THESIS FOR THE DEGREE OF DOCTOR OF PHILOSOPHY

Co-precipitation of Actinide Hydrous Oxides and Leaching of Unirradiated MOX Fuel in the Presence of Iron and its Corrosion Products

Mustapha G. Saleh

Department of Chemistry and Chemical Engineering

Chalmers University of Technology

Gothenburg, Sweden 2026

Co-precipitation of Actinide Hydrous Oxides and Leaching of Unirradiated MOX Fuel in the Presence of Iron and its Corrosion Products

Mustapha G. Saleh

ISBN:978-91-8103-412-7

Doktorsavhandlingar vid Chalmers Tekniska Högskola
Ny serie nr: 5869
ISSN:0346-718x
DOI: https://doi.org/10.63959/chalmers.dt/5869

Department of Chemistry and Chemical Engineering
Chalmers University of Technology
SE- 412 96 Gothenburg,
Sweden
Telephone: +46 (0) 31-772 1000

Cover:
Deep geological repository (engineered) safety barrier system and autoclave used for the leaching experiment.

Printed by:
Chalmers digitaltryck
Gothenburg, Sweden 2026

Co-precipitation of Actinide Hydrous Oxides and Leaching of Unirradiated MOX Fuel in the Presence of Iron and its Corrosion Products

Mustapha G. Saleh

Department of Chemistry and Chemical Engineering
Chalmers University of Technology

Abstract

With growing global energy demand and the need to ensure energy security, meet climate goals, and support sustainable development, nuclear energy has experienced a renewed global interest. However, the safe disposal and management of high-level radioactive waste, particularly spent nuclear fuel (SNF), remains a significant scientific, societal and political challenge on a global scale. One Proposed solution is the long-term isolation of the SNF in deep geological repositories (DGRs), where SNF is enclosed in copper canisters with an iron insert, surrounded by bentonite clay, and placed ~500 meters underground in granitic bedrock. While deep geological repositories (DGR) are designed to rapidly evolve towards anoxic, reducing conditions after closure, a potential breach of the canister containment followed by groundwater intrusion to the SNF can generate localized oxidizing conditions through the formation of radiolytic oxidants produced through water radiolysis. Such conditions can induce oxidative dissolution of UO_2 matrix, potentially resulting in the mobilization and release of highly radiotoxic radionuclides into the biosphere. Metallic iron, a key component of the engineered barrier system, can simultaneously undergo anoxic corrosion upon contact with groundwater, producing Fe(II) and H_2. These species could inhibit the oxidative dissolution of the spent fuel matrix. In addition, metallic iron and Fe(II) may also play a crucial role in reducing U(VI) to U(IV) in groundwater systems, thereby limiting its solubility and mobility. Furthermore, the co-precipitation UO_2(s) with minor components of the SNF may serve as a retention mechanism for radionuclides, further enhancing repository safety. Therefore, a detailed understanding of fuel matrix dissolution, radionuclide migration, and interactions with engineered barrier materials is essential for assessing repository performance over extended timescales. This thesis investigates key chemical processes influencing the behaviour of SNF under DGR conditions. The findings indicate that anoxic corrosion of metallic iron significantly suppresses radiolytically induced oxidative dissolution of the fuel, leading to lower actinide releases. The coprecipitation studies infer that the concentrations of other actinides, lanthanides, and fission products released by the fuel matrix during oxidative dissolution will not be determined by their individual solubilities when they coprecipitate with UO_2(s) at the iron surface of the canister insert but will be orders of magnitude lower. Additionally, metallic iron efficiently reduces U(VI) to U(IV), promoting its sorption and precipitation on iron corrosion products. Overall, this thesis provides new insights and a better understanding of uranium redox behaviour in groundwater systems, spent fuel redox stability, and actinide oxides co-precipitation processes under repository-relevant conditions.

Keywords: UO_2, Solubility, Co-precipitation, Dissolution, MOX fuel, Fe(II), H_2, Actinides, Geological disposal

LIST OF PUBLICATIONS

This thesis is based on the work contained in the following papers. Referred to by Roman numerals in the text:

I. N.L. Hansson, **M. Saleh,** P. L. Tam, S. Holgersson, K. Spahiu, C. Ekberg, Influence of groundwater composition on the reductive precipitation of U(VI) on corroding iron foil surfaces. Journal of Nuclear Materials, 577 (2023) 154324, Journal of Nuclear Materials, 577 (2023) 154324, https://doi.org/10.1016/j.jnucmat.2023.154324.

Contribution: Investigation, Formal analysis, Writing- Review & Editing.

II. **M. Saleh**, M. Hedberg, P. L. Tam, K. Spahiu, I. Persson, C. Ekberg, Coprecipitation of Ce(III) oxide with UO_2. Journal of Synchrotron Radiation (2024) 31, https://doi.org/10.1107/S1600577524008336.

Contribution: Conceptualization, Formal analysis, Investigation, Methodology, Writing - Original Draft, Writing- Review & Editing.

III. **M. Saleh**, N.L. Hansson, M. Hedberg, P. L. Tam, K. Spahiu, C. Ekberg, Dissolution of unirradiated MOX fuel in the presence of metallic iron, Journal of Nuclear Materials 618 (2026) 156202, https://doi.org/10.1016/j.jnucmat.2025.156202.

Contribution: Conceptualization, Formal analysis, Investigation, Methodology, Writing - Original Draft, Writing- Review & Editing.

IV. **M. Saleh**, M. Hedberg, E. Lawrence Bright, K.O. Kvashnina, M. Ghaly, C. Andrikopoulos, I. Petropoulou Kynigopoulou, K. Spahiu, C. Ekberg, Coprecipitation of Pu and Np amorphous oxides with UO_2(am, hyd). Submitted to the Journal of Nuclear Materials.

Contribution: Conceptualization, Formal analysis, Investigation, Methodology, Data curation, Validation, Visualization, Writing - Original Draft, Writing-Review & Editing.

V. **M. Saleh**, E. Darwish, M. Hedberg, P. L. Tam, K. Spahiu, C. Ekberg, Dissolution of unirradiated MOX fuel in the presence of magnetite and chukanovite. Submitted to the Journal of Nuclear Materials and Energy.

Contribution: Conceptualization, Formal analysis, Investigation, Methodology, Data curation, Validation, Visualization, Writing - Original Draft, Writing- Review & Editing

ABBREVIATIONS AND DEFINITIONS

The following abbreviations and definitions were used during this thesis:

am	Amorphous
DGR	Deep Geological Repositories
EDX	Energy dispersive X-ray
EURATOM	European Atomic Energy Community.
FT-IR	Fourier Transform Infrared Spectroscopy.
GW	Giga Watt
HALEU	High Assay Low Enriched Uranium
HLW	High -Level Waste
ICP-MS	Inductively Coupled Plasma Mass Spectroscopy
ICP-OES	Inductively Coupled Plasma Optical Emission Spectroscopy
IEA	International Energy Agency
ILW	Intermediate Level Waste
IAEA	International Atomic Energy Agency
LET	Linear Energy Transfer
LLW	Low-level waste
LWRs	Light Water Reactors
MeV	Mega electron volt
MOX	Mixed Oxide fuel
MQ	Milli-Q (high purity water)
MWCO	Molecular Weight Cut-off
NEA	Nuclear Energy Agency
NEA-TDB	Nuclear Energy Agency Thermodynamic Database
ppb	Part per billion
ppm	Part per million
PWRs	Pressurized Water Reactors
SEM	Scanning Electron Microscopy
SKB	Svensk Kärnbränslehantering
SNF	Spent Nuclear Fuel
UO_2	Uranium dioxide
UV-Vis	Ultraviolet Visible
VLLW	Very Low-Level Waste
XANES	X-ray Absorption Near- Edge Structure
XAS	X-ray Absorption Spectroscopy
XPS	X-ray Photoelectron Spectroscopy
P-XRD	Powder X-ray Diffraction

Table of Contents

1.0. Introduction

Nuclear power remains an important source of reliable low-carbon electricity, and it plays a significant role in global efforts to reduce greenhouse gas emissions. As the demand for clean and secure energy continues to rise, nuclear power is increasingly viewed as a crucial component of future energy systems, alongside renewable sources such as solar and wind [1-3]. According to the International Atomic Energy Agency (IAEA), as of November 2025, ~ 416 nuclear power reactors were in operation worldwide, with a combined net electrical capacity of about 376 GW(e) [3]. In addition, more than sixty reactors are currently under construction, representing an additional capacity of ~ 66 GW(e) [4]. Long-term projections indicate that global nuclear generating capacity could increase significantly by 2050, reflecting the growing role of nuclear power in supporting climate mitigation and energy security [5].
Despite its advantages, nuclear energy also presents several challenges, such as long construction timelines, high capital investment costs, public acceptance issues, and safety concerns arising from past nuclear accidents. Among these challenges, the long-term management of highly radioactive waste (HLW) such as spent nuclear fuel (SNF) remains one of the most critical issues associated with nuclear energy [6-9]. SNF, which is generated during reactor operation, contains long-lived radionuclides and accounts for ~ 95% of the total radiotoxicity of nuclear waste [10, 11]. These radionuclides must be safely isolated from the biosphere for extended timescales to prevent potential environmental and health risks. Deep geological disposal has been widely recognized as a reliable and scientifically supported strategy for the long-term management of SNF.

In Sweden, nuclear power accounts for nearly 30% of the country's electricity production, and ~ 8,000 tonnes of SNF have been generated from its nuclear operations. Currently, this spent fuel is stored in interim storage facilities while awaiting final disposal [12]. The Swedish strategy for long-term SNF management is based on the KBS-3 concept, which involves encapsulating spent fuel assemblies in corrosion-resistant copper canisters with cast-iron inserts. These canisters are surrounded by a bentonite clay buffer and emplaced at a depth of ~ 500 m in crystalline bedrock [13, 14]. The multi-barrier system is designed to prevent or limit radionuclide release through the combined natural and engineered safety barriers protection offered by the fuel matrix, the canister, the bentonite buffer, and the surrounding geological bedrock formation [13]. While the KBS-3 repository concept is designed to provide long-term containment of SNF, safety assessment must consider potential failure scenarios that may occur over geological timescales. One of the most important scenarios evaluated in repository safety analysis is the intrusion of groundwater into a breached canister [15]. If the copper canisters fail after prolonged geological evolution, groundwater may eventually come into contact with the SNF matrix. Under such conditions, the interaction between groundwater and the fuel surface becomes a critical factor controlling radionuclide release.

Under the reducing conditions expected in deep geological repositories, uranium (U) is predominantly present in the tetravalent state as UO_2, which has very low solubility [16]. However, radiolysis of water by radiation emitted from spent fuel can generate oxidizing species, such as hydrogen peroxide (H_2O_2) and molecular oxygen (O_2) [17]. These oxidants can promote oxidative dissolution of UO_2 by oxidizing the relatively insoluble U(IV) into the more soluble U(VI) species, potentially enhancing radionuclide release from the fuel matrix.

At the same time, the repository environment also contains several processes that may counteract oxidative dissolution. Anoxic corrosion of iron components within the copper canisters can produce Fe(II), hydrogen (H_2), and secondary iron corrosion products, such as magnetite, green rust, and chukanovite, etc. These species can act as reducing agents, scavenging or mitigating the effects of radiolytic oxidants and helping to maintain reducing conditions in the near-field environment surrounding the fuel [18]. Despite this potentially beneficial process, the extent to which these processes can mitigate or suppress the oxidative dissolution of the fuel matrix remains incompletely understood. Another important factor influencing radionuclide mobility during fuel alteration is the potential formation of secondary actinide phases. During fuel degradation, actinides such as U, plutonium (Pu), and neptunium (Np) may co-precipitate or form solid solutions with hydrous oxide phases. These processes can significantly influence the long-term solubility and transport behaviour of actinides in groundwater systems. However, the mechanisms controlling actinide co-precipitation and the extent to which these processes may limit actinide mobility in repository environments remain insufficiently explored. The overall aim of this thesis is therefore to improve the understanding of key chemical processes controlling the behaviour of SNF under repository-relevant conditions.

This work focuses on three main aspects relevant to the long-term behaviour of SNF under disposal conditions. First, the reduction behaviour of U(VI) in groundwater systems in the presence of metallic iron was investigated, with particular focus on the influence of calcium–uranyl–carbonato complexes on U reduction and precipitation processes. Secondly, the dissolution behaviour of unirradiated mixed oxide (MOX) fuel was studied under controlled experimental conditions. These experiments investigated the influence of metallic iron and iron corrosion products, specifically magnetite and chukanovite, on the suppression of oxidative fuel dissolution driven by radiolytically generated oxidants such as H_2O_2 and O_2. Finally, the co-precipitation behaviour of actinide hydrous oxides was examined. Initial studies focused on the co-precipitation of Ce(III) with amorphous UO_2, where Ce was used as a simulant for Pu. This was followed by experiments investigating the co-precipitation of Pu and Np amorphous oxides with UO_2 (am, hyd). These studies were designed to improve the understanding of actinide co-precipitation processes and their potential influence on actinide solubility during spent fuel alteration.

2.0 Background

This chapter presents the background to the thesis work, with an overview of actinide chemistry (U, Pu, and Np), the nuclear fuel cycle, and the composition and behaviour of SNF under disposal-relevant conditions. It outlines a deep geological repository as a management option for SNF and the mechanisms governing radiation-induced fuel dissolution with emphasis on the role of repository-relevant reductants. Actinide coprecipitation under reducing conditions is also discussed as a key retention mechanism influencing long-term spent fuel stability.

2.1. Chemistry of Uranium, Plutonium, and Neptunium

Uranium (U), plutonium (Pu), and neptunium (Np) are key actinides in the nuclear fuel cycle and are of particular importance in environmental radiochemistry and long-term safety assessments of deep geological repositories. Their chemistry is characterized by multiple oxidation states, strong complexation with inorganic and organic ligands, and redox-driven transformations that govern their solubility, mobility, and retention in the natural environment [19-22].

Uranium, one of the few naturally occurring actinides, was discovered in 1789 by Klaproth and later identified as radioactive by Becquerel and Curie. It became central to nuclear energy following the discovery of the fissile isotope U-235 and nuclear fission [19]. Natural U consists primarily of the α-emitting isotopes U-238 ($t_{1/2} = 4.47 \times 10^9$ y), U-235 ($t_{1/2} = 7.04 \times 10^8$ y), U-234 ($t_{1/2} = 2.46 \times 10^5$ y) [19, 23]. U is relatively abundant in the Earth's crust (2-3 ppm) [24]. It occurs in a wide range of minerals such as uraninite, pitchblende, etc. [24-26]. In aqueous systems, U commonly exists in the +IV, +V, and +VI oxidation states [19, 21]. The relative stability of these oxidation states is strongly influenced by redox conditions, pH, and the presence of complexing ligands [21]. U(IV) compounds are generally insoluble under mildly acidic to alkaline conditions, whereas U(VI) compounds, primarily the uranyl ion UO_2^{2+}, are highly soluble and mobile [19, 25]. U(VI) dominates under oxic and carbonate-rich conditions, where it forms stable aqueous complexes with carbonate, hydroxide, and oxalate ligands. Under reducing conditions, U(IV) precipitates as UO_2(s) and exhibits very low solubility. U(V) is relatively rare, metastable, and typically undergoes disproportionation to U(IV) and U(VI) [19].

Plutonium, a transuranic element also belonging to the actinide series, was first synthesized by Seaborg and colleagues in 1940 [20]. It became scientifically and technologically significant following its discovery, initially due to its role in nuclear weapons development during World War II. However, in contemporary nuclear science, its relevance is primarily associated with civilian applications, including mixed oxide (MOX) fuel fabrication, nuclear fuel reprocessing, and radioactive waste management [20, 22]. The chemistry of Pu is complex and diverse, as it can react with almost every element in the periodic table [20]. Pu exhibits several isotopes, all of which are radioactive, with Pu-238 ($t_{1/2} = 87.7$ years), Pu-239 ($t_{1/2} = 24{,}100$ years), and Pu-240 ($t_{1/2} = 6560$ years) being the most significant in spent nuclear fuel [19]. Unlike U, Pu is extremely rare in nature, occurring only in trace amounts due to neutron capture by U-238, but it is produced in significant quantities during the irradiation of nuclear fuel [19, 20].
In aqueous solution, Pu behaviour is governed by its redox chemistry and its tendency to form hydrolyzed species and colloid formation, as well as complexation with other ligands. Pu displays multiple oxidation states in aqueous solution, predominantly +III, +IV, +V, and +VI, of which all

can co-exist in solution at a given time [27]. Pu redox chemistry is highly sensitive to pH and redox potential [20, 22, 28]. In acidic solutions, the standard redox potentials of the various Pu couples are very similar, with values close to 1.0 V. This close potential implies that Pu is highly sensitive to slight variations in the system redox condition, which can lead to changes in the oxidation state [27].Under reducing conditions, Pu(IV) is the most stable dominant oxidation state and precipitates as $Pu(OH)_4(s)$ or $PuO_2.XH_2O$, which is sparingly soluble due to its low solubility and strong sorption property. Pu(VI) is stable under oxidizing conditions, while Pu(III) is stable only under strongly reducing conditions. [22, 27, 29, 30]. Pu(V) and Pu(VI), present as PuO_2^+ and PuO_2^{2+}, are more soluble under oxic conditions [28, 30]. Understanding Pu redox behaviour, hydrolysis, complexation, adsorption to minerals and colloids facilitated transport is therefore crucial for assessing the long-term safety of deep geological repositories.

Neptunium, the first transuranium element to be discovered, was identified in 1940 by McMillan and Abelson during neutron irradiation of U [19, 32]. It is produced in nuclear reactors primarily through neutron capture by U-238, followed by β-decay, and is therefore present in spent nuclear fuel and reprocessing wastes [19, 32]. Several Np isotopes occur as by-products in nuclear reactors. Among its isotopes, Np-237 ($t_{1/2}$ = 2.144 x 10^6 y) is the most abundant and environmentally relevant due to its long half-life and significant contribution to long-term radiotoxicity in nuclear waste repositories [19, 32]. Distinct from the rest of its actinide neighbours, Np displays truly unique chemistry due to its speciation and chemical behaviour [32]. In aqueous environments, Np can exist in various oxidation states, such as +III, +IV, +V, +VI, and +VII [19, 33]. However, Np(IV) and Np(V) are the most environmentally relevant [20, 34]. Np(V), neptunyl(V) ion, NpO_2^+, is the most stable species over a wide range of environmental conditions and is generally more soluble and mobile than Np(IV) [25, 32]. Under reducing conditions, Np(IV) forms insoluble oxides and hydroxides ($NpO_2(s)$), while Np(VI), as NpO_2^{2+} may exist under strong oxidizing conditions but is less stable than the pentavalent state [31, 32]. Complexation with carbonate, sulfate, phosphate, and humic substances enhances Np solubility [25, 31].

Under reducing repository conditions, U(IV), Pu(IV), and Np(IV) form low-solubility oxides. In addition, U, Pu, and Np can interact strongly with mineral surfaces, such as iron (oxyhydr) oxide phases, clay minerals, and silicate phases, as well as with natural organic matter. Processes such as adsorption and precipitation with anions can significantly retard their migration [30, 31, 34, 35]. However, radiolytically generated oxidants may locally shift redox conditions toward a more oxidizing environment, forming soluble actinyl species and potentially enhancing actinide mobility [19, 30].

2.2. Nuclear fuel cycle

The nuclear fuel cycle comprises a series of processes involved in the production, utilization, and management of nuclear fuel, extending from U extraction to the final disposal of radioactive waste. It is commonly divided into the front end, in-reactor phase, and the back end, all of which play a critical role in the overall safety, sustainability, and environmental impact of nuclear energy systems. The front end of the fuel cycle involves the steps of mining and milling, conversion, enrichment, and fuel fabrication. After the irradiation of the fuel in a nuclear reactor to generate electricity, the resulting used or spent nuclear fuel undergoes a series of further steps, including interim storage, waste transportation, and/or reprocessing or recycling operations, before its final disposal as spent nuclear fuel or high-level radioactive waste [9, 36]. These steps constitute the

“back end” of the nuclear fuel cycle. The selection of an open or closed fuel cycle strategy significantly influences resource utilization, waste generation, management, and long-term safety considerations [6, 37]. U in the form of UO_2 is widely used as nuclear fuel. The suitability of UO_2 as a nuclear fuel arises from its high melting point, stability under irradiation, and resistance to phase transformation even at elevated temperature [38]. After mining and milling of U ore, it is then processed (purification) to produce U oxide concentrates, which are subsequently converted to uranium hexafluoride (UF_6) for enrichment (3-5%). Enrichment increases the fissile U-235 content to levels suitable for reactor operation, after which the material is fabricated (converting UF_6 gas into UO_2 powder, pressing of powder, and sintering of fuel pellets) into fuel assemblies, typically UO_2 ceramic pellets for light-water reactors [26]. Recent developments at the front-end focus on advanced fuels and enrichment strategies, such as high-assay low-enriched uranium (HALEU) fuel driven by the deployment of advanced reactors and small modular reactors [6].

The nuclear reactor is used to initiate and control a sustained nuclear chain reaction. Nuclear reactors are the core components of nuclear power plants, which are responsible for converting nuclear energy into thermal energy, which is then used to generate electricity. During the in-reactor phase, nuclear fuel undergoes fission and neutron capture, leading to the formation of fission products and transuranic elements. These processes result in significant changes in the chemical composition, microstructure, and radiological properties of the fuel. The accumulation of minor actinides and irradiation-induced defects in the UO_2 matrix directly influences the characteristics of spent nuclear fuel and its subsequent management [39]. The back end of the nuclear fuel cycle addresses the management of SNF following reactor discharge. After an initial period of cooling in spent fuel pools, fuel may be transferred to dry storage or processed further depending on the adopted fuel cycle strategy [36]. In open fuel cycles, spent nuclear fuel is considered waste, and it is conditioned for direct disposal in deep geological repositories. In closed fuel cycles, reprocessing technologies are applied to recover U and Pu for reuse, while separated high-level waste is conditioned for disposal. Each approach presents distinct economic, technical, and safety challenges, particularly with respect to waste form stability and long-term radionuclide release [9, 37, 40].

The selection of a nuclear fuel cycle is driven mainly by economic considerations, environmental impact, proliferation risk, and cost, which are closely linked to national energy policies. These policies are, in turn, shaped by the availability and nature of each country’s energy resources [40]. Advanced reactor concepts (advanced reactor designs) and innovative fuel cycle strategies have renewed interest in closing the nuclear fuel cycle to improve resource efficiency and reduce waste inventories [6, 41]. However, advanced reactors and fuels (higher burnup levels) may introduce new complexities for backend waste management, including changes to waste compositions, radionuclide inventory, and waste volume, which can lead to increased demands on disposal systems [6, 42]. As a result, considerations and compatibility between advanced fuel cycles and existing repository concepts must be carefully evaluated [6]. Safety and regulatory directives are fundamental to all stages of the nuclear fuel cycle. International guidance provided by organizations such as the IAEA, Euratom, and OECD/NEA emphasizes the need for robust and stringent safety assessments, particularly for long-term waste management [36]. Geological disposal concepts require a comprehensive understanding of fuel matrix stability, geochemical interactions, and radionuclide release mechanisms over geological timescales [37, 43].

The future of the nuclear fuel cycle will be shaped by the demand for low-carbon energy, energy security, technological innovation, and societal acceptance [6, 44]. While advanced reactors and

recycling options continue to develop and evolve, direct disposal of SNF remains the reference strategy in several countries. Consequently, continued research into spent fuel chemistry and behavior under repository-relevant conditions remains central to ensuring the long-term safety of nuclear energy systems.

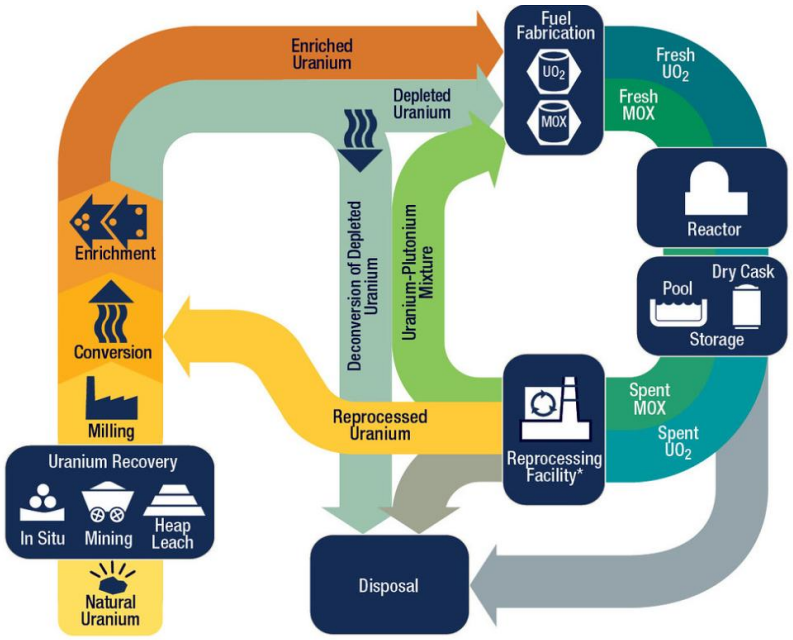

Figure 1: Nuclear fuel cycle. Source: [45] (Public domain)

2.3. Spent nuclear fuel, its composition, and the chemical state of fission products

SNF is generated following prolonged irradiation of nuclear fuel in a nuclear reactor and represents the principal high-level radioactive waste arising from nuclear energy production. SNF is classified as a complex, heterogeneous material dominated by a nearly stoichiometric UO_2 matrix. This matrix is a redox-sensitive, semiconducting, and polycrystalline ceramic material that hosts most radionuclides generated during reactor operations [46, 47]. The worldwide operation of commercial nuclear power reactors has resulted in an accumulated inventory of approximately 430,000 metric tonnes of heavy metal (mtHM), with an annual increase of roughly 10,000 mtHM [48, 49]. The microstructure and chemical characteristics of spent fuel have been extensively investigated in earlier studies [50, 51]. More recently, advances in analytical and spectroscopic techniques have enabled increasingly detailed characterization of fission product distributions, revealing important variations in chemical speciation and phase distribution in high burn-up fuels [52].

At discharge from the reactor, the majority of the fuel mass remains as UO_2 (typically ~ 95%), while the remaining fraction consists of fission products, transuranium elements, and activation products formed during reactor operation. These include radionuclides such as Sr-90, I-129, I-131, and Cs-137 among the fission products, Np-237, Pu-239, Am-241 and Cm-242 among the transuranium elements, and activation products such as C-14, Co-60, 63-Ni [51, 53]. Although present in relatively small quantities, these radionuclides dominate the radiotoxicity and heat generation of the fuel over time [54]. The radionuclide inventory evolves continuously due to

radioactive decay, heat generation, and radiation fields, particularly during the early post-discharge period [46, 55, 56].

The final composition of SNF depends on reactor-specific parameters such as fuel type, chemical composition, U enrichment, neutron spectrum, and achieved fuel burn-up [46, 55, 57]. At the microscale, radionuclides are heterogeneously distributed within the UO_2 matrix and occur in multiple chemical and physical forms [58]. Actinides such as Np and Pu, together with many fission products, including Sr and lanthanide oxides, are incorporated into the UO_2 matrix as solid solutions [46, 58]. Fission products such as Cs and I segregate UO_2 grain boundaries, the fuel-cladding gap, and spaces between fuel pellets. Volatile fission products such as Kr, Xe, and I are predominantly retained within intragranular gas bubbles within the fuel grains, influencing thermal and mechanical properties. Other fission products (such as Ba, Cs, Zr, and Rb) form oxide precipitates along UO_2 grain boundaries, where also metallic particles composed of Mo, Tc, and noble metal fission products such as Pd, Pt, Ru, and Rh (referred to as ε-particles) precipitate [47, 58, 59].

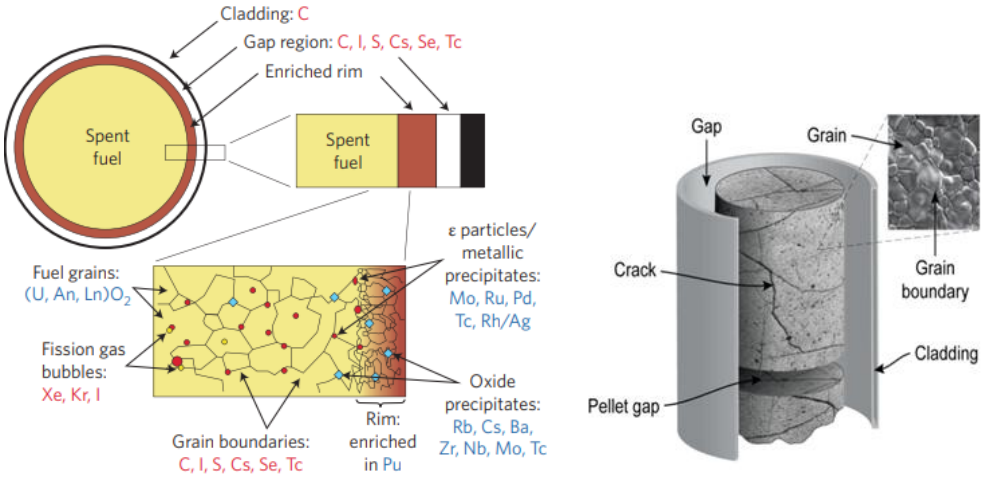

Figure 2. Schematic illustration of the microstructure and the distribution of elements in SNF after irradiation in a reactor. Adapted from Buck et al. (2004) and Bruno et al. (2006) [46, 60].

2.4. Management and disposal of radioactive nuclear waste

Radioactive waste is generated as a consequence of nuclear power production and the use of radioactive materials in research, medical, and industrial applications [48]. Such waste must be carefully managed to protect humans and the environment from the harmful effects of ionizing radiation, including genetic damage and increased risk of cancer [48, 61, 62]. The hazard posed by radioactive waste depends on factors such as radiotoxicity, decay heat, the type and energy of radiation emitted, and the duration over which the waste remains hazardous [63]. Radioactive waste is generally classified into several categories: high-level waste (HLW), intermediate-level waste (ILW), low-level waste (LLW), and very low-level waste (VLLW), as well as according to its half-life (long or short-lived) [48, 64]. Disposal strategies are determined based on this classification, ranging from near-surface facilities for VLLW to deep geological repositories for HLW [48].

The choice of disposal depends on the radioactivity of the waste as well as national regulations and established practices [48]. Proper management is essential to ensure safety during handling,

storage, and eventual disposal [48]. Waste poses long-term hazards to human health and the environment and requires containment or encapsulation in appropriate packaging and disposal within engineered facilities designed with multiple protective barriers [48]. A central challenge in the continued use of nuclear energy is the effective management of highly radioactive waste [65].

Among the different waste forms, SNF represents the most radiologically significant material produced during nuclear power generation. Although it constitutes a relatively small fraction of the total waste volume, it accounts for the majority of the radioactivity and long-term radiotoxicity associated with nuclear energy production [46, 66]. After discharge from the reactor, spent fuel initially requires active management such as cooling and radiation shielding to remove decay heat [48, 65]. Long-term disposal strategies must subsequently ensure the isolation of radionuclides from the biosphere over extended timescales. Because of its long-lived radionuclide inventory, SNF is universally categorized as high-level, long-lived waste, requiring isolation from the biosphere for timescales of approximately 10^4-10^5 years until its radiological hazard declines to levels similar to natural uranium ores [48, 66, 67].

Several strategies have been proposed for managing this waste, including recycling of usable materials or direct disposal of spent fuel [9]. At present, the international scientific and regulatory consensus supports deep geological disposal in stable geological formations as the most viable long-term solution for the safe management and isolation of SNF [36, 46].

2.5. Deep geological repositories and the multi-barrier safety concept

Deep geological disposal is internationally recognized as a safe and effective approach for the long-term management of SNF and other HLW [14,65]. Several countries, such as Finland, Sweden, Switzerland, Canada, etc., have adopted or are in advanced stages of implementing geological disposal programmes based on this concept [65, 68]. DGRs consists of an interconnected system of carefully engineered underground tunnels and deposition areas constructed within stable geological formations at depths of several hundred metres [68]. At such depth, geological processes evolve slowly, and environmental conditions are favourable for long-term isolation and containment of radioactive waste.

The long-term safety of DGRs relies on a multi-barrier system, in which engineered and natural barriers work together to contain radionuclide and limit their migration to the biosphere [14]. Safety is achieved through the complementary performance of the waste form, engineered barriers, and surrounding host rock. These barriers are designed to fulfil two primary safety functions: ensuring long-term containment of the spent fuel and, in the unlikely event of containment failure, retarding radionuclide migration [13].

The SNF itself constitutes the first barrier due to the low solubility and slow dissolution kinetics of the UO_2 matrix under reducing conditions, which are expected to prevail after repository closure [69]. Additional engineered barriers typically include corrosion-resistant metallic canisters, buffer or backfill materials such as bentonite clay, which provide mechanical support and restrict groundwater flow around the waste packages [69]. The surrounding host rock provides additional natural barriers by ensuring long-term mechanical stability and favourable geochemical conditions for radionuclide retention, including low permeability [65, 68, 69].

Different national waste management programmes have adopted repository concepts adapted to their geological settings. Crystalline bedrock formations are considered in Nordic countries, clay

formations in parts of Western Europe, and salt formations in other regions [68, 70]. In Sweden and Finland, the disposal strategy is based on the KBS-3 concept. In 2022, the Swedish government approved Svensk Kärnbränslehantering AB (SKB) to proceed with the construction of a DGR, following decades of research, site investigations, and safety assessments. This decision positioned Sweden as the second country, after Finland, to advance from repository planning to construction and implementation [71].

The planned Swedish repository system would comprise an encapsulation facility located near the interim storage facility (CLAB) in Oskarshamn, and a repository located at approximately 500 m depth in crystalline bedrock at Forsmark in the Östhammar municipality [13]. Within the KBS-3 design, fuel assemblies consisting of UO_2 pellets enclosed in zirconium-based cladding are encapsulated in copper canisters ~ 5 m long and weighing up to 25 tonnes. Each canister contains a load-bearing nodular cast iron insert that provides mechanical strength, while the copper shell (~ 5 cm thick) serves as the primary corrosion barrier. Each canister is surrounded by a compacted bentonite clay buffer. Upon hydration, bentonite swells to form a low-permeability barrier that resists groundwater flow around the canisters and into the bedrock, limits advective radionuclide transport, and provides mechanical support to the canisters [13]. After emplacing the canisters, deposition tunnels are backfilled with bentonite clay.

The final safety barrier is the surrounding host rock, whose primary function is to ensure long-term isolation of the repository from the biosphere. If radionuclides are released from a breached canister and migrate beyond the bentonite buffer, their transport within the host rock may be significantly retarded through processes such as sorption onto fracture surfaces, interaction with fracture minerals, and diffusion into the rock matrix micro porosity [13]. The geological bedrock formation, therefore, provides a geochemically stable environment that protects the repository from surface events or processes over geological timescales [13].

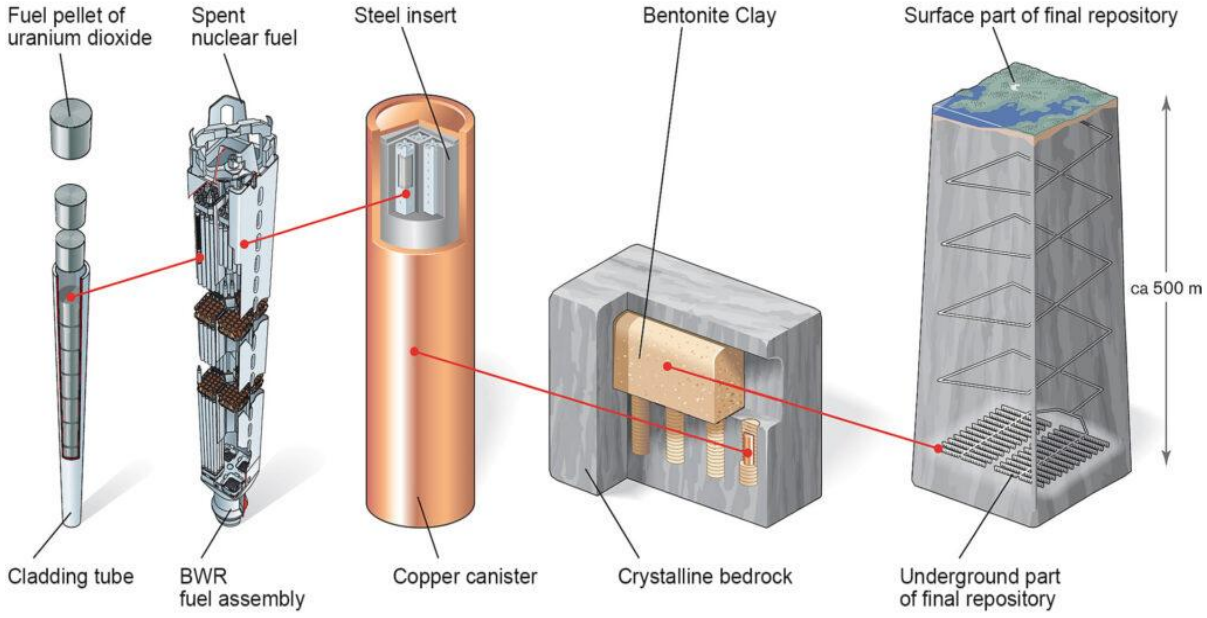

Figure 3. The KBS-3 design incorporates safety barrier features such as fuel pellet, copper canister, bentonite clay, and crystalline bedrock. Illustration: Jan Rojmar, Svensk Kärnbränslehantering AB. Reproduced with permission from SKB.

2.6. Radiation-induced SNF dissolution under disposal conditions

While the engineered barrier system (EBS) of DGRs is designed to provide robust containment and ensure long-term isolation of SNF, the potential intrusion of groundwater following canister failure is explicitly considered in repository safety assessments [13, 72]. Such failure scenarios are generally associated with long-term degradation processes, including corrosion of metallic components, erosion of the bentonite buffer, or mechanically induced damage caused by shear movements in the host rock [13]. Safety analyses indicate that the likelihood of canister failure during the first thousand years after repository closure is extremely low; nevertheless, these scenarios are assessed to ensure robust long-term safety [13, 73].

After repository closure, residual oxygen in the repository will be consumed by reducing minerals and microbial activity (bacteria) [13]. As a result, strongly reducing and anoxic conditions are expected to prevail within the disposal environment. Under such conditions, the UO_2 matrix remains stable and exhibits very low solubility under deep geological conditions [74]. Consequently, groundwater represents the primary potential transport pathway for radionuclide mobility from the repository to the biosphere, a process that becomes relevant only in the event of canister breach. In such cases, the release of radionuclides is governed by the dissolution behaviour of the UO_2 fuel matrix itself, a mechanism that has been recognized as central to repository safety assessments for several decades [75-77].The dissolution rate of UO_2 under disposal-relevant conditions depends on several factors, including fuel composition, burnup, groundwater chemistry, and surface redox conditions [75, 76, 78-82]. When groundwater comes into direct contact with spent fuel following canister failure, ionizing radiation emitted by the fuel matrix induces water radiolysis. This process can alter the groundwater redox environment from reducing to more oxidizing conditions [75, 77]. This radiolytic process generates a range of highly reactive species and molecular products such as oxidants ($OH^{\bullet}$, H_2O_2, $HO_2^{\bullet}$, O_2) and reductants (e^-_{aq}, $H^{\bullet}$, H_2), which are formed in approximately equal proportions [75]. Radiolysis-driven corrosion at the UO_2-water interface has been shown to dominate fuel dissolution under anoxic conditions, with oxidant production occurring locally at the fuel surface [83]. Among the radiolytic oxidants, hydrogen peroxide (H_2O_2) has been identified as the dominant species responsible for oxidative dissolution of UO_2 [84, 85].

The interaction of H_2O_2 with the UO_2 surface leads to oxidation of U(IV) to the significantly more soluble U(VI), thereby enhancing matrix dissolution according to the reaction:

$$UO_2(s) + H_2O_2 \rightarrow UO_2^{2+}(aq) + 2OH^- \quad (1)$$

The extent of oxidative dissolution of the UO_2 fuel matrix is strongly controlled by the groundwater composition [86]. In particular, bicarbonate and carbonate would enhance U solubility, by stabilizing it through strong aqueous complexation, even at low oxidant concentrations [87]. More generally, radiolytic oxidation of U(IV) to the more soluble U(VI), together with complexation by dissolved ligands, promotes dissolution of the fuel matrix [86, 87]. The production of radiolytic oxidants driving these processes is governed by the radiation dose rate, which is influenced by factors such as fuel age, burnup, and the proximity to the fuel surface [86, 88]. These dependencies highlight the importance of site-specific groundwater chemistry and fuel characteristics when assessing the long-term stability of spent nuclear fuel under disposal conditions. Given that groundwater represents the only viable pathway for radionuclide transport

from the repository to the biosphere, it is essential to further investigate scenarios involving canister breach and water intrusion. Understanding the dissolution and migration behaviour of radionuclides under repository-relevant conditions is therefore critical, highlighting the significance and relevance of the research work presented in this thesis.

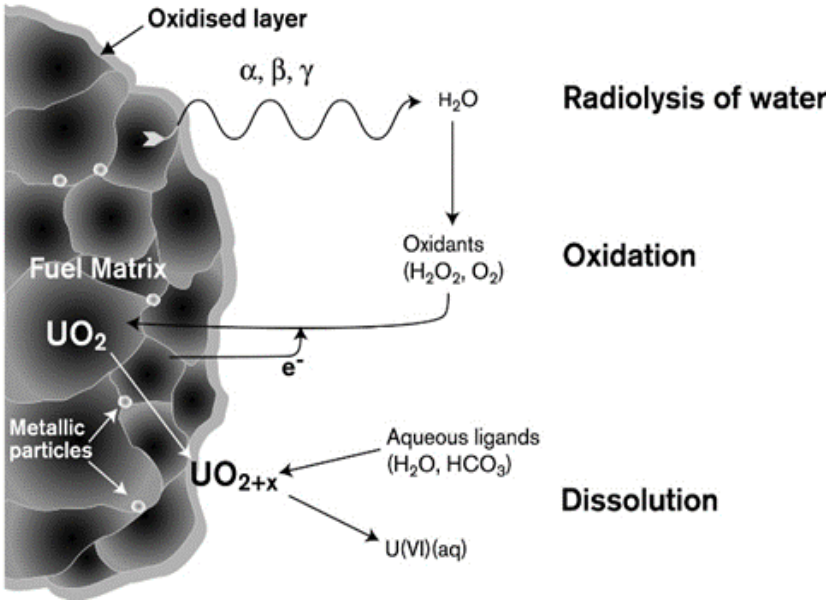

Figure 4. Radiation-induced oxidative dissolution of spent nuclear fuel. Illustration: Svensk Kärnbränslehantering AB (SKB). Reproduced with permission from SKB.

2.7. Role of potential repository reductants in controlling SNF dissolution

In DGRs for SNF, the long-term redox conditions in the near-field environment are strongly influenced by the presence of reducing agents generated within the repository system. In the Swedish KBS-3 repository concept, each spent fuel canister contains a substantial amount of iron (14 tons) in the form of a cast iron insert enclosed by a copper shell, making iron a key component influencing repository geochemistry [72, 89]. In the event of canister breach and subsequent groundwater intrusion, anaerobic corrosion of iron is expected to occur under the prevailing anoxic conditions [90].

Aqueous corrosion of iron under reducing conditions can lead to the formation of various secondary iron corrosion products, including magnetite, green rust, siderite, and chukanovite, depending on groundwater composition and redox conditions [91–95]. Among these iron phases, magnetite has been identified as the dominant corrosion product formed during anoxic iron corrosion under repository-relevant conditions in the long term [18, 94–96]. The corrosion process would result in the release of dissolved Fe(II) and the generation of significant amounts of molecular hydrogen (H_2), both of which act as effective reductants in the near-field environment [96-99]. Representative reactions describing anoxic iron corrosion include:

$$Fe(s) + 2\ H_2O(l) \rightleftharpoons Fe(OH)_2(aq) + H_2(g) \qquad (2)$$

$$3\ Fe(s) + 4\ H_2O(l) \rightleftharpoons Fe_3O_4(s) + 4\ H_2(g) \qquad (3)$$

The formation of dissolved Fe(II) plays a crucial role in consuming radiolytically generated oxidants, particularly hydrogen peroxide (H_2O_2), through redox reactions that convert Fe(II) to Fe(III). These reactions include:

$$Fe^{2+} + H_2O_2 \rightarrow Fe^{3+} + OH\cdot + OH^- \quad (4)$$

$$Fe^{2+} + OH\cdot \rightarrow Fe^{3+} + OH^- \quad (5)$$

Through these reactions, Fe(II) effectively reduces H_2O_2 at the fuel surface, thereby limiting the oxidative dissolution of the UO_2 matrix and promoting the precipitation of oxidized iron phases.

Although H_2 does not react directly with H_2O_2 under repository conditions, experimental and modelling studies have demonstrated that a strong synergistic effect exists between H_2 and Fe(II) [100, 101]. H_2 rapidly scavenges hydroxyl radicals produced during Fe(II)-mediated peroxide decomposition, leading to the formation of atomic hydrogen, a highly reactive reducing species:

$$OH\cdot + H_2 \rightarrow H_2O + H\cdot \quad (6)$$

$$H\cdot + H_2O_2 \rightarrow H_2O + OH\cdot \quad (7)$$

It is assumed that SNF dissolution proceeds at a very low oxidative rate and that oxidized U, Pu, and redox-sensitive fission products are efficiently reduced at the surface of iron-containing components, a concept applicable to most European repository designs [18, 84, 102]. Over the past two decades, extensive experimental evidence has confirmed that H_2 generated by anaerobic corrosion of iron can significantly suppress the radiation-induced oxidative dissolution of the fuel [74, 103-109]. The protective effect of hydrogen on the fuel surface can be attributed to the kinetic activation of H_2 on noble metal ε-particles (e.g., Mo, Ru, Rh, Tc, Pd) present within the spent fuel [110-112]. Numerical modelling has further demonstrated that elevated hydrogen concentrations reduce the steady-state concentration of oxidants near the fuel surface, thereby lowering dissolution rates under repository-relevant conditions [113]. In parallel, studies investigating the interaction of iron and its corrosion products on SNF corrosion show that the presence of iron phases inhibits fuel corrosion and radionuclide release [18, 92, 97]. Recent studies further support the conclusion that the combined presence of Fe(II) and H_2 establishes a robust redox buffer in the repository near-field, significantly limiting oxidative dissolution processes [18, 92, 114]. Consequently, iron corrosion and hydrogen generation are now considered as one of the important key mitigating processes contributing to the long-term stability of spent fuel under disposal conditions

2.8. Radionuclide coprecipitation under disposal-relevant conditions

Following the potential release of radionuclides from SNF due to matrix dissolution, their subsequent behaviour in the near-field environment plays a critical role in determining long-term repository safety. Under disposal-relevant reducing conditions, several geochemical processes can significantly control radionuclide retention and limit their mobility, including solubility limit, sorption (surface complexation and anion exchange), secondary phase formation, and radionuclides coprecipitation [115-118]. Experimental investigation of SNF leaching under hydrogen atmospheres has shown that the aqueous concentrations of U, Pu, and Np initially decrease within the first days to weeks. Subsequently, these concentrations remain very low and constant over extended periods ranging from several months to years [18, 75, 104, 106, 107].

These observations have been interpreted as evidence for the reduction of initially oxidized actinides (pre-oxidized fuel layer) at or near the fuel surface (fuel/groundwater interface), followed by their reprecipitation and coprecipitation as their corresponding reduced amorphous oxides. Such observation suggests that coprecipitation may significantly limit radionuclide release and serve as a mechanism for retaining radionuclides following an initial corrosion of the spent fuel by groundwater under disposal-relevant conditions [119-121].

Coprecipitation of actinides is chemically favoured due to the strong similarities among tetravalent actinide ions. U(IV), Pu(IV), and Np(IV) exhibit comparable ionic radii, identical charges, and similar coordination numbers, and they form oxides with the fluorite crystal structure [122]. These similarities promote the formation of mixed oxide phases or solid solutions. The formation of such solid solutions can further reduce actinide solubility relative to that of the individual end member oxides [123, 124]. In cases where radiolysis-induced reactions lead to the oxidation of spent nuclear fuel, a localized oxidizing condition may develop at the fuel–water interface due to water radiolysis [75-77]. However, reducing conditions are expected to dominate in the near field as a result of redox buffering by repository iron canister materials, leading to the establishment of "redox fronts" [125]. Within these regions, dissolved actinides migrating away from the fuel surface may undergo reduction and subsequent reprecipitation [126]. Once solubility limits are exceeded, they can coprecipitate with each other, most likely occurring at some distance from the fuel surface, where reducing conditions are re-established or within the reducing environment of the far field as first suggested by Bruno et al. in the late 1990s [119-124].

Given the abundance of U in spent fuel, its coprecipitation with other radionuclides within a failed canister is expected to control their individual concentration. Coprecipitation with U, therefore, plays a key role in determining the aqueous concentrations of other actinides such as Pu and Np, as well as redox-sensitive elements within a breached canister. The formation of U-mixed oxides solid solutions incorporating other actinides may act as long-term solubility-controlling solids in HLW repository environments. Retention processes such as coprecipitation can strongly influence the release of radionuclides during spent fuel dissolution under disposal conditions. Improving the understanding of spent fuel interactions under various disposal scenarios is therefore essential for assessing long-term safety in deep repository environments. In this context, investigating actinide oxides coprecipitation under repository-relevant conditions is particularly important because of its relevance to radionuclide immobilization.

Despite substantial progress in this research area, further studies are still required to better understand the long-term evolution of repository redox conditions, secondary phase formation, and groundwater chemistry. Since groundwater intrusion due to canister breach represents the only plausible pathway for radionuclide transport to the biosphere, continued investigation of radiation-induced dissolution processes and their mitigation remains essential. The present thesis contributes to this effort by addressing radionuclide behaviour under disposal-relevant reducing conditions, with particular emphasis on the process governing spent fuel dissolution, actinide oxide coprecipitation, and UO_2 migration in groundwater systems, thereby addressing key remaining knowledge gaps in this field.

3.0. Theory

3.1. Corrosion processes of MOX fuel under geological-disposal conditions

Mixed oxide (MOX) fuel is composed primarily of uranium dioxide (UO_2) and plutonium dioxide (PuO_2). It is widely used in thermal light water reactors (LWR), and, after irradiation, two management pathways are considered for the back end of the spent MOX fuel. It may either be reprocessed for further energy recovery in advanced or future reactor systems or considered for direct disposal in DGR as part of the HLW inventory [127, 128].In several countries, direct disposal of spent MOX fuel is regarded as a practical option, given the technical and economic constraints associated with the limited mono-recycling potential of MOX fuel in LWR [70, 129].

Industrially, commercial MOX fuel is mostly fabricated using the MIMAS (MIcronized MASter blend) process, which involves diluting a plutonium-rich UO_2–PuO_2 master blend with UO_2 powder to achieve the desired plutonium content [130]. Because of this fabrication route, MIMAS-MOX fuel exhibits a heterogeneous microstructure [130-132]. This microstructure is typically described as comprising three distinct zones: (i) a UO_2-rich matrix with low Pu content, (ii) a Pu-rich agglomerate zone, and (iii) a surrounding coating zone characterized by an intermediate Pu content [130, 131].

SNF exhibits a more complex heterogeneous microstructure with different phases, consisting of UO_2 matrix, containing dissolved and segregated actinides (Pu, Np, Am), metallic and oxide fission product inclusions, fission gas bubbles, grain boundaries, and high active rim zone structure [46]. At extended repository timescales, typically beyond several hundred to a few thousand years after repository closure, the radiation field of SNF will be dominated by alpha-emitting actinides such as Np, Pu, Am, and Cm. The contributions of beta and gamma radiation decline rapidly as short- and intermediate-lived fission products and actinides decay, since these radionuclides are responsible for nearly all β- and γ-emissions that dominate the activity of “young” spent fuel available today. As a result, alpha radiation would persist over geological timescales [76, 77, 85, 133, 134].

Alpha radiation is high LET (Linear Energy Transfer) radiation and produces mainly molecular radiolysis products. Among the formed radiolytic species, H_2O_2 has been identified as the dominant oxidizing species controlling fuel corrosion and is responsible for oxidative fuel dissolution under anoxic disposal relevant conditions [69]. The continuous generation of H_2O_2 at the fuel-water interface or fuel surface promotes oxidation of U(IV) to U(VI), thereby enhancing uranium solubility and matrix dissolution [69, 84, 85]. The overall mechanism of oxidative dissolution occurs through sequential surface oxidation of U, the aqueous dissolution of the uranyl species, and the formation of secondary solid phases [135, 136].

In MOX fuel, the presence of Pu increases alpha activity (especially in the Pu-rich agglomerates), which could lead to locally enhanced radiolytic yields and impact the fuel dissolution [132, 136, 137]. Compared to conventional UO_2 fuel, MOX fuel exhibits a higher fraction of Pu, compositional heterogeneity, microstructural complexity, and differences in fission density, all of which could influence corrosion behaviour in a groundwater saturated scenario [127, 135]. While the alteration or corrosion of UO_2 spent fuel has been extensively investigated, experimental data addressing MOX fuel corrosion under disposal-relevant conditions remain comparatively limited. Under DGR conditions, the corrosion behaviour of MOX fuel will be governed by a combined

effect of radiolytic reactions, redox processes, and fuel microstructure. Although the fundamental corrosion mechanism is expected to be similar to that of UO_2 fuel, the inherent microstructural heterogeneity of MOX fuel can affect its alteration behaviour. Experimental studies have shown that this heterogeneity may result in a higher initial fractional release of actinides and fission gas from MOX fuel compared with homogeneous UO_2 fuel [132, 136, 137-140]. Under aerated conditions MOX fuel dissolves about 7 times faster than UO_2 fuel of the same burnup [110].

However, long-term leaching experiments performed on irradiated and unirradiated MOX fuel under reducing conditions and in the presence of dissolved hydrogen have shown that oxidative dissolution is strongly suppressed [127, 135, 136]. These studies report very low steady-state aqueous concentrations of U and Pu, indicating limited matrix corrosion and negligible contribution from plutonium-rich agglomerates [127, 135, 136]. Although the heterogeneous microstructure of MOX fuel, characterized by Pu-rich islands embedded within a UO_2 matrix, may lead to enhanced initial release during early contact with water, long-term dissolution rates may remain low under reducing conditions representative of deep geological disposal.

MOX fuel provides a valuable and conservative approach for studying radiation-induced processes relevant to the long-term behaviour of all spent nuclear fuels under disposal conditions. Radiolysis of water adjacent to MOX fuel is dominated by alpha particles, which deposit energy over very short ranges and generate high local concentrations of radiolytic species at the fuel surface. Previous studies have shown that alpha radiolysis is the principal driver of oxidative dissolution under anoxic conditions at long timescales [76, 77, 134, 137]. Since MOX fuel intrinsically reproduces an alpha-dominated radiation field, it allows investigation of key corrosion mechanisms without relying on external alpha sources or α-doped UO_2 fuel. From a safety assessment perspective, the use of MOX fuel in corrosion and dissolution studies is therefore justified not only by its relevance as an actual waste form, but also by its role as a conservative analogue for the long-term behaviour of spent nuclear fuel in general. Studies from MOX fuel leaching can be used to gain insight into the behaviour of spent MOX fuel in case of water intrusion canister failure; likewise, it can be applied to the evaluation of spent fuel performance during alpha-dominated repository phases, thereby reducing uncertainties associated with long-term source term predictions.

3.2. Groundwater chemistry, iron corrosion, and uranium speciation under repository-relevant conditions

The long-term behaviour of SNF in a DGR is governed by coupled geochemical processes involving groundwater composition, redox evolution, and interactions with engineered barrier materials. In the KBS-3 disposal concept, carbon steel components, most notably the cast iron insert of the copper canister, are expected to corrode in the event of groundwater intrusion [13, 141]. The corrosion of metallic iron plays a central role in establishing redox conditions, modifying solution chemistry, and ultimately controlling radionuclide mobility over geological timescales [141].

Groundwater chemistry in crystalline bedrock environments evolves toward Na–Cl dominated compositions with varying contributions from Ca^{2+}, Mg^{2+}, carbonate, and sulfate [142, 143]. Salinity ranges from fresh to brackish conditions depending on depth, and repository groundwaters are typically characterized by near neutral to mildly alkaline pH and very low dissolved oxygen concentrations [142-144]. Following repository closure, oxygen introduced during construction is rapidly consumed by reactions with ferrous minerals and microbial activity, establishing strongly

reducing conditions [13, 145]. Under these anoxic conditions, metallic iron corrodes through anaerobic reaction, releasing dissolved Fe(II), generating H_2, and increasing pH in the near-field environment [18]. Depending on groundwater composition and redox conditions, corrosion of iron can lead to the formation of secondary iron-bearing phases such as magnetite, siderite, green rusts, ankerite, and chukanovite [18, 91, 92, 95, 146]. These corrosion products can contribute to maintaining reducing conditions and provide reactive surfaces capable of influencing radionuclide behaviour through adsorption, surface complexation, redox reactions, and coprecipitation processes [18, 147, 148].

U mobility in groundwater is strongly controlled by its oxidation state and aqueous speciation [149, 150]. Under oxidizing conditions, U predominantly occurs as the hexavalent uranyl ion (UO_2^{2+}) [150]. In carbonate-containing groundwaters, uranyl forms highly stable and soluble carbonate complexes, including $UO_2(CO_3)_2^{2-}$ and $UO_2(CO_3)_3^{4-}$ which dominate speciation under neutral to alkaline conditions [149, 151]. The presence of Ca further modifies U chemistry through the formation of ternary Ca–uranyl–carbonate complexes, such as $CaUO_2(CO_3)_3^{2-}$ and $Ca_2UO_2(CO_3)_3(aq)$ [152, 153], as shown in the equation below:

$$UO_2(CO_3)_3^{4-} + Ca^{2+} \rightleftharpoons CaUO_2(CO_3)_3^{2-}, \qquad \log k = 5.2 \pm 0.2 \qquad (8)$$

$$UO_2(CO_3)_3^{4-} + 2\,Ca^{2+} \rightleftharpoons Ca_2UO_2(CO_3)_3, \qquad \log k = 9.0 \pm 0.4 \qquad (9)$$

These complexes enhance uranium solubility and reduce its tendency to adsorb onto mineral surfaces, thereby increasing mobility in subsurface environments [152-154].

However, under reducing conditions established by iron corrosion, U can undergo reduction from the relatively soluble U(VI) state to sparingly soluble U(IV), leading to the formation of amorphous UO_2(am) [155, 156]. Both metallic iron and dissolved Fe(II) have been shown to promote U(VI) reduction, either directly at the metal surface or via homogeneous and surface-mediated pathways [157, 158]. Fe(II)-bearing minerals such as magnetite and green rusts can further facilitate reduction, thereby lowering the solubility of U and limiting its migration [159, 160]. The efficiency and kinetics of U(VI) reduction are strongly influenced by aqueous speciation. Ca–uranyl–carbonate complexes exhibit increased thermodynamic stability and kinetic resistance toward homogeneous reduction by dissolved Fe(II) [161, 162]. Surface-mediated processes may partially overcome these limitations, but the presence of calcium has been shown to inhibit both abiotic and microbially mediated reduction pathways, likely due to steric effects and stabilization of the ternary complexes [161, 162]. Consequently, the interplay between carbonate complexation and iron-induced reduction represents a critical control on uranium mobility.

In summary, U behaviour in repository environments is governed by the coupled effects of groundwater composition and iron corrosion processes. Carbonate enhances U solubility under oxidizing conditions, whereas iron corrosion establishes reducing conditions and provides reactive surfaces that promote immobilization through reductive precipitation. Likewise, Ca forms strong complexes with uranyl carbonate and increases their stability towards reduction. Understanding the balance between these competing mechanisms is essential for assessing the long-term safety performance of deep geological repositories, and it forms part of the conceptual basis for the experimental investigations presented in this thesis.

3.3. Coprecipitation and partitioning behavior in solid-solution systems

Coprecipitation is a fundamental chemical process that involves the simultaneous precipitation of solid compounds from a solution, often resulting in the incorporation of minor elements into the host solid precipitates. This phenomenon is of particular importance in geochemical and radiochemical processes, where it can strongly influence the retention and long-term mobility of radionuclides under disposal-relevant conditions [119 -121]. Coprecipitation is generally achieved by adding a base (NaOH) to aqueous metal solutions to promote solid formation [163]. Depending on the chemical system, coprecipitation may be carried out at ambient or elevated temperatures, and in redox-sensitive environments, under an inert atmosphere to prevent oxidation [164, 165].

During coprecipitation, dissolved ions are removed from solution and incorporated into the growing solid through processes such as nucleation, crystal growth, and aggregation [166, 167]. The extent of incorporation depends on several physicochemical parameters, including pH, ionic strength, temperature, total metal concentrations, aqueous complexation, precipitation kinetics, and the chemical similarity between the major and minor components [163, 168]. Similarities in ionic radius, charge, and coordination environment enhance the likelihood that minor components become structurally integrated into the host solid [121-124].

When coprecipitation leads to the formation of a single mixed solid phase, the resulting material can be described as a solid solution. Solid solutions can be described as homogeneous solids in which two or more components are mixed at the atomic or molecular scale while preserving a common crystal or amorphous structure, though slight variations in lattice parameters can occur [123, 124]. While this concept is commonly used in metallurgy, it is equally applicable to oxide and hydroxide systems relevant to actinide chemistry.

The distribution of components between the aqueous phase and the coprecipitated solid is commonly described using empirical partitioning laws [168]. These laws relate the molar fractions of a minor component (A) and a major component (B) in the solid to their concentrations in solution and provide insight into whether equilibrium is attained with the bulk of the solid or is restricted to its surface. If thermodynamic equilibrium is established between the aqueous phase and the bulk solid, the system follows the homogeneous distribution law proposed by Berthelot and Nernst [120, 169]. This relationship is expressed as:

$$\frac{[\mathrm{A}]_{(\mathrm{s})}}{[\mathrm{B}]_{(\mathrm{s})}} = \mathrm{D}\,\frac{[\mathrm{A}]_{(\mathrm{aq})}}{[\mathrm{B}]_{(\mathrm{aq})}} \qquad (10)$$

where $[A]_{(aq)}$and $[B]_{(aq)}$denote the total aqueous concentrations of the minor and major components, respectively, $[A]_{(s)}$and $[B]_{(s)}$are their mole fractions in the solid phase, and $D$is the homogeneous distribution coefficient. Under ideal conditions, this coefficient can be related to the ratio of the solubility product constants of the corresponding end-member solids:

$$\mathrm{D} = \frac{\mathrm{K}_{\mathrm{sp}}^{\mathrm{B}}}{\mathrm{K}_{\mathrm{sp}}^{\mathrm{A}}} \qquad (11)$$

Homogeneous solid solutions formed under these conditions are characterized by uniform composition and the absence of concentration gradients, reflecting a true thermodynamic equilibrium [170]. In contrast, it is possible that coprecipitation systems may not achieve complete equilibration within the solid phase, whereby the minor components can be unevenly distributed within the host lattice. Such heterogeneous solid solutions may exist in a metastable equilibrium

with an aqueous solution, displaying concentration gradients due to limited solid-state diffusion and slow structural rearrangement [170]. In such cases, distribution equilibrium may be limited to the solid–solution interface, leading to heterogeneous incorporation of the minor component within the host lattice. This behavior is described by the logarithmic distribution law proposed by Doerner and Hoskins [171]:

$$\log\left(\frac{[\mathrm{A}]_{(\mathrm{surface})}}{[\mathrm{B}]_{(\mathrm{surface})}}\right) = \mathrm{k}\,\log\left(\frac{[\mathrm{A}]_{(\mathrm{aq})}}{[\mathrm{B}]_{(\mathrm{aq})}}\right) \qquad (12)$$

where $[A]_{(surface)}$ and $[B]_{(surface)}$ represent the mole fractions of the minor and major components at the solid surface, and k is the heterogeneous distribution coefficient.

For actinide-bearing systems such as SNF, coprecipitation formation could play an important role in controlling radionuclide migration within the geosphere. This thesis investigates the formation of U(IV)-based hydrous oxide phases and their capacity to incorporate other actinides (Pu, Np) under repository-relevant conditions. Specifically, the coprecipitation and solubility behaviour of Ce_xU_{1-x} and $Np_xPu_yU_{1-x-y}$ phases were evaluated to assess the extent to which these materials approach equilibrium solid-solution behaviour under conditions relevant to geological disposal.

3.4. Solubility and hydrolysis of actinide hydrous oxides (U, Pu, and Np)

Due to their similar charge, ionic radii, and coordination chemistry, tetravalent U, Pu, and Np exhibit comparable hydrolysis behaviour in aqueous media [19, 35]. Their chemistry can therefore be described using a generic actinide representation (An = U, Pu, Np), where the hydrolysis reaction can be written as:

$$\mathrm{x\,An^{4+} + y\,OH^- \rightleftharpoons An_x(OH)_y^{(4x-y)}} \qquad (13)$$

with x = 1–4, leading to the formation of mononuclear hydroxo complexes $An(OH)^{3+}$, $An(OH)_2^{2+}$, $An(OH)_3^{+}$, and $An(OH)_4(aq)$ [35, 172-174].Under neutral to alkaline conditions, tetravalent actinides precipitate as amorphous hydrous oxides, commonly represented as $AnO_2 \cdot xH_2O(am)$, which are often referred to as $An(OH)_4(s)$. The solubility-controlling equilibrium can be expressed as:

$$\mathrm{An(OH)_4(s) \rightleftharpoons An^{4+} + 4OH^-} \qquad (14)$$

with the solubility product:

$$\mathrm{K_{sp} = \{An^{4+}\}\{OH^-\}^4} \qquad (15)$$

In an aqueous system, where no complexation with other inorganic ligands or colloidal species occurs, the total dissolved actinide equilibrium concentration is given by:

$$\mathrm{[An(IV)]_{total} = [An^{4+}] + \sum[An_x(OH)_y^{(4x-y)}]} \qquad (16)$$

Tetravalent U is known for its very low solubility in aqueous systems, and it has a strong tendency to undergo hydrolysis. UO_2 can dissolve under acidic conditions, with the dominant aqueous species being U^{4+} and $U(OH)^{3+}$ at low pH values. When the solution pH is below 2, U remains

mostly dissolved, however, as the pH increases above this threshold, hydrolysis reactions become significant, leading to the formation of various hydroxide species [173]. Hydrolysis involves the interaction of metal ions with water molecules, releasing protons and generating hydrolyzed complexes [174]. The extent and type of hydrolysis products depend strongly on the charge and ionic radius of the metal ion [174].

For U(IV), mononuclear hydroxide species are formed through the reactions:

$$x\,U^{4+} + y\,H_2O \rightleftharpoons U_x(OH)_y^{4x-y} + y\,H^+ \qquad (17)$$

where x = 1 corresponds to mononuclear complexes. Specific hydrolysis reactions include:

$$U^{4+} + H_2O \rightleftharpoons U(OH)^{3+} + H^+ \qquad (18)$$
$$U^{4+} + 2H_2O \rightleftharpoons U(OH)_2^{2+} + 2H^+ \qquad (19)$$
$$U^{4+} + 3H_2O \rightleftharpoons U(OH)_3^{+} + 3H^+ \qquad (20)$$
$$U^{4+} + 4H_2O \rightleftharpoons U(OH)_4(aq) + 4H^+ \qquad (21)$$

The overall formation constant for each species is defined as:

$$\beta_{1,x} = \frac{\{U(OH)_x^{4-x}\}}{\{U^{4+}\}\{OH^-\}^x} \qquad x = 1,..,4 \qquad (22)$$

Where the index1, x represents a mononuclear complex formed in the hydrolysis step x.At near-neutral groundwater pH (7–9), amorphous UO_2 reaches equilibrium concentrations on the order of ~3×10^{-9} M [35]. The solubility of UO_2(am) is governed by equilibria between the solid phase and dissolved species:

$$UO_2(am) + 4H^+ \rightleftharpoons U^{4+} + 2H_2O \qquad \log K_{s,0}^0 = 1.5 \qquad (23)$$
$$U^{4+} + 4H_2O \rightleftharpoons U(OH)_4(aq) + 4H^+ \qquad \log \beta_{0,4}^0 = -10.0 \qquad (24)$$
$$UO_2(am) + 2H_2O \rightleftharpoons U(OH)_4(aq) \qquad \log K_{s,4}^0 = -8.5 \qquad (25)$$

At higher pH values, the formation of neutral $U(OH)_4$ species dominates the solubility equilibrium. Tetravalent uranium precipitates as an amorphous hydrous oxide, $UO_2 \cdot xH_2O$(am), often referred to as uranium hydroxide, $U(OH)_4$(s). Its dissolution can be represented as:

$$U(OH)_4(s) \rightleftharpoons U^{4+} + 4OH^- \qquad (26)$$

The corresponding solubility product is:

$$K_{sp} = \{U^{4+}\}\{OH^-\}^4 \qquad (27)$$

The total U concentration, (where no complexation with other inorganic ligands or colloidal species occurs) which determines the effective solubility of the solid, includes both the free ion and all its hydrolyzed species:

$$[\mathrm{U(IV)}]_{\mathrm{total}} = [\mathrm{U}^{4+}] + \sum[\mathrm{U(OH)}_{\mathrm{y}}^{4x-y}] \qquad (28)$$

Pu in its tetravalent state exhibits similar hydrolysis behavior to U(IV) and is characterized by low solubility and a strong tendency to form hydrous oxides. However, predicting Pu solubility in aqueous solution is complicated by the possibility of simultaneous formation of different oxidation states [22]. PuO_2 can dissolve in acidic solutions, and at low pH, with Pu^{4+} as the dominant species. When pH ≤ 2, Pu remains mostly in solution, however, at pH > 2, Pu hydrolyzes to form mononuclear hydroxide species such as $Pu(OH)^{3+}$, $Pu(OH)_2{}^{2+}$, $Pu(OH)^{3+}$, and $Pu(OH)_4$(aq) [22, 28, 35].

When compared to the other Pu oxidation states, Pu^{4+} has the highest tendency to form hydrolysis products. However, as the hydrolysis proceeds, polynuclear hydroxide species are formed if the concentration of Pu is sufficiently high, which, as they grow in size, are commonly referred to as colloids [28]. The formation of colloids, however, can increase the solubility of Pu as they can remain in solution up to a size of about 10 nm before they precipitate. The hydrolysis reactions for Pu(IV) are similar to those of U. Numerical values for the Pu(IV) hydrolysis constants have been described by Neck and Kim [35]. At neutral to slightly alkaline pH (7–9), PuO_2 reaches a solubility of ~$10^{-10.4}$M [172]. The solubility is controlled by the equilibrium:

$$\mathrm{PuO_2(am)} + 4\mathrm{H}^+ \rightleftharpoons \mathrm{Pu}^{4+} + 2\mathrm{H_2O} \quad \log \mathrm{K^o_{s,0}} \approx 1.3 \qquad (29)$$

Tetravalent Pu precipitates as an amorphous hydrous oxide $PuO_2.xH_2O$ or as $Pu(OH)_4$(s), and its dissolution can be expressed as:

$$\mathrm{Pu(OH)_4(s)} \rightleftharpoons \mathrm{Pu}^{4+} + 4\mathrm{OH}^- \qquad (30)$$

The solubility product for the Pu(IV) hydrous oxide is:

$$\mathrm{K_{sp}} = \{\mathrm{Pu}^{4+}\}\{\mathrm{OH}^-\}^4 \qquad (31)$$

The total Pu concentration, considering its hydrolysis, can also be illustrated as:

$$[\mathrm{Pu(IV)}]_{\mathrm{total}} = [\mathrm{Pu}^{4+}] + \sum[\mathrm{Pu(OH)}_{\mathrm{n}}^{4-n}] \qquad (32)$$

The solubility of NpO_2 in aqueous systems is generally very low and is strongly controlled by pH, redox conditions, and the presence of complexing ligands [35]. Under reducing conditions, dissolved Np predominantly exists as $Np^{4+,}$ which undergoes extensive hydrolysis even at relatively low pH values. The hydrolysis reactions of Np(IV) are similar to those observed for other tetravalent actinides such as Pu(IV) and U(IV) [35, 172].

In acidic solutions (pH ≤ 2), Np^{4+} is the dominant aqueous species, at higher pH values (pH > 2), hydrolysis reactions occur, leading to the formation of species such as $Np(OH)^{3+,}$ $Np(OH)_2{}^{2+}$, $Np(OH)^{3+}$, and $Np(OH)_4$(aq) [32, 33, 35].At higher pH values, polymeric and colloidal species may also form, which can further influence the apparent solubility of NpO_2. These hydrolysis reactions play an important role in controlling the aqueous speciation of Np and consequently its mobility in groundwater systems [175]. The solubility of NpO_2(am) at neutral pH is approximately ~10^{-9} M [172].

The dissolution equilibrium can be expressed as:

$$NpO_2(am) + 4H^+ \rightleftharpoons Np^{4+} + 2H_2O \qquad (33)$$

The strong tendency of Np(IV) to undergo hydrolysis and form polymeric species results in extremely low dissolved concentrations, particularly under neutral to alkaline conditions, which are relevant to nuclear waste repository environments [35].

3.5. Thermodynamic model/approach for trivalent (Ce or Pu) hydroxide co-precipitation system

For each chemical component in the studied coprecipitation system, at equilibrium, the chemical potential (μ) must be equal in the solid and in the aqueous phase μ^s $(An(OH)_3) = \mu^{aq}$ $(An(OH)_3)$.

In our investigated system, the measured concentrations in solution (U-Ce and U-Pu-Np studies) in equilibrium with their corresponding mixed oxide phases were evaluated over two pH ranges (low and high pH regions), which correspond to regions where different aqueous species are expected to dominate.

In the low acidic region, the dissolution of $Ce(OH)_3$(s) or $Pu(OH)_3$ (s) is governed primarily by the reaction below:

$$An(OH)_3(am,s) + 3\ H^+ \rightleftharpoons An^{3+} + 3\ H_2O(l) \qquad (34)$$

where An represents Ce(III) or Pu(III). Within this pH range, the formation of hydrolyzed Ce(III) or Pu(III) species is not expected to occur. The thermodynamic equilibrium constant for $Ce(OH)_3$ or $Pu(OH)_3$(s) in the coprecipitates and the solution can be expressed as :

$$*K^0_{s0} = \frac{\{An^{3+}\}a_w^3}{\{H^+\}^3\ a_{An(OH)_{3(s)}}} \qquad (35)$$

where $a_{An\ (OH)_3(s)}$ represents the activity of $Ce(OH)_3$(s) or $Pu(OH)_3$(s) in their respective solid phase, and curly brackets denote activities in solution.

Under constant ionic strength conditions (1 M $NaClO_4$) as in the U-Ce coprecipitation study, the activity coefficients and water activity are incorporated into a conditional solubility product, allowing the equilibrium to be expressed in terms of measurable aqueous concentrations.

$$\log [Ce^{3+}] = \log \left(*K^0_{s0} \frac{\gamma^3_{H^+}}{\gamma_{Ce^{3+}}\ a_w^3}\right) - 3(-\log[H^+]) + \log a_{Ce(OH)_{3(s)}} \qquad (36)$$

$$\log [Ce^{3+}] = \log *K_{s0} - 3(-\log[H^+]) + \log a_{Ce(OH)_{3(s)}} \qquad (37)$$

While in the U-Pu-Np coprecipitation study, where 0.01M NaCl was used, the activity of water in such dilute solution is close to one. The concentration of Pu in equilibrium with the 0.01M NaCl can be expressed as:

$$\log \{Pu^{3+}\} = \log *K^0_{s0} - 3\ pH + \log a_{Pu(OH)_{3(s)}} \qquad (38)$$

At constant temperature, pressure, and composition, the activity of the solid phase remains unchanged if its Gibb´s free energy is constant. Although aging processes typically reduce the free energy of solid precipitates, this effect was negligible over the 30-day equilibration period considered in both co-precipitation studies. The activity of $An(OH)_3(s)$ in the solid solution can be estimated by introducing a solid phase composition-dependent constant denoted K_x, where x represents the mole fraction of Ce or Pu in the solid:

$$\log K_x = \log {}^*K_{s0} + \log a_{An(OH)_3(s)} \qquad (39)$$

The constant K_x equals ${}^*K_{s0}$ when $An(OH)_3(s)$ is in its standard state, i.e. pure $An(OH)_3(s)$. The constant K_x can be expressed in this acidic pH range by combining equations 37 and 39:

$$\log [An^{3+}] = \log K_x - 3\ pH \qquad (40)$$

or combining equations 38 and 39:

$$\log\{An^{3+}\} = \log K_x - 3\ pH \qquad (41)$$

For the mixed solid phases formed by co-precipitation, the activity coefficients of the solid phase (λ) were derived from the relationship between the activity and composition expressed as:

$$a_{An(OH)_3(s)} = x\ \lambda_{An(OH)_3(s)} \qquad (42)$$

At higher basic pH values, assuming that $An(OH)_3(aq)$ is the dominant species in solution, the total dissolved concentration can be expressed as:

$$\log [An]_T = \log {}^*K_{s0} + \log {}^*\beta_3 \qquad (43)$$

where ${}^*\beta_3$ is the conditional formation constant corresponding to the equilibrium:

$$An^{3+} + 3\ H_2O(l) \rightleftharpoons An(OH)_3(aq) + 3\ H^+ \qquad (44)$$

The Ce or Pu concentrations in equilibrium with the co-precipitated solids are expected to be lower than those in equilibrium with their respective pure hydroxides ($Ce(OH)_3(s)$ and $Pu(OH)_3(s)$), due to the reduced activity of the hydroxide component within the mixed solid phase. In this case, the following relation is obtained:

$$\log [An] = \log K_x + \log {}^*\beta_3 \qquad (45)$$

4.0. Materials and Methods

This chapter describes the materials, experimental procedures, and analytical methods used throughout this thesis. The methodology combines all experimental approaches from published articles and submitted manuscripts.

4.1. Experimental strategy and conceptual framework

The experimental work in this thesis was designed to investigate the behavior of U and other transuranic actinides (Pu, Np) under reducing conditions relevant to the deep geological disposal of SNF. Three complementary experimental strategies were employed:

1. Reductive precipitation of U(IV): The interaction between dissolved U(VI) and corroding metallic iron was investigated in simulated groundwater solutions under anoxic conditions. The effect of Ca-uranyl carbonato complexes on the reductive precipitation of U(VI) to U(IV) on the iron surface was examined.

2. Long-term leaching experiments: Leaching experiments were conducted using unirradiated MIMAS-MOX fuel in the presence of metallic iron and, in subsequent experiments, with iron corrosion products (magnetite, chukanovite), both of which were carried out in the presence of synthetic Swedish Forsmark groundwater under an Ar atmosphere. These studies investigate the effect of repository reductants and iron corrosion products on the oxidative dissolution of MOX fuel pellets.

3. Co-precipitation and solid-solution formation: The initial studies focused on U(IV) and Ce(III), with Ce used as a non-radioactive surrogate for Pu. These experiments aimed to develop and validate the methodology for actinide oxides co-precipitation studies, to determine their solubilities and the nature of the solid solution formed. The U-Ce study was carried out in 1 M $NaClO_4$ because Ce(III) hydrolysis and the solubility of $Ce(OH)_3(s)$ were studied in this medium, while $UO_2(s)$ solubility in 1 M NaCl was used for data comparison.

In the subsequent study, co-precipitation experiments of Pu and Np amorphous oxides with UO_2(am, hyd) were conducted to investigate the solubility behaviour, kinetics of equilibration, and nature of the solid solution formed. The U-Pu-Np coprecipitation study was carried out in diluted 10 mM NaCl solutions and compared to $UO_2(s)$ solubility or $PuO_2(s)$ reductive dissolution at a similar ionic strength.

All experiments were conducted under anoxic and reducing conditions to preserve actinide oxidation states and to simulate repository-relevant environments. Anoxic conditions were maintained using an inert-atmosphere glove box (N_2 atmosphere, O_2 < 1 ppm), while reducing conditions were achieved through the addition of a chemical reductant (sodium dithionite) where necessary. Experimental work involving U, Pu, Np, and MOX fuel handling was performed in a dedicated fumehood and inert-atmosphere glove boxes.

4.2. Chemicals and solutions

All solutions used in all the experiments were prepared with ultrapure water (18.2 MΩ·cm, Milli-Q Advantage, Merck). Before use in all experiments, the water was sparged with high-purity nitrogen gas (99.99%) for some hours to eliminate dissolved oxygen. The deoxygenated water was then transferred into an argon-controlled glove box, purged with the argon box atmosphere, and

finally stored in the glove box. Analytical-grade reagents were used throughout the experiments. Acids (HCl) and bases (NaOH) were used for pH adjustment, and HNO_3 (Suprapur grade) was used for analytical dilution. Sodium dithionite ($Na_2S_2O_4$) (Sigma-Aldrich, Merck) was used as a reducing agent where applicable.

For the study on Ca–uranyl–carbonato complexes reduction in the presence of iron, a 10 ppm U(VI) stock solution was first prepared and subsequently diluted with synthetic groundwater as shown in Table 1 to achieve a U concentration of 1 ppm (4.2×10^{-6} M).

For the U–Ce coprecipitation experiments, a U(IV) stock solution (~0.46 M) was prepared by dissolving reactor-grade U metal in 12 M HCl (37% ACS grade, Sigma-Aldrich, Merck). In parallel, 4.6573 g of cerium (III) chloride heptahydrate ($CeCl_3 \cdot 7H_2O$, 99.9% purity, Sigma-Aldrich, Merck) was dissolved in 100 mL of 10 M HCl to obtain a 0.125 M Ce stock solution.

Sodium dithionite ($Na_2S_2O_4$, Sigma-Aldrich, Merck) was prepared at concentrations of 10 mM and 20 mM, while a 1 M carbonate-free NaOH solution was obtained using 1 M NaOH Titrisol ampoules (Sigma-Aldrich, Merck). An ionic medium of 1.0 M sodium perchlorate ($NaClO_4$) was prepared for solubility experiments. The $NaClO_4$ stock solution (4.61308 mmol g^{-1}) was synthesized from reagent-grade perchloric acid and sodium carbonate following established procedures at Kungliga Tekniska högskolan (KTH) [176]. To prepare the 1 M working solution, an accurately weighed portion of the stock containing 1 mol of $NaClO_4$ (216.77 g) was transferred to a 1 L volumetric flask and diluted to volume with distilled water.

For the coprecipitation experiments of UO_2 with Pu and Np. U(IV), Np(IV), and Pu(IV) stock solutions were prepared under strictly inert conditions to preserve redox stability. The U(IV) stock solution (~1.33 M) was prepared using the same method described above. The Np(IV) stock solution was obtained by dissolving 0.42 g of $^{237}NpO_2$ in concentrated HCl with controlled heating. Similarly, the Pu(IV) stock solution was prepared by dissolving 0.6365 g of $^{239}PuO_2$ in concentrated HCl with controlled heating. Small, carefully regulated additions of HNO_3 were used to facilitate dissolution of Pu and Np without altering the oxidation state of the actinides. U, Pu, and Np solutions were filtered to remove residual solids and stored in sealed, opaque containers under an inert atmosphere to ensure redox stability for subsequent experiments.

4.2.1. Synthetic groundwater and model solutions

Synthetic groundwater solutions were prepared using ≥ 99.0% ACS reagent-grade chemicals (Sigma-Aldrich, Merck). Two site-specific synthetic groundwaters representative of repository depth at the Forsmark site, designated as 01D and 02A, were prepared according to reported compositions (Table 1) [177]. In addition, two simplified synthetic groundwater compositions referred to as 10-2 and 10-2-Ca were investigated. The simplified groundwater "10-2" consists of 10 mM NaCl and 2 mM. To specifically assess the effect of Ca, 0.526 mM $CaCO_3$ was added exclusively to the "10-2-Ca" solution.

For the autoclave experiments conducted under an Ar atmosphere, without metallic iron, a simplified groundwater composed of 10 mM NaCl and 2 mM $NaHCO_3$ was used, prepared from ACS reagent grade chemicals (Sigma Aldrich ≥ 99.9%). The synthetic Forsmark groundwater solution used in the autoclave experiments conducted in the presence of Fe(s) and magnetite/chukanovite, using synthetic Forsmark groundwater (02A), was prepared according to the site-specific compositions listed in Table 1, using ≥99.0% ACS reagent-grade salts.

The prepared groundwater was purged with argon for several hours before experiments and transferred under inert conditions to prevent oxidation. The amounts of reagents/chemicals used in its production are given in the Appendix. The compositions of all four groundwater models are detailed in Table 1.

Table 1. Chemical compositions of the synthetic groundwaters. Concentrations in unit mmol/L.

Ground-water	$[Na^+]$	$[K^+]$	$[Ca^{2+}]$	$[Mg^{2+}]$	$[HCO_3^-]$	$[Cl^-]$	$[SO_4^{2-}]$	$[Br^-]$	$[F^-]$	[Si]	$[Fe^{2+}]$	$[Mn^{2+}]$	$[Sr^{2+}]$
01D	77.02	0.187	45.91	0.448	0.280	168.56	0.324	0.581	0.061	0.152	0.014	0.0016	0.237
02A	96.57	0.931	22.21	10.04	2.065	148.91	5.275	0.304	0.077	0.216	0.041	0.0377	0.099
10-2	12.00	0	0	0	2.000	10.00	0	0	0	0	0	0	0
10-2-Ca	10.47	0	0.526	0	2.000	9.00	0	0	0	0	0	0	0

4.3. Materials

4.3.1. Unirradiated MIMAS-MOX Fuel

An unirradiated 10 wt.% Pu MIMAS-MOX fuel pellet produced at the MELOX facility (Marcoule, France) through the MIMAS (MIcronized MASterblend) process was used for all the autoclave leaching experiments. The pellet had a density of approximately 95% of the theoretical density and a specific alpha activity of 1.79 GBq g^{-1}. The original pellet was sectioned into cylindrical slices, and two of these slices with masses 1.6657 g and 1.6565 g were used in the autoclave experiments.

MIMAS-MOX fuel exhibits a heterogeneous microstructure consisting of a UO_2 matrix, Pu-rich agglomerates, and an intermediate Pu-enriched coating zone, originating from the fabrication process. Before each experiment, the pellets were polished using 2400-grit SiC paper and annealed for 5 h at 1200 °C (with a 20 ºC/min heating and cooling rate) in an Ar + 5% H_2 atmosphere inside a graphite furnace (Thermal Technology 1000–2560-FP20), to remove any pre-oxidized surface layer formed during their long storage. Additional details on the MOX fuel used in these studies are provided in the articles included in this thesis.

Table 2. Composition and dimensions of the used 10 wt.% MIMAS-MOX pellets.

Oxide composition			Pu/Am isotopic composition		Dimensions	
UO_2	PuO_2	AmO_2	June 2019		Diameter	Height
89.20 wt.%	10.17 wt.%	0. 63 wt.%	^{238}Pu	1.32%	8.08 mm	3.27 mm
			^{239}Pu	64.37%		
			^{240}Pu	26.60%		
			^{241}Pu	2.54%		
			^{242}Pu	5.05%		
			^{241}Am	0.12%		

4.3.2. Synthesized chukanovite

For the leaching experiment conducted in the presence of chukanovite, synthesized chukanovite was prepared from a 0.22 M $FeCl_2$, 0.20 M NaOH, and 0.18 M Na_2CO_3 solution. The stoichiometric conditions for the direct formation of chukanovite were adopted from Chen et al. [178], with $R = [Fe^{2+}]/[OH^-] = 1.1$ and $R' = [CO_3^{2-}]/[OH^-] = 0.9$.

4.3.3. Iron foils, iron powder, and magnetite

Iron foils with ≥ 99.99 % purity (Thermo Scientific Alfa Aesar) of ~ 0.1 mm thickness and ~1.56 cm^2 surface area, weighing 0.125 g, were used in this experiment. The iron foils were polished with a #1200 grit (FEPA-P) Sic sandpaper in an inert-gas glovebox atmosphere to remove any pre-oxidized layer before the experiments. The iron foil was rinsed in ethanol and ultrasound cleaned for a few minutes before use in the autoclave. 2 g of iron powder (10 μm, ≥ 99.9 % metal basis (Sigma -Aldrich, Merck) was also added to the autoclave for the leaching experiment in the presence of metallic iron. Commercial magnetite (Sigma-Aldrich, < 5 μm mesh) was used for the autoclave leaching experiment conducted in the presence of magnetite.

4.3.4. Stainless steel autoclaves

Leaching experiments were conducted under an Ar atmosphere using modified Parr 4760 pressure vessels. For experiments carried out in the absence of metallic iron, a 0.5 L autoclave vessel was utilized, in which the dip tube of the autoclave was replaced with a PEEK tube to allow H_2O_2 measurements. Experiments in the presence of metallic iron, magnetite, and chukanovite were carried out in a customized 1 L stainless steel autoclave, capable of withstanding pressures up to 131 bar and temperatures up to 350 °C. The autoclave was equipped with sampling and gas-purging valves, a precision manometer for pressure monitoring, and Swagelok VCR fittings to ensure leak-tightness, which is essential due to H_2 generated under anoxic iron corrosion. Graphite gaskets coated with a thin layer of silicone grease were used to maintain gas-tight sealing and were replaced after each experiment. In all cases, a glass beaker insert was used to prevent contact between the solution and metallic components.

4.3.5. Glove box

Several experiments were carried out in both Ar and N_2 atmosphere glove boxes (Inert Technology). The glovebox internal atmosphere was continuously circulated through a catalytic bed that removes O_2, maintaining oxygen levels below 1 ppm throughout the experiments. The glovebox was maintained at a room temperature of 21.0 ± 2.0 °C.

4.4. Analytical instrument used for both liquid and solid characterization

4.4.1. pH and Redox Potential

Solution pH was measured using a combined pH glass electrode. Calibration was carried out at room temperature with pH 2, 4, 7, and 10 buffer solutions. In the U-Ce coprecipitation study, we have used the $-\log[H^+]$ formula due to the I M $NaClO_4$ medium in which the experiment was conducted. We have also made corrections for the experimentally measured pH using the relation $pH = (pH)exp + \log [H^+] = -0.23 \pm 0.02$ as determined by Fanghänel and coworkers for 1M $NaClO_4$ [179]. In the U-Pu-Np coprecipitation study, we have used the normal pH measurements because the experiment was carried out in a dilute 0.01M NaCl solution. Redox potential was determined

using a calibrated ORP electrode. Measurements were performed immediately after sampling to minimize artefacts.

4.4.2. ICP-OES and ICP-MS

Elemental concentrations were determined using inductively coupled plasma optical emission spectroscopy (ICP-OES, Thermo Scientific, Model iCAP pro) and inductively coupled plasma mass spectrometry (ICP-MS, Thermo Scientific, Model iCAP Q). Fe concentrations during preliminary corrosion experiments were measured by ICP-OES, while actinide (U, Pu, and Np) and Fe concentrations in radioactive samples were determined by ICP. All sample and calibration solutions were prepared by dilution of certified stock solutions (CPAchem) in 0.5 M HNO_3 (Suprapur, Merck). Yttrium (Y) and bismuth (Bi) were added as internal standards for ICP-OES and ICP-MS measurements, respectively.

External calibration series were used in combination with internal standards to ensure analytical accuracy. All samples were analysed in triplicate. Instrument performance assessment test was verified using the Tune B solution, containing U, In, Co, and several additional elements. For ICP-MS measurements, the detection limits were 0.01 ppb for U, 0.001 ppb for Pu and Np, and 0.1 ppb for Fe. During Fe and Ca measurements, kinetic energy discrimination (KED) was applied to minimize polyatomic ion interferences [180]. Measurement uncertainties were generally < 2% (relative uncertainty) for concentrations above 0.1 ppb, reflecting the high sensitivity of the ICP-MS instrument. The uncertainties were not included in the plots because they overlap significantly with the data points.

4.4.3. UV-Vis spectrometry

Ultraviolet–visible (UV–Vis) absorption spectroscopy was used to determine the oxidation states of aqueous actinide species in solution. The absorption spectra were recorded using a UV–Vis spectrophotometer (Shimadzu UV-1800) over a wavelength range of 350–1100 nm. Measurements were performed in quartz cuvettes with a lid and an optical path length of 1 cm. All spectra were collected at room temperature.

4.4.4. Hydrogen peroxide (H_2O_2) analysis

The H_2O_2-concentrations were measured spectrophotometrically at 350 nm wavelength with a Shimadzu UV-Vis spectrophotometer. The analysis was performed using the tri-iodide (Ghormley) method, based on the molybdate-catalyzed oxidation of iodide by H_2O_2 [181]. The instrument was calibrated with a 30 wt.% H_2O_2 standard solution (Sigma-Aldrich). For each measurement, 2 mL of sample was mixed with 100 µL of 1 M KI and 100 µL ammonium molybdate in an acetate buffer (pH 4.65). All reagents were obtained from Sigma-Aldrich, and KI was prepared in Milli-Q water.

4.4.5. Alpha Spectrometry

The specific activity of Pu was measured using an alpha spectrometer (Ortec Alpha Duo, Octete-PC) equipped with PIPS detectors (450 mm^2 active area). Samples were positioned 20 mm from the detector in a chamber operated at 0.05–1 mbar. Before analysis, samples were diluted with 0.5 M HNO_3. The diluted solution was deposited on a planchet, dried under an infrared lamp, and heated with a gas torch to remove residual organic matter. The instrument detection limit was 0.1 Bq mL^{-1}.

4.4.6. Scanning Electron Microscopy (SEM) analysis

Surface morphology and elemental composition of the leached MOX pellets, iron foils, and iron-bearing solids were examined using scanning electron microscopy coupled with energy-dispersive X-ray spectroscopy (SEM–EDX). A Hitachi TM 3000 tabletop SEM–EDX located inside a nitrogen-filled glove box was used for analysis of MOX pellet surfaces to prevent air contamination and radiation exposure. While Iron foils, magnetite, and chukanovite were analyzed using a field-emission SEM (Quanta 200 ESEM FEG). Coprecipitated solid samples were analyzed using a field Emission Gun (FEG) SEM (model ZEISS Aurigas) equipped with both EDX and WDS. The instruments were also equipped with an EDAX Electron Backscatter diffraction detector operated in high-vacuum mode (4.7×10^{-5} mbar) at an accelerating voltage of 15-30 kV and a current of 100 μA. LOD is in the range of 0.1% by weight.

4.4.7. Powder X-ray Diffraction (P-XRD)

P-XRD was used to characterize crystalline phases associated with solid samples (iron foils, magnetite, chukanovite, and U-Ce solid samples). XRD patterns were collected using a Bruker D2 PHASER diffractometer equipped with a monochromatic Cu Kα radiation source (λ = 1.54184 Å). Data were acquired over a 2θ range of 20°–90° at operating conditions of 30 kV and 10 mA. Analyses were performed with the DIFFRAC.EVA software, version 5.2.

4.4.8. Raman Spectroscopy

Confocal Raman spectroscopy was used to identify secondary phases and the nature of corrosion products formed on iron foil and MOX pellet surfaces. A WITec alpha300 R Raman microscope equipped with a cooled EMCCD detector was operated using a 532 nm excitation laser at low power (≤0.6 mW) to avoid beam-induced oxidation or phase transformation. Spectra were collected using a ×100 objective.

4.4.9. Fourier Transform Infrared Spectroscopy (FT-IR)

Fourier Transform Infrared (FT-IR) spectroscopy was used to characterize the functional groups and confirm the formation of chukanovite in the synthesized solid samples. The spectra were recorded using a Bruker Hyperion 3000 microscope coupled with a Bruker Vertex 70v spectrometer PerkinElmer Spectrum, specify model if known) in the range of 4000–400 cm^{-1}. The vertex 70v spectrometer operates under vacuum to reduce atmospheric interference from water vapor and CO_2. Samples were prepared using the attenuated total reflectance (ATR) technique. For ATR measurements, a small amount of finely ground sample was directly placed on the diamond crystal surface. All measurements were performed at room temperature with a spectral resolution of 4 cm^{-1} and averaged over 64 scans per sample to improve the signal-to-noise ratio.

4.4.10. X-ray photoelectron spectroscopy (XPS)

XPS was used to characterize the elemental composition and to investigate the oxidation state of U and Ce in the coprecipitated solid samples after equilibration (paper II), as well as the oxidation state of U deposited on the iron foils (paper I). The instrument was a PHI 5000 VersaProbe III-Scanning XPS microprobe^{TM} with a monochromatic Al K-α X-rays source (1486.6 eV) with a power of 25 W and a voltage of 15 kV. Energy calibration was performed using Ar^+ sputter- Au, Ag, and Cu reference samples, with core-level binding energies of Au $4f_{7/2}$ (83.96 eV), Ag $3d_{5/2}$ (368.21 eV), and Cu $2p_{3/2}$ (932.63eV), and a narrow scan measurement was carried out with the

C1s signal at 284.8 eV before analysis. Survey scans were first acquired to identify elemental composition, followed by high-resolution scans of selected regions, yielding a detection limit of approximately 1 at.%. The solid samples were transported in a transfer vessel tailored to the XPS sample introduction chamber to ensure transportation and sample introduction without risk of air contamination**.**

4.4.11. High-resolution powder X-ray diffraction and X-ray absorption Spectroscopy (XAS)

Powder X-ray diffraction (XRD) and X-ray absorption near-edge structure (XANES) measurements were conducted at the Rossendorf Beamline (BM20) at the European Synchrotron Radiation Facility (ESRF, Grenoble, France). High-resolution XRD data were collected in transmission geometry using monochromatic synchrotron radiation ($\lambda = 7.28 \times 10^{-11}$m). Diffraction patterns were recorded over a 2θ range of 0° - 66° with a step size of 0.01° using an Eiger 2 500k detector, while the incident beam intensity was monitored with a Kapton foil and scintillation counter.

XANES measurements were performed at the XRD-1 station of the Rossendorf Beamline using the same sample setup and beam conditions as for XRD. Spectra were collected in fluorescence mode with a Si drift detector, with incident energy calibrated using the Zr K-edge (18008 eV). Measurements of the Pu L3 edge (~18057 eV) were carried out, and scans were recorded from 18020 to 18170 eV with 1 eV steps, repeated four times. The data were normalized to beam intensity and detector live time, then summed for analysis. The U-Pu-Np coprecipitated solid samples, collected both before and after equilibration, were homogenized with glass powder at a 2:1 mass ratio (sample: glass) to improve particle dispersion and minimize absorption effects. The mixtures were loaded into borosilicate glass capillaries with a diameter of 0.3 mm.

In addition, ~ 1 g of equilibrated $U_{0.98}Pu_{0.01}Np_{0.001}$ and $U_{0.945}Pu_{0.05}Np_{0.005}$ solids were transferred into molybdenum crucibles and subjected to thermal treatment in a furnace under a reducing atmosphere (Ar+5%H_2). The gas flow rate was maintained at 1 L/min throughout the experiment. The samples were heated at a ramp rate of 10 °C/min to 900 °C, maintained for one hour at this temperature, and then cooled down at the same rate. After thermal treatment, the resulting solids were prepared following the same capillary confinement procedure described above and analyzed afterwards.

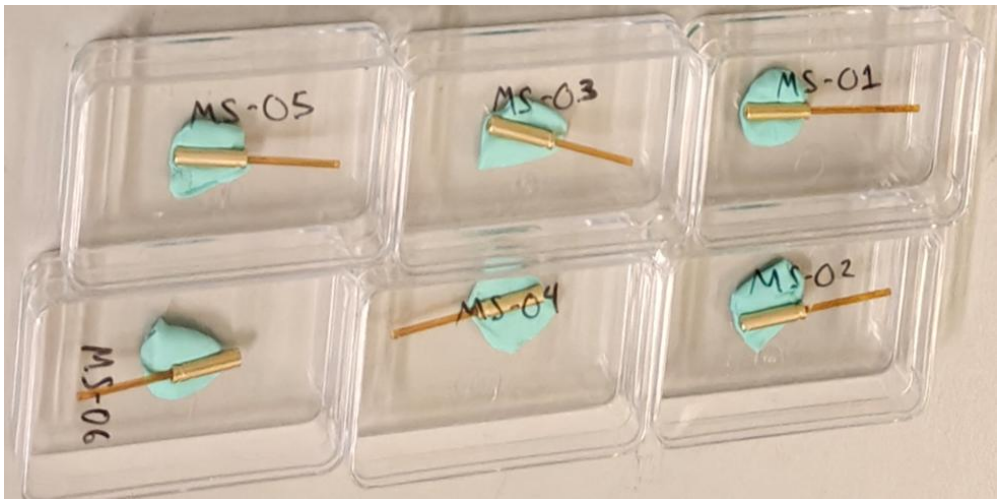

Figure 5: U-Pu-Np solid sample preparation for both P-XRD and XANES analysis.

For radiological safety and to comply with beamline containment requirements, the capillaries were sealed at both ends with epoxy resin and enclosed within a Kapton tube. This assembly was further inserted into a second, larger-diameter Kapton tube to provide double containment. The confined capillary was subsequently fixed with epoxy adhesive (glue) inside a brass pin. Care was taken to ensure that no adhesive contacted the central region of the capillary, thereby avoiding interference with the X-ray beam during data collection. Structural refinements were carried out using the Rietveld method implemented in GSAS-II. Lattice parameters were refined to evaluate solid-solution formation and assess compositional variations within the U, Pu-Np system.

In the earlier U-Ce coprecipitate study, XAS was used to determine the oxidation states and local structure of Ce and U in mixed oxide solid solutions. Measurements were performed in transmission mode at the Ce L3- edge (5723 eV) and U L3-edge (17166 eV). The experiments were conducted at the Balder beamline (MAX IV, Lund, Sweden) using a Si monochromator, with samples prepared as ~20 mg powders mixed with boron nitride and sealed in Kapton-covered holders. Energy calibration was carried out using Cr and Y metal foils, and the collected spectra were processed using standard procedures.

4.5. Experimental procedures/setup

A summary of the experimental procedures is provided here. Additional details regarding the experimental methods and analytical techniques are described in the published article and the submitted manuscript attached to this thesis.

4.5.1. Reductive precipitation of Ca-uranyl carbonato complexes in contact with iron foils (paper I)

The experiments were carried out in an Ar-filled glovebox (Inert Technology). To prepare the reaction, 2mL of a 10 ppm U(VI) stock solution was diluted to 20 mL with synthetic groundwater in plastic vials, which were then placed in a ~2 L glass reaction vessel within the glovebox. The iron foils were contacted in the different groundwater compositions containing the uranyl solution in the vials A-D, as illustrated in the figure below. The vessel was fitted with gas inlets and outlets, enabling continuous flushing with an inert gas to maintain a controlled atmosphere throughout each batch of experiments. Samples were collected approximately every 48 hours and analyzed throughout the experiments, which lasted 750 to 1250 hours (approximately 1-2 months). The schematic of the experimental setup maintained in an inert glove box is shown in Fig.6 below.

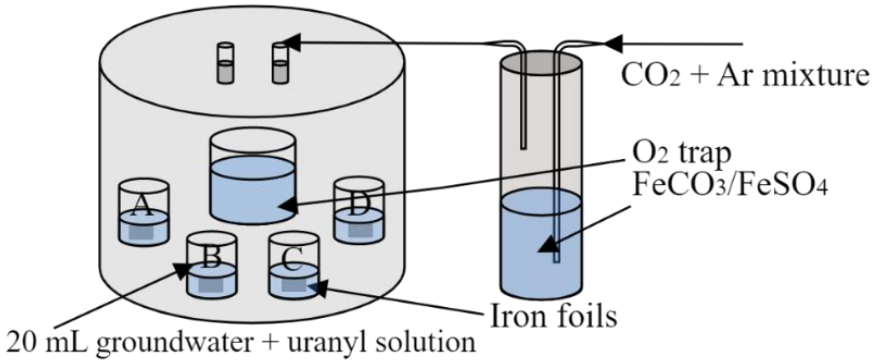

Figure 6. Experimental setup for the iron foils experiments with reaction vessels (A, B, C, D) in the presence of uranyl solution with different groundwater compositions.

4.5.2. Leaching experiments in synthetic Forsmark groundwater in the presence of metallic iron, magnetite, and chukanovite (paper III and V)

Leaching experiments in simplified groundwater solutions and synthesis of Forsmark groundwater were conducted using modified Parr autoclaves equipped with a customized glass beaker insert to prevent contact with metallic components. Unirradiated MOX fuel was contacted with the groundwater in the presence and absence of Fe(s). Solutions were purged with argon before sealing. Periodic liquid sampling was performed via PEEK dip tubes, with initial aliquots discarded to rinse sampling lines. Samples were filtered using a syringe with a 0.45 µm polypropylene membrane filter, and samples were also centrifuged using Amicon centrifuge filters (30000 MWCO) with a pore size of 4 nm to separate potential particulate matter from the solution. At the end of all leaching experiments, the autoclaves were opened under an argon atmosphere. MOX pellets, iron foils, and iron powders were retrieved, dried, and stored under inert conditions before surface characterization. Leaching solutions were filtered, and vessel walls were acid-leached sequentially to quantify sorbed or precipitated U. Iron powders and foils were dissolved in HNO_3 to quantify the amount of U, Pu sorbed. In the subsequent study, the dissolution of the same MOX fuel pellet was investigated in the presence of magnetite and also in the presence of chukanovite.

Figure 7: Autoclave used for the leaching experiments.

4.5.3. Co-precipitation experiments (paper II and IV)

Co-precipitation experiments were conducted in argon-filled glove boxes at ambient temperature. In the first study, acidic stock solutions containing U(IV) and Ce(III) were mixed in defined molar ratios (see attached publication to this thesis for the detailed experimental procedure). In the subsequent study, stock solutions of U(IV), Pu(IV), and Np(IV) were mixed in a ratio similar to

their composition in SNF. The mixed stock solutions of U, Pu, and Np were allowed to homogenize for a few minutes, after which 20 mM sodium dithionite ($Na_2S_2O_4$) was added to the stock solutions to maintain reducing conditions. These steps are necessary to ensure that the reduction of Pu(IV) to Pu(III) occurs either by U(IV) or by added dithionite, thereby preventing any traces of oxidized Pu or Np. Precipitation of the mixed solutions was induced by stepwise addition of carbonate-free NaOH (until pH 9.5-10 was obtained in the neutralized solution) to precipitate U, Pu, and Np as amorphous hydroxides and prevent decomposition of dithionite. The resulting solid precipitates were separated by using a vacuum filtration setup in the glove box.

After filtration, the solid residue on the filter paper was collected and transferred to a separate beaker in the glove box. The resulting solid residue was washed twice with 20mM $Na_2S_2O_4$ solution to remove NaCl formed during neutralization and was aged overnight in the glove box before solubility experiments. Portions of the aged precipitates were further washed with 10 mM $Na_2S_2O_4$ and filtered using the vacuum filtration setup as before. At a final step, the filtered solid precipitates were distributed in a 40 mL centrifuge tube for the solubility test between pH 2 and 12. Solutions containing 10mM NaCl and 1mM $Na_2S_2O_4$ were used as the ionic medium for solubility measurement. Two sets of experiments were conducted with these precipitates. One set of experiments was conducted with 1% molar concentration of Pu, 0.1% Np, and the other with 5% Pu, 0.5% Np concentration in the solid.

The remaining precipitated solids were subjected to further washing with $Na_2S_2O_4$ and ultrapure water, after which the solids were left to dry in a desiccator before characterization. In the U-Ce coprecipitate study, a similar experimental approach was used except for the ionic medium, which was 1 M $NaClO_4$.

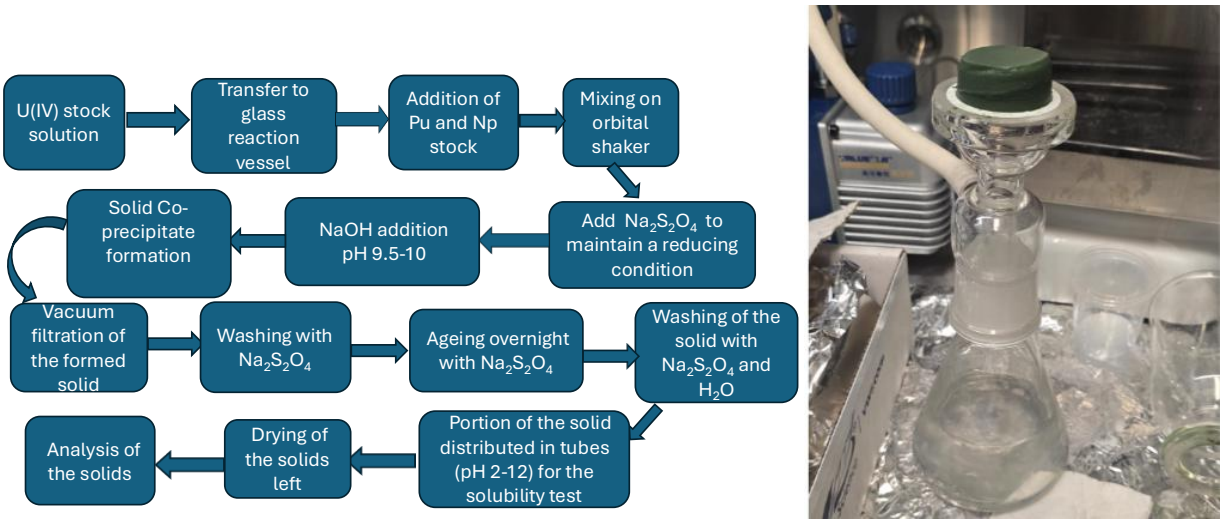

Figure 8:(a) Experimental procedure used for the U-Pu- Np coprecipitation experiment and (b) resulting solid coprecipitates of U-Pu-Np after neutralization.

5.0. Results and discussion

5.1. Influence of groundwater composition on the reductive precipitation of U(VI) in the presence of corroded iron surfaces (paper I)

To aid the interpretation of the results presented in the following sections, Table 3 provides groundwater compositions, atmospheric conditions, and their associated experimental labels.

Table 3. Groundwater and Atmosphere compositions and their corresponding sample label.

Groundwater	Label
01D	A, E, I, M
02A	B, F, J, N
10-2	C, G, K,O
10-2-Ca	D, H, L, P
Atmosphere	**Label**
3000 ppm CO_2 in Ar	A, B, C, D
400 ppm CO_2 in Ar	E, F, G, H, I, J, K, L, M, N, O, P

5.1.1. Determination of measured U, Fe, and Ca concentrations in solution by ICP-MS

The measured dissolved U, Fe, and Ca concentrations for the experiment series A-D conducted under an argon atmosphere containing 3000 ppm CO_2 are shown in Fig.9. The initial U concentrations of 1 ppm (4.2 x10^{-6} M) decrease progressively to ~10^{-9} M toward the end of the 1200 hours (50 days) of experiment across all datasets. Higher Fe concentrations were observed at early reaction times in experiments A and B, which is attributable to the higher Fe content of the 01D and 02A groundwater compositions. After ~ 200 hours, dissolved Fe concentrations are nearly equal across all four series (A-D). Afterward, Fe concentrations stabilize and reach an equilibrium of ~ 10^{-3} M in experiments A and B, whereas experiments C and D exhibit values nearly two orders of magnitude lower (~10^{-5} M). Ca concentration remained constant throughout the experimental period, which is consistent with its initial concentration.

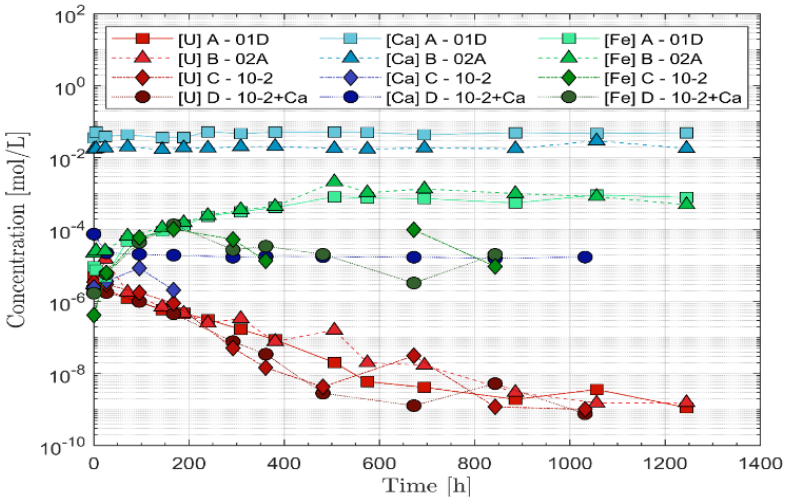

Figure 9. Dissolved concentrations measured in experimental series A–D conducted under 3000 ppm CO_2 in an Ar atmosphere using $FeSO_4$ as an oxygen trap.

For the experimental series I-L conducted under 400 ppm CO_2, the dissolved concentrations of U, Fe, and Ca are shown in Fig.10. U concentrations in this series also decrease to lower values, ~10^{-9} – 10^{-8} M, but not as low as those observed in experiments A-D series (~10^{-9} M, Fig. 9). However, the duration of experiment I-L was shorter (770 hours) when compared to A-D, which can explain the difference observed. Throughout the experimental duration, Ca concentration remained constant, reflecting its stability under the experimental conditions.

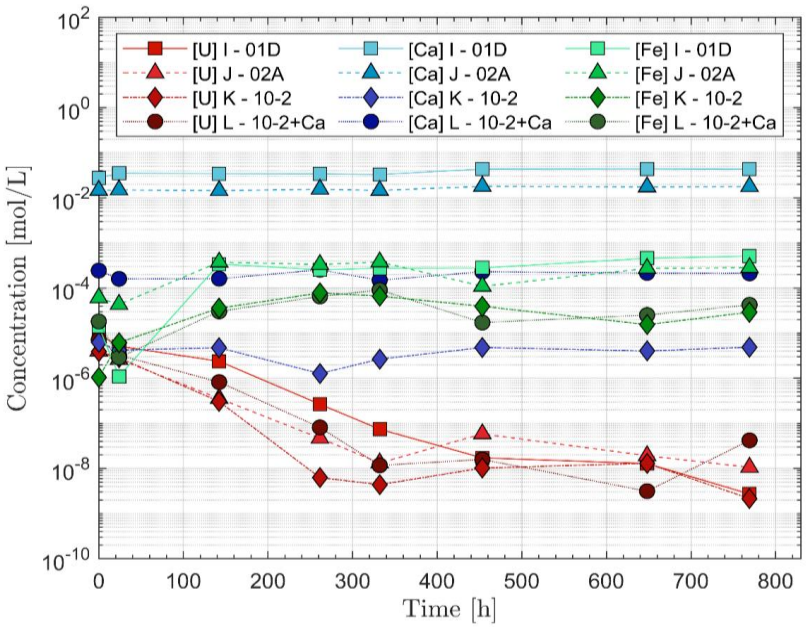

Figure 10. Dissolved concentrations measured in experimental series I-L, conducted under 400 ppm CO_2 in an Ar atmosphere using $FeSO_4$ as an oxygen trap.

The observed rapid decrease in aqueous U concentrations indicates that U(VI) is effectively reduced and precipitated in the synthetic groundwater systems containing corroding iron foil. The higher Fe concentration observed in batch I-L is likely due to the greater efficiency of the $FeSO_4$ oxygen trap as compared to batch E-H, where $FeCO_3$ was used as an O_2 trap. The experimental results for batches E-H and M-P are presented in the published article attached to this thesis.

5.2. Solid characterizations

5.2.1. SEM-EDX results

At the end of the leaching experiments, the iron foils were retrieved from the synthetic groundwater solution. Visual inspections revealed the presence of dark-green surface spots (see Figs. 11a and 11b), which are characteristic features of green rust formation [156, 182, 183]. SEM analysis was performed on iron foils from selected experimental batches due to potential O_2 contamination during storage after the leaching experiments. SEM micrographs of iron foils from experiments E, F, K, and H, representing exposure to different simulated groundwater compositions, are presented in Figs. 12 and 13.

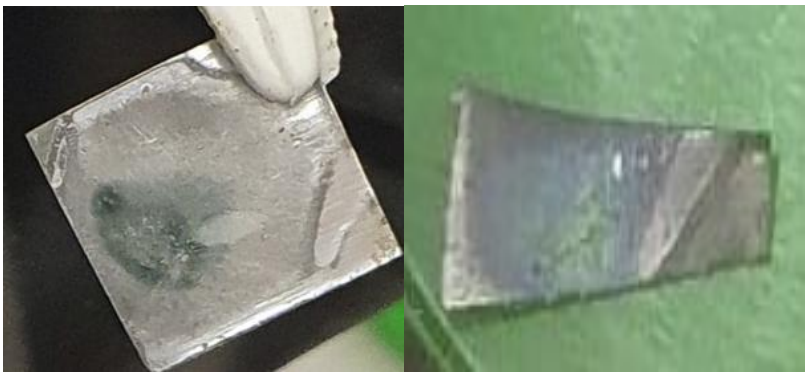

Figure 11. Representative images of iron foil obtained from experiments E and F, respectively, where clear green (a) and green-blue (b) rust surface features or spots are found.

The distribution of U on the iron foil surfaces was heterogeneous, with U occurring as localized agglomerates in a few grains, appearing as spots. In experiments E and F, U was present as small, discrete, grain-like features, whereas substantially larger U-rich particles were observed on iron foil from experiment K. The U distribution on foils from experiment H closely resembled that observed for experiments E and F.

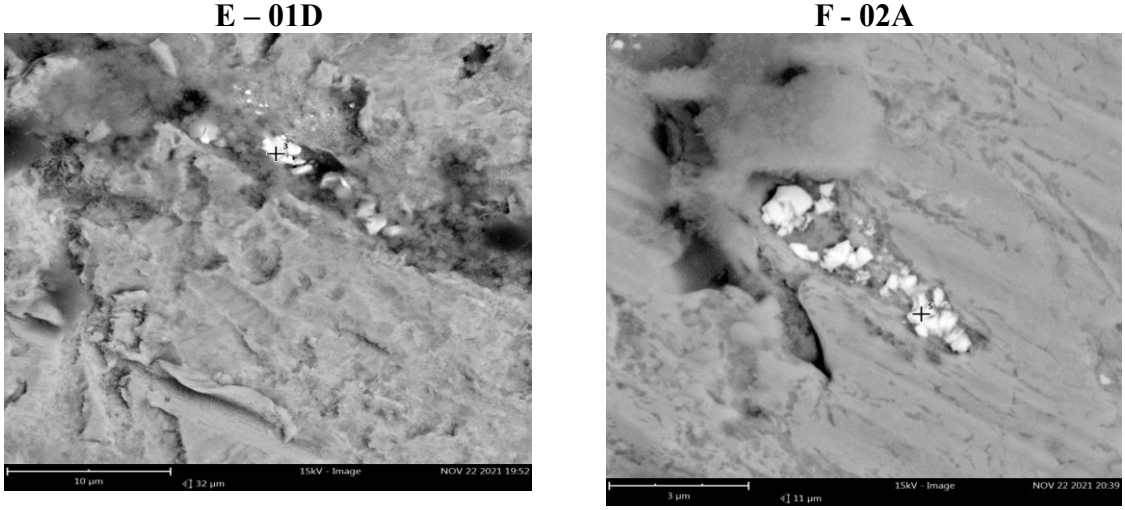

Figure 12. SEM micrographs of iron foils from experiments **E** (a) and **F** (b), showing U-rich precipitates on the corroded iron surfaces.

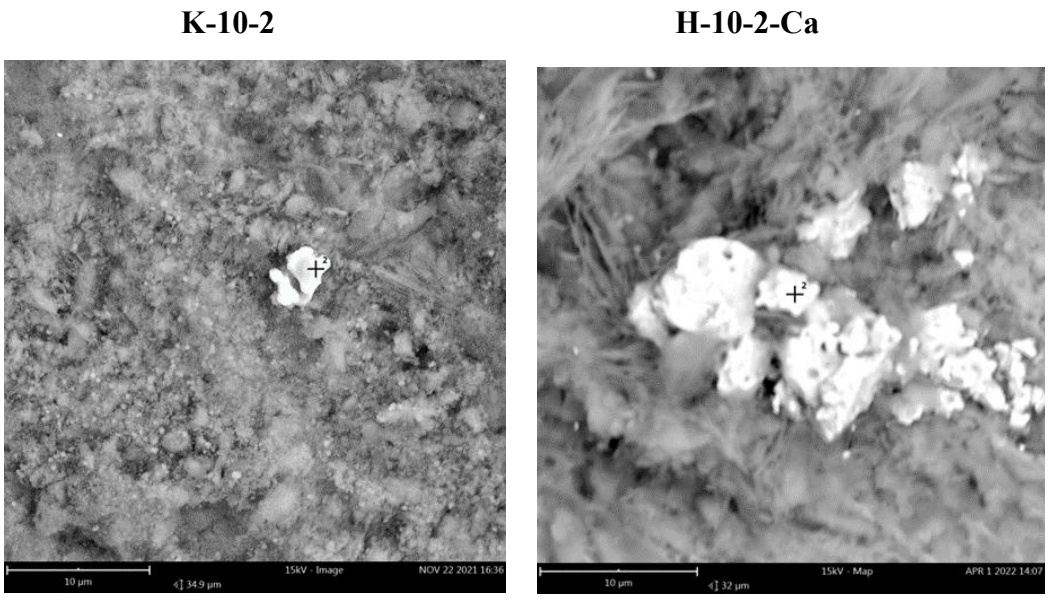

Figure 13. SEM micrographs of iron foils from experiments K (a) and H (b) showing the large, precipitated U-containing grains

EDX analysis shows that the iron foils exposed to the 01D and 02A groundwater compositions exhibited chemically complex surface layers containing Fe, O, Na, Cl, C, and Si. The U-rich precipitates formed on the foil surfaces consist primarily of Fe, U, C, and O, as summarized in Table 4. The carbonate-rich 02A groundwater resulted in a higher carbon content in the U grains on iron foil F (8-16 at.%), compared with foil E exposed to 01D groundwater (1-5 at.%), based on the analysis of five grains per foil. Inclusion of oxygen in the quantitative analysis reduced the relative atomic fractions of the remaining elements.

Table 4. EDX element compositions on iron foils labelled E, F, G, H, K, and L

Element	E (at.%)	F (at.%)	G (at.%)	H (at.%)	K (at.%)	L (at.%)
O	57.15	-	-	63.06	47.58	60.72
Fe	24.61	54.22	24.26	12.42	10.61	13.40
U	15.12	34.33	60.78	19.50	32.71	19.90
C	3.13	11.45	14.96	5.02	9.09	5.98

An elemental mapping of grains deposited on the iron foil surface from experiments F, G, and H revealed that U precipitates had a considerable overlap with carbon. Regions with higher C content were closely associated with the U precipitates (see Fig. 14)

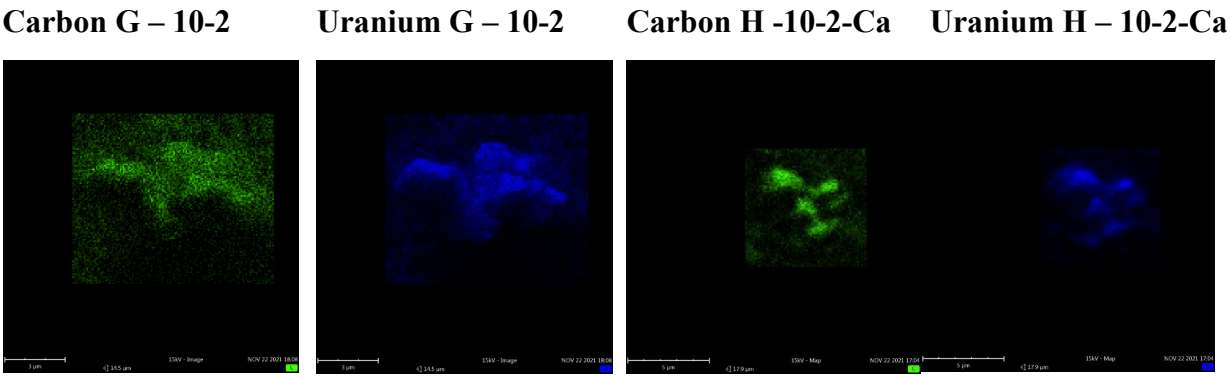

Figure 14. The elemental mapping scans reveal significant overlap between C and U on the iron foil surfaces.

The observed SEM-EDX elemental mapping results indicate that U precipitated on carbonate-rich regions of the iron foil surface, likely associated with carbonate-containing green rust corrosion products. This observation is consistent with previous studies, where U precipitation has been observed on top of green rust [156]. Also, the findings from this study are in agreement with the work of O´Loughlin, which shows that green rust can facilitate the reductive formation of UO_2 nanoparticles [184].

5.2.2. XPS Surface analysis results

XPS measurements were carried out on the iron foils containing U precipitates to evaluate the surface characteristics following exposure to the uranyl-containing synthetic groundwaters. The analysis focuses on the core levels of $U4f_{7/2}$, $U4f_{5/2,}$ and $Fe2p_{3/2}$. Due to the relatively low U concentrations in these experiments, the XPS spectra exhibited weak signal intensity and noticeable background noise. The $U4f_{7/2}$ and $U4f_{5/2}$ spectra from experiments E-H are presented in Fig.15, with all peaks showing a full width at half maximum (FWHM) close to 1.8 eV, corresponding to a single oxidation state [185, 186]. The observed U peak position corresponds to U in a lower oxidation state.

The $U4f_{7/2}$ peaks observed in experiments E–H exhibit binding energies consistent with U(IV), centered around 380.0 ± 0.2 eV, indicating that U associated with the iron foils is in the reduced tetravalent state. The corresponding satellite shifts are generally consistent with those expected for U(IV), with an energy separation of ~ 6.9 ± 0.5 eV. Although some satellite shifts appear slightly lower than the typical range, this does not indicate the presence of U(V), as U(V) species would be characterized by satellites at higher binding energies.

The $Fe2p_{3/2}$ peaks of the iron foils were also analyzed and deconvoluted into contributions from t Fe(0), $Fe(II)_{oct}$, $Fe(III)_{oct}$, $Fe(III)_{tet}$, $Fe(II)_{sat}$ and $Fe(III)_{sat}$ for experiment batches E-H and I-L. The corresponding Fe(III)/Fe(II) ratios derived from the $Fe2p_{3/2}$ peaks range from 0.98-1.27 for batches E-H and from 0.96-1.54 for batches I-L. Detailed peak deconvolution and Fe(III)/Fe(II) ratios for the iron foils from the different experimental batches are reported in the published article associated with this thesis.

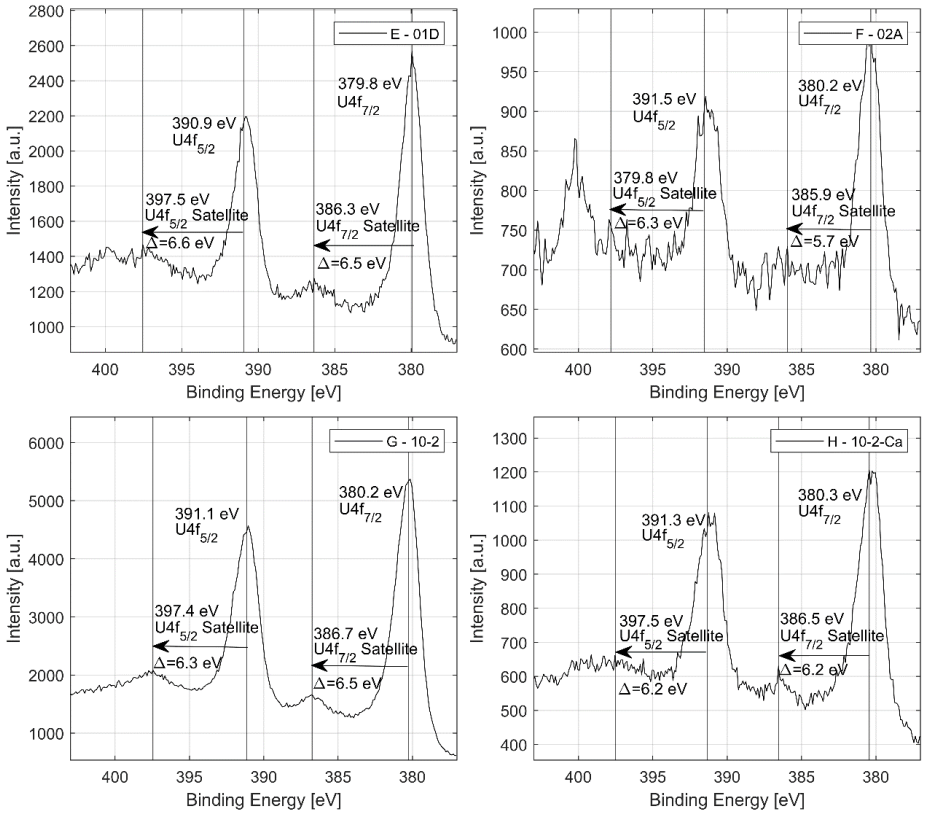

Figure 15. XPS analysis of the $U4f_{7/2}$ and $U4f_{5/2}$ peaks along with their corresponding satellite features, for experiment series E-H.

5.3. Uranyl speciation calculations and kinetics of U(VI) reduction

The speciation of uranyl in synthetic groundwaters under 400 ppm and 3000 ppm CO_2 in Ar atmospheres was modelled using PHREEQC [187], using the Lawrence Livermore database, with the addition of Ca- uranyl complexes from the NEA TDB database [16] and including the redox - active element Rx and Inert elements Ip and Im [188]. In all Ca-containing groundwaters under a CO_2 partial pressure of 400 ppm and 3000 ppm, the $Ca_2UO_2(CO_3)_3$ complex is the predominant species. As presented in Table 5, Ca-uranyl-carbonato complexes constitute approximately 90 % of the dissolved U in groundwater 01D at 400 ppm CO_2, decreasing to 56.5 % at 3000 ppm CO_2. In synthetic groundwater 02A, these complexes dominate uranyl speciation to an even greater extent, accounting for nearly 99.7 % of total U under both 400 ppm and 3000 ppm CO_2 conditions.

The removal of U(VI) by corroding metallic iron followed pseudo-first-order kinetics, as indicated by a linear relationship between $\ln(C_t/C_0)$ versus reaction time. The reaction rates were determined from the initial stages of the experiments (5-6 data points) using linear regression. Notably, experiments A and B, which contained higher Fe concentrations, did not enhance the reduction kinetics, suggesting that the increased Fe concentrations did not influence kinetics but rather affected the final equilibrium conditions. Similarly, elevated CO_2 pressure increased Fe dissolution at equilibrium but had no significant effect on the early-stage reaction kinetics.

Table 5. Modelled major uranyl species using PHREEQE C in the 400 ppm and 3000 ppm CO_2 atmosphere experiments.

400 ppm CO_2	**01D**	**02A**	**10-2**	**10-2-Ca**
$Ca_2UO_2(CO_3)_3$	87.60%	95.39%	0.00%	48.08%
$CaUO_2(CO_3)_3^{2-}$	1.88%	4.28%	0.00%	43.43%
$UO_2(OH)_2$	5.75%	0.00%	3.56%	0.31%
$UO_2(CO_3)_2^{2-}$	2.17%	0.01%	68.09%	5.88%
UO_2CO_3	2.09%	-	1.09%	0.09%
$UO_2(CO_3)_3^{4-}$	-	0.31%	24.51%	2.21%

3000 ppm CO_2	**01D**	**02A**	**10-2**	**10-2-Ca**
$Ca_2UO_2(CO_3)_3$	55.34%	95.39%	-	32.06%
$CaUO_2(CO_3)_3^{2}$	1.19%	4.27%	-	28.75%
UO_2CO_3	17.06%	-	9.85%	3.90%
$UO_2(OH)_2$	7.18%	0.00%	4.09%	1.64%
$UO_2(CO_3)_2^{2-}$	4.94%	0.02%	78.83%	31.56%
$(UO_2)_2CO_3(OH)_3^{-}$	1.75%	-	3.43%	0.56%

The presence of Ca-uranyl-carbonato complexes was found to slightly decrease the reduction rate of U(VI) compared to Ca-free groundwater systems. Under high CO_2 conditions (3000 ppm), the reduction rate in Ca-free solutions was approximately 1.8 times higher than in Ca-containing groundwater, where Ca-uranyl-carbonato complexes dominate the aqueous speciation. However, these differences remain relatively small.

Overall, the results indicate that oxygen scavenging efficiency plays a more significant role in controlling the reduction kinetics than Ca complexation. Under lower CO_2 conditions (400 ppm), the highest reduction rates were observed, both in the presence and absence of Ca. Nevertheless, the presence of Ca consistently led to a modest decrease in reduction rates, typically by a factor of 1.2–1.6.

5.4. Leaching of unirradiated MOX fuel in the presence of metallic iron and its corrosion products (paper III and V)

5.4.1 Forsmark groundwater chemistry (pH and Eh for all leaching experiments)

In the leaching study of the MOX fuel pellet (10% Pu) in synthetic Forsmark groundwater in the presence of metallic iron, the solution pH was monitored prior to and following the addition of the MOX fuel pellet. Throughout the leaching experiment, the pH remained stable within the range of 6.9 (± 0.1) to 7.2 (± 0.1), with no significant pH change observed. Redox potential (Eh) measurements were performed on aliquots collected near the conclusion of the MOX dissolution experiment, yielding values between −30 and −40 mV /SHE. For the concentrations of the

groundwater composition, only slight decreases in the concentrations were observed (mainly Ca), which can be attributed to the relatively high solution-to-solid ratio used in the experiment.
In the leaching test in the presence of magnetite, the pH showed similar behaviour, decreasing slightly from 7.2 (± 0.1) to 7.1 (± 0.1) throughout the duration of the leaching experiment. E_h measurements conducted at the beginning and towards the end of the experiments ranged between -178 and -162 mV/SHE (first two sampling points), and in subsequent measurements (final five sampling points), Eh increased to values between −30 and −22 mV/SHE. While in the leaching test in the presence of chukanovite, Eh ranged from -102 and −106 mV/SHE (first three sampling points), towards the end of the experiments, it read - 116mV/SHE.

The pH of the solution varied between 7.2 (±0.1) and 7.6 (±0.1), showing a gradual increase throughout the leaching experiment. This rise in pH can be attributed to the release of carbonate species from chukanovite, which likely resulted in higher pH values compared to those observed in similar leaching systems containing magnetite. In general, fluctuations in Eh were observed across all measurements in the presence of metallic iron, magnetite, and chukanovite, but they all correspond to reducing conditions.

5.4.2. Evolution of U and Pu concentrations in simulated groundwater solutions in the presence and absence of metallic iron (paper III)

The measured dissolved concentrations of both U and Pu in the leaching tests carried out in the presence and absence of metallic iron are shown in Fig.16. Both U and Pu serve as indicators of the oxidative dissolution of the MOX fuel pellet. Leaching test carried out under simulated Forsmark groundwater in the presence of metallic iron shows that uranium concentrations decreased gradually from 0.7 µg/L (2.9×10^{-9} M) at the start of the experiment to 0.3 µg /L (1.3×10^{-9} M) after 240 days of the leaching experiment. This concentration remains stable until the end of the leaching experiment (407 days) , which implies that a steady-state concentration was reached. The measured Pu concentrations were below the detection limits of the ICP-MS instrument except for a few initial data points, which correspond to very low Pu concentration data (see Fig. 16). Also, the measured activities of Pu were below the detection limits of the alpha spectrophotometer (0.1 Bq/mL)

In contrast, in the leaching test carried out under carbonated solution (10 mM NaCl, 2 mM $NaHCO_3$) in the absence of metallic iron, the U concentrations steadily increased throughout the experiment, indicating continuous oxidative dissolution of the MOX pellet. The concentration of Pu could only be measured for the first two sampling points, which is approximately 2 x 10^{-8}M, and decreased later below the detection limit of the instrument.H_2O_2, a key oxidative species, was measured using the Ghormley method, and the measured concentration was above the detection limit 2×10^{-6} M after ~164 days and reached a steady state concentration of ~2.6×10^{-5} M after 297 days. The release rate of U was minimal during the first 20 days of the leaching test, and between 30-40 days, the release rate reached a steady value of about 2.4 X 10-7 mol.d^{-1}. The significant production of H_2O_2 induced by the strong α-radiation from the MOX pellet promotes the oxidation of U(IV) to U(VI), which is then released in solution as uranyl carbonate complexes.

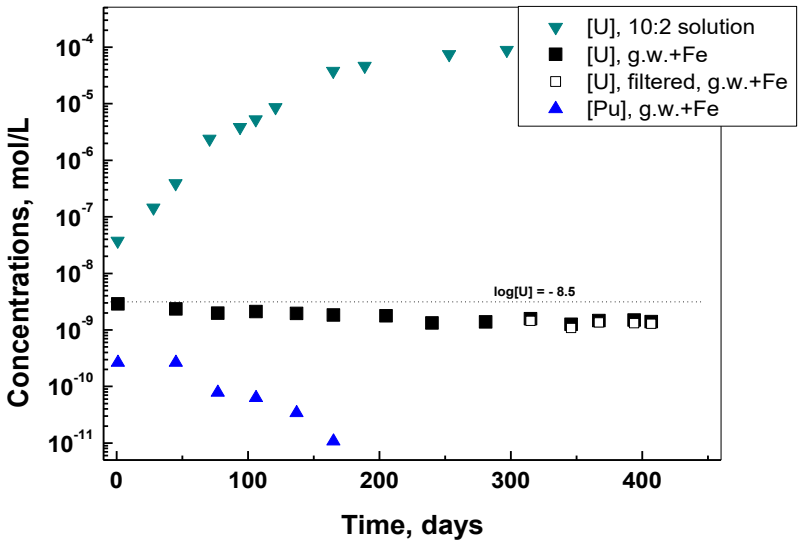

Figure 16. Evolution of U and Pu concentrations in solutions during leaching of the 10% Pu MOX pellet under Ar in 10-2 solution (10 mM NaCl, 2 mM $NaHCO_3$) and in Forsmark groundwater in the presence of Fe(s).

The low initial U concentration (leaching test in the presence of iron) indicates that the pre-oxidized surface layer of the MOX pellet was effectively minimized, preventing a higher measured concentration of U. The persistently low and slightly decreasing U concentrations throughout the experiment demonstrate the strong influence of groundwater chemistry and metallic iron in maintaining reducing conditions. The similar U concentrations measured in filtered and ultrafiltered samples collected after 315 days suggest that colloid formation was unlikely. The measured U concentrations were consistent with the lower solubility limit of amorphous UO_2 [16], indicating that U remained predominantly in the reduced oxidation state U(IV).
Dissolved Fe(II) and H_2 generated in the system acted as reducing agents, thereby suppressing or inhibiting the oxidative dissolution of the MOX fuel pellet despite potential alpha-radiolytic production of oxidants such as H_2O_2.
Pu concentrations were below the detection limit of alpha spectrometry and remained very low by ICP-MS, although slightly higher than the reported solubility of amorphous PuO_2 [16]. These concentrations are comparable to previously reported values for reductive dissolution of PuO_2 in the presence of Fe(II) [189]. Thermodynamically, Fe(II) can reduce Pu(IV) to Pu(III), and the formation of $Fe(OH)_3$(s) through radiolytic oxidation of Fe(II) likely provided sorption sites for Pu, contributing to the observed decrease in dissolved Pu concentrations over time.

5.4.3. Evolution of Fe and H_2 in the leaching test in the presence of metallic iron

Fe(II) concentrations in solution were monitored over time initially by ICP-OES and ICP-MS after introducing the MOX pellet (Fig. 17). Initially, Fe(II) increased almost linearly, reflecting the anoxic corrosion of metallic iron in the synthetic groundwater, which produces Fe(II) and H_2. After 101 days, the autoclave was opened in an Ar- filled glove bag. The introduction of the MOX pellet caused a slight decrease in Fe(II) due to minor O_2 ingress during handling. Afterwards, the Fe(II) starts to increase almost linearly again. After approximately 200 days, the dissolved Fe

concentration stabilizes and reaches a plateau at around 50 mg/L. This stabilization suggests the precipitation of a secondary iron phase with relatively high solubility. High Fe(II) concentrations have been shown in previous comparable studies to inhibit the oxidative dissolution of fuel [92,135]. During the initial 101 days (pre-corrosion phase), H_2 production increased gradually, with an average rate of 7.2×10^{-5} mol H_2.day^{-1}. Following the introduction of the MOX fuel pellet, H_2 generation continued over the 508-day leaching period. The average production rate increased slightly to 8.6×10^{-5} mol H_2.day^{-1}. This rate is consistent with previously reported values for similar systems involving spent fuel and iron powder [18].

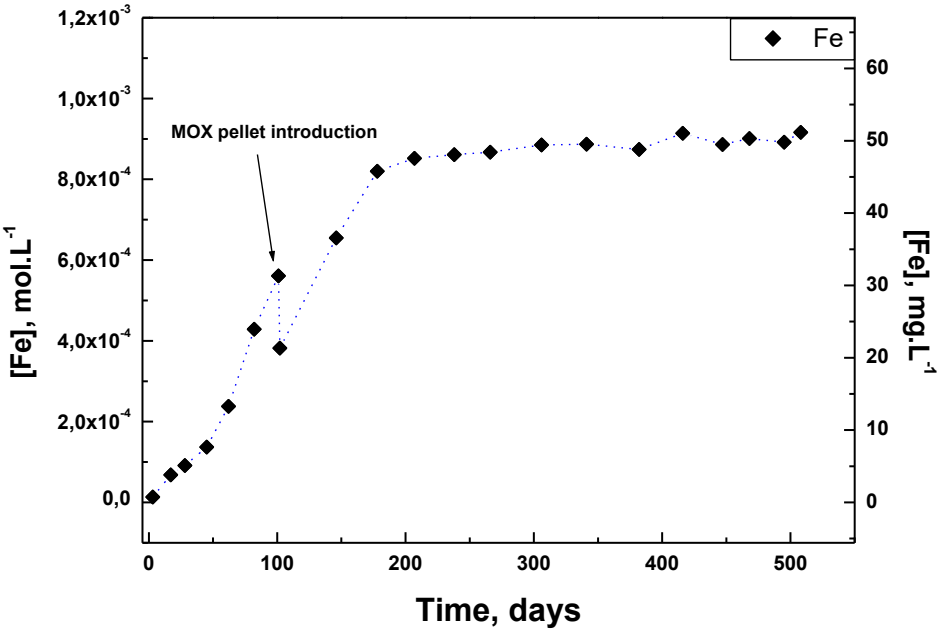

Figure 17: Evolution of dissolved Fe concentration in solution during leaching of the MOX pellet in Forsmark synthetic groundwater.

The results of the leaching test in the presence of metallic iron demonstrate that the presence of Fe(II) and H_2 produced during the anoxic corrosion of the metallic iron strongly suppresses MOX pellet dissolution by maintaining reducing conditions, which inhibit both U and Pu release. In the absence of metallic iron, oxidative species such as H_2O_2 build up, driving continuous U dissolution in the carbonated solution. This highlights the critical role of iron corrosion in controlling U(VI) mobility under near-neutral groundwater conditions.

5.4.4. Analysis of the distribution of U in aqueous solution and sorbed/precipitated on solid surfaces

At the end of the leaching experiment in the presence of metallic iron, the distribution of U among different system components was assessed (Fig.18). Only 1.2 % of the released U (0.14 µg) remained in solution, while 4.9 % (0.58 µg) was associated with the iron foils and 10.4 % (1.24 µg) sorbed or precipitated on the quartz beaker insert. The majority, 83.5 % (9.91 µg), was retained on

the iron powder, which had the largest surface area in contact with the solution. Overall, 11.9 µg of U was mobilized over more than one year. These results show that U(IV) was mainly sorbed on the different surfaces.

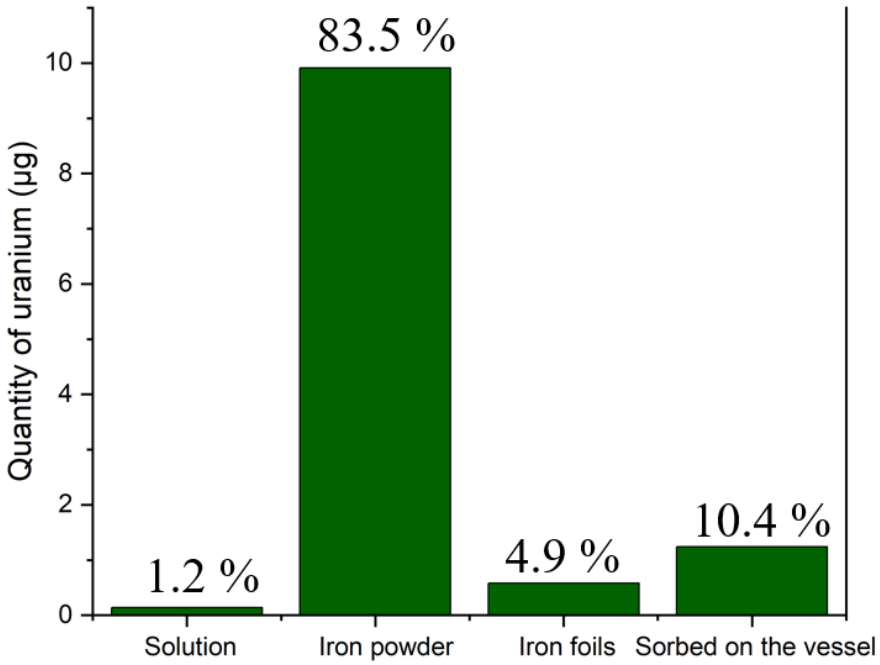

Figure 18: Uranium quantification among different system components.

5.5. Solid characterization of the leached MOX pellet in the presence of metallic iron

5.5.1. SEM analysis of the leached MOX pellet in the presence of metallic iron

At the conclusion of the leaching experiment, the MOX pellet was removed from the leaching solution, and the surface of the leached MOX fuel pellet was entirely covered with a red, granular-shaped precipitate several micrometers thick (see Fig. 19).

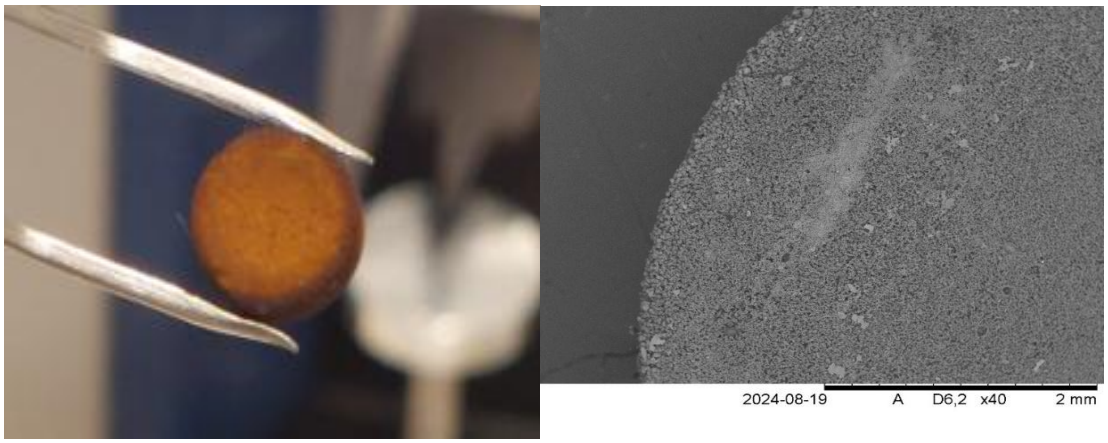

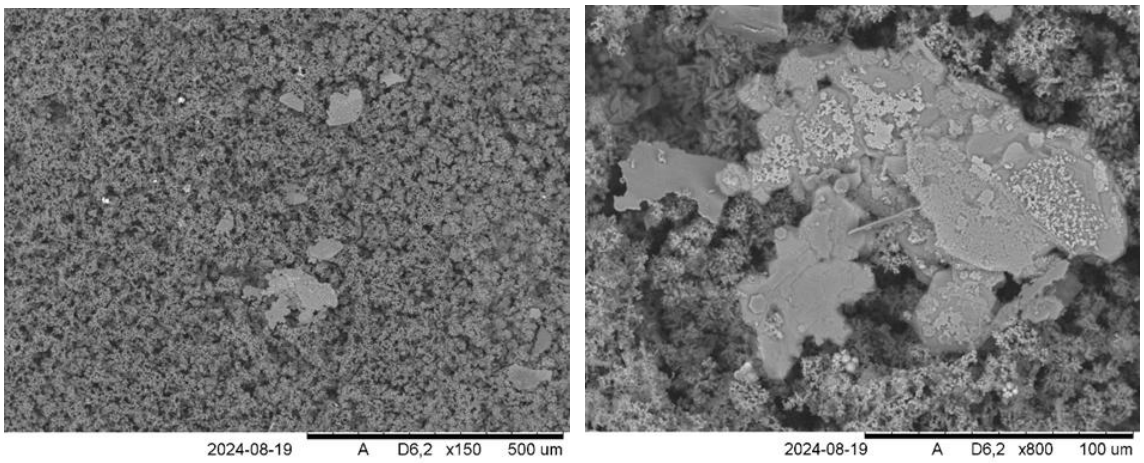

Figure 19. SEM micrographs of the leached MOX pellet in synthetic Forsmark groundwater in the presence of iron, with the top left image showing the pellet when it was removed from the leaching solution.

The EDX analyses and elemental mapping of the precipitates formed on the surface of the MOX pellet were carried out by gently pressing Kapton tape onto the surface of the pellet and subsequently analyzing the powder attached to the tape. The corresponding EDX spectrum and elemental distribution maps are presented in Fig. 20. The EDX results (from the average of EDX analyses performed on 8-10 different spots on each micrograph analyzed) identify Fe and O as the dominant elements in the formed phases. Minor amounts of Si, C, Ca, Na, S, Cl, and Mn were also detected, which most likely originate from residual salts following evaporation of the synthetic groundwater. No U signal was detected in any of the acquired spectra.

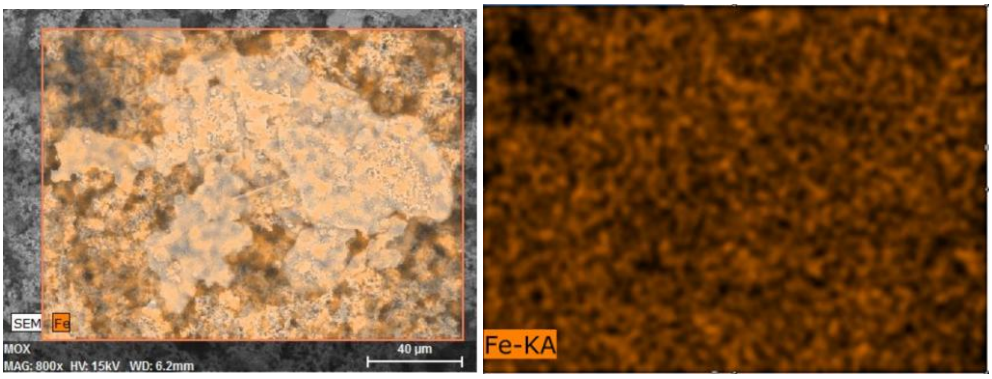

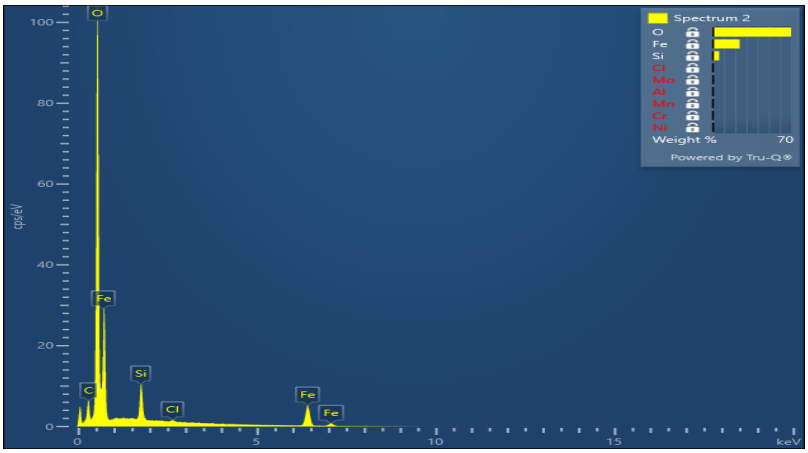

Figure 20. Elemental mapping and SEM-EDX analyses of the precipitates formed on the leached MOX pellet surface.

The SEM-EDX results indicate that the precipitates are primarily composed of Fe-containing compounds, formed at the fuel- water interface as a result of Fe(II) oxidation to Fe(III). Earlier studies on alpha-doped UO_2 pellet have similarly reported the formation of iron hydroxide phases such as akageneite (β-FeOOH) on the surface of leached MOX pellet in the presence of iron [92,135].

5.5.2. Powder XRD analysis of the red deposit on the MOX pellet surface

X-ray diffraction (XRD) analysis of the red precipitate from the corroded MOX pellet was conducted to determine its structural phase. The diffractogram exhibited broad and not well-defined peaks, as shown in Fig. 21, indicating that the precipitate is mainly amorphous. Although the presence of minor micro-crystallinity cannot be ruled out, no well-defined crystalline phases could be conclusively identified. Comparison of the diffraction pattern with entries in the ICDD database matches some peaks with several Fe(III) oxide phases, including lepidocrocite, goethite, akaganeite, hematite, and maghemite. However, due to the lack of distinct diffraction peaks, definitive phase identification was not possible, supporting the conclusion that the precipitate mainly consists of poorly crystalline or amorphous Fe(III) oxide phases.

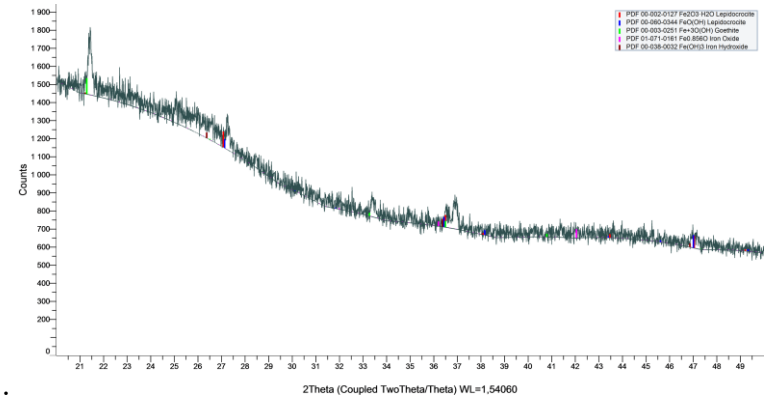

Figure 21. XRD patterns of the red deposit or precipitates formed on the surface of the leached MOX pellet. The sharper peaks originate from the Kapton tape and sample holder.

5.5.3. Raman spectroscopy analysis of the precipitates on the surface of the MOX pellet in the presence of metallic iron

Raman spectroscopy was performed on the precipitate formed on the MOX pellet surface to determine the nature of the precipitates formed. The spectra, obtained from six different spots (Fig. 22), closely match the reference spectrum of akageneite (β-FeOOH), with characteristic peaks at 303, 392, 714, and 1392 cm^{-1}, consistent with previous studies [92, 135, 190]. Additional features indicate similarity to lepidocrocite [191]. Overall, the results suggest that the precipitates are composed of various Fe(III) oxides, including akageneite, lepidocrocite, and goethite, formed through oxidation of Fe(II) to Fe(III) by H_2O_2 and other radiolytic oxidants.

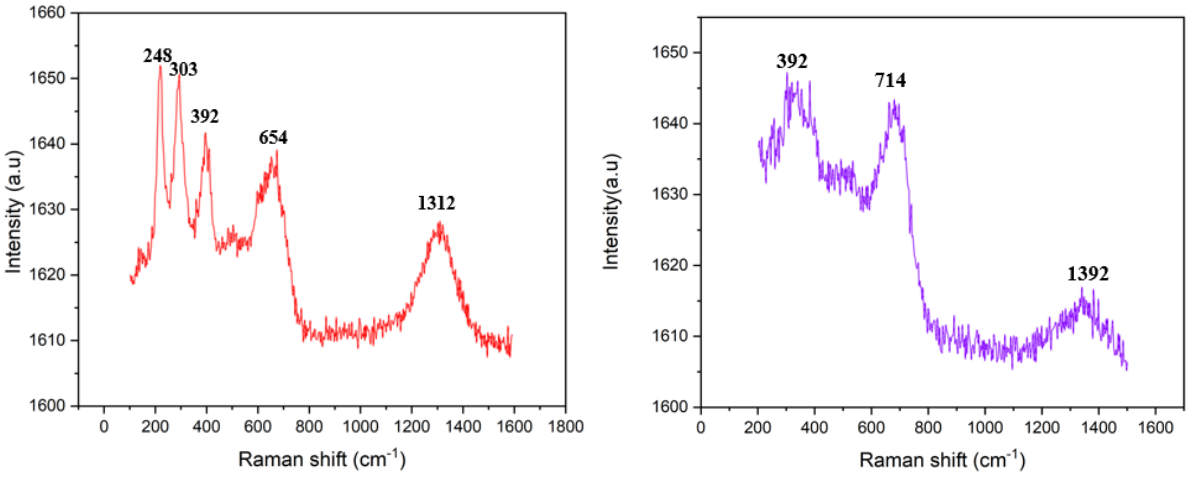

Figure 22. Raman spectra of the precipitates found on the leached MOX pellet.

5.5.4. SEM-EDX analyses on the corroded iron foils

The microstructure and elemental composition of the iron foils were also examined using SEM-EDX following completion of the autoclave leaching experiment. Representative micrographs of the corroded iron foil surfaces, acquired from different regions and at varying magnifications, are presented in Fig. 23. The micrographs indicate that the iron foils corroded, resulting in the formation of multiple distinct phases. Additionally, the deposition of precipitate particles ranging from nm to µm scale was observed on the corroded iron foil surfaces.

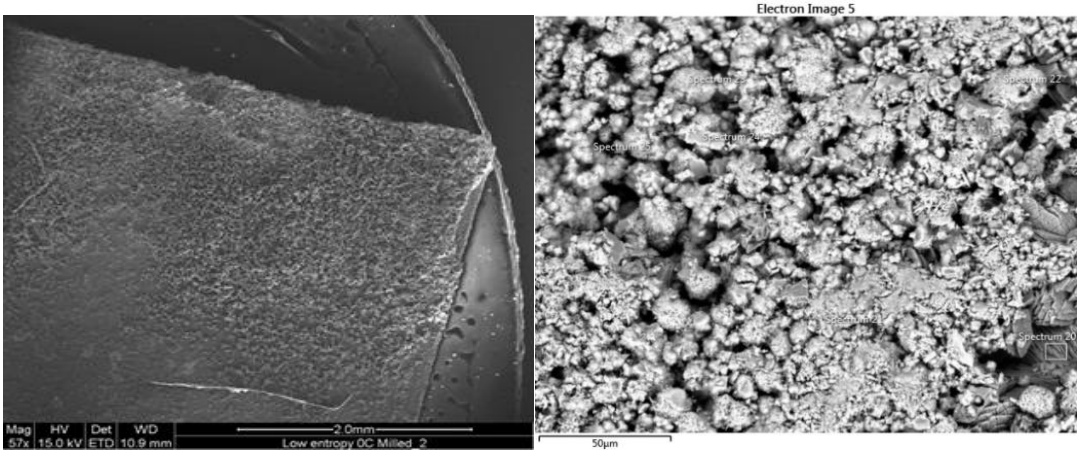

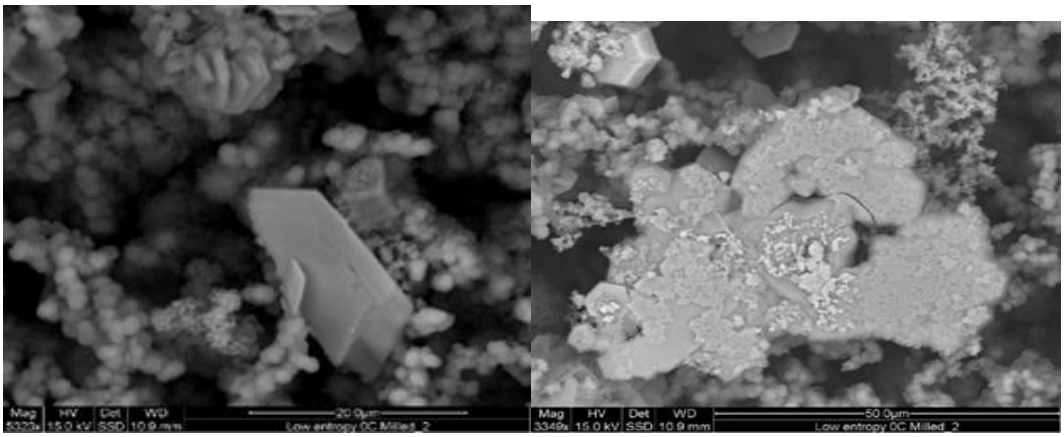

Figure 23 (a-d). SEM- micrographs of the corroded iron foils at different magnifications.

EDX analysis was conducted on multiple regions of the corroded iron foil surfaces, with each micrograph evaluated by averaging measurements from approximately 8–10 distinct spots. The compositional analysis indicates that the precipitated phases are predominantly composed of Fe (~ 85–90 at.%), while the remaining 10–15 at.% consists mainly of O_2, Si, Ca, Cl, and C. Trace amounts of Mn, Na, and Mo were also detected, which are most likely attributable to the evaporation of residual groundwater. The corresponding elemental distributions are presented in Fig. 24.Among the total of 82 EDX measurements acquired from different surface areas, U was detected in only a single micrograph, at a concentration of ~ 1 at.%. In this case, U was found in association with elements characteristic of the groundwater matrix, including Si, S, Fe, Cl, O_2, and Mo. This observation can be due to the drying of the leachate solution containing dissolved U(IV) species along with groundwater components.

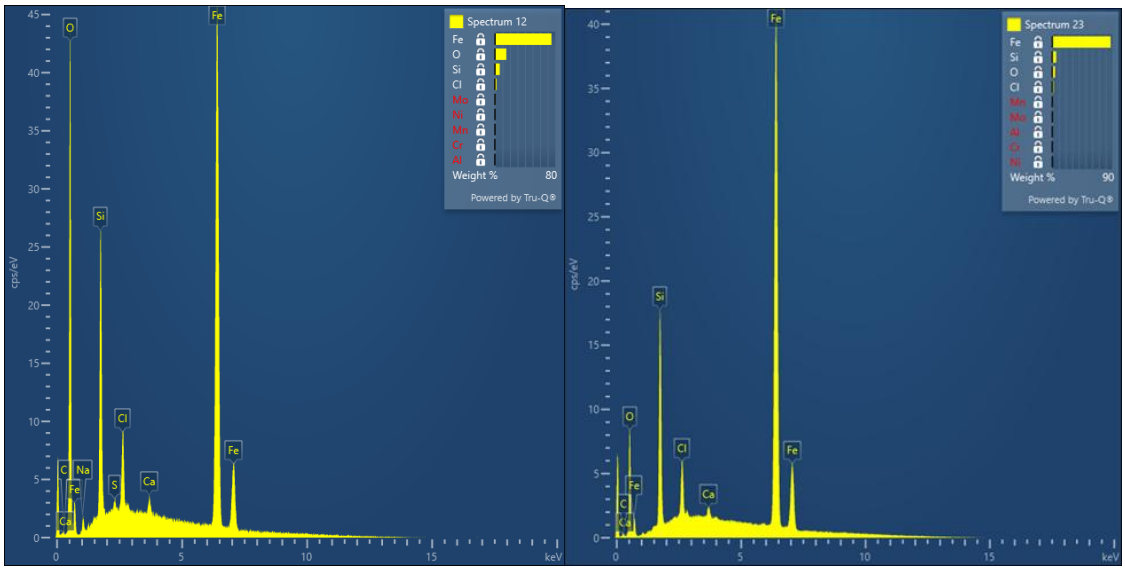

Figure 24. SEM-EDX spectrum on the corroded iron foils.

Elemental mapping was additionally performed on the corroded iron foils across multiple surface regions, covering a total of 13 distinct mapped areas. The mapping results consistently indicate the presence of Fe, O, Ca, and Si as the dominant elements. A representative full-area elemental map of the corroded iron surface is presented in Fig. 25.

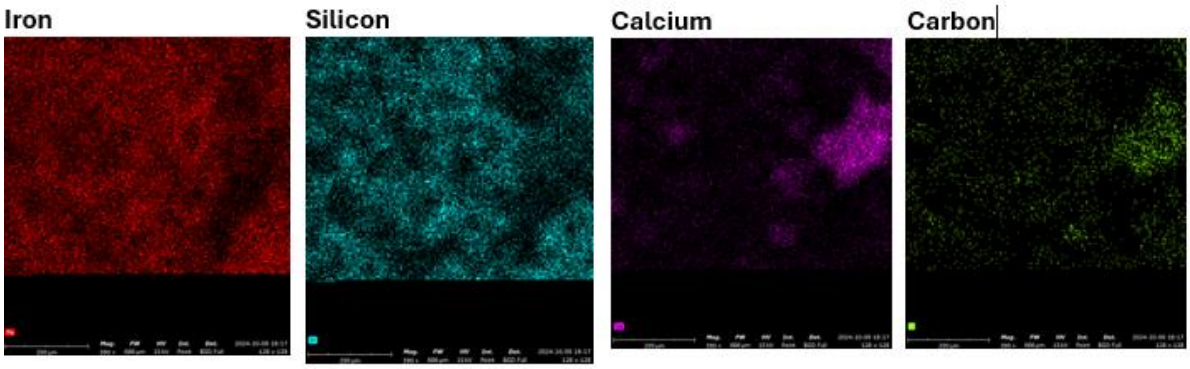

Figure 25. Mapping of the corroded iron foils.

Based on the SEM-EDX results, the formation of iron corrosion phases such as Fe(II) hydroxides and Fe(II) hydroxy-carbonates, in addition to calcite, is considered most likely to form. It should be noted that light elements such as H_2 and C, and O_2, are not easily quantified and detectable by EDX due to their low atomic numbers.

5.5.5. Raman spectroscopy analyses the corroded iron foils.

The Raman spectra collected from precipitates formed on the corroded iron surfaces are characterized by the Raman shifts in the ranges 1084-1086 cm^{-1} and 713-716 $cm^{-1,}$ along with a less intense peak at approximately 277-280 cm^{-1} and 154-55 cm^{-1}. These peaks correspond well with reported reference spectra for ankerite ($CaFe(II)(CO_3)_2$), as reported in the literature [92, 192] and in the RRUFF mineral database (ID: R050197).In some spots, the recorded spectra display similarities to calcite ($CaCO_3$), particularly with respect to the characteristic bands near 280 and 1086 cm^{-1}, consistent with reference data from the RRUFF database (ID: R050127). Additionally, some morphological features observed in Fig. 23c and 23d exhibit close resemblance to chukanovite, however, these specific areas were difficult to relocate and analyze using the Raman microscope.

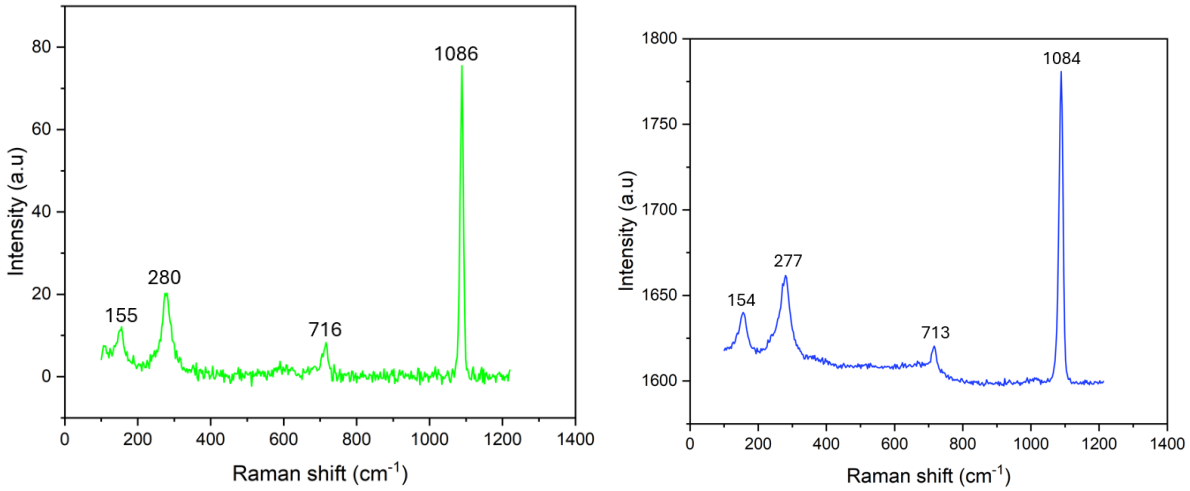

Figure 26. Raman spectra of the precipitates found on the surface of the corroded iron foils.

In summary, the combined results from the SEM-EDX analysis and Raman measurements indicate that the precipitate phases formed on the corroded iron foil surfaces are most likely to be ankerite, chukanovite, and /or calcite, while the formation of cronstedtite cannot be ruled out.

5.6. Leaching results in the presence of magnetite and chukanovite (paper V)

5.6.1 Evolution of the concentrations of U, Pu, and Fe during the leaching test in the presence of magnetite

The concentrations of U, Pu, and Fe were measured during the leaching of a MOX pellet in synthetic Forsmark groundwater in the presence of magnetite (Fe_3O_4). The experiment was carried out under an Ar atmosphere to maintain anoxic conditions. Dissolved concentrations of U and Pu were quantified using ICP-MS and were monitored throughout the experiment to evaluate the oxidative dissolution behavior of the MOX fuel pellet.

As illustrated in the Fig. 27, the measured U concentration increased from 2 x 10^{-8} M to 4 x10^{-6} during the first 50 days of leaching. Beyond this period, the rate of increase declined significantly, approaching a steady-state concentration toward the end of the 250-day experiment. Pu exhibited a similar trend to U, with an initial increase in concentration followed by a slower increase at later stages. The dissolved Fe concentration decreases over time from an initial value of 4 x 10^{-5} M at start to 4 x 10^{-6} M after 40 days, and declines further after 159 days.

These results indicate that the Fe(II) concentrations generated from Fe_3O_4 in equilibrium with Forsmark groundwater were insufficient to mitigate the strong alpha radiation field of the unirradiated MOX fuel pellet. Radiolytic processes promoted oxidative dissolution of the fuel matrix, leading to the formation of U(VI) and its subsequent release into solution, likely as aqueous uranyl-carbonate complexes. The relatively low Fe(II) levels suggest that the reducing front did not effectively propagate to the pellet surface.

Post-leaching characterization of the MOX fuel pellet did not detect Fe(III) secondary phases instead, only NaCl crystals were observed, attributed to evaporation of the residual solution. Comparing the results with analogous experiments conducted on SNF [18], the increase in U concentration observed in this study was less pronounced when compared with a similar experiment using SNF. This difference is likely related to the absence of gamma radiation in the present system, which may have resulted in slower oxidation and consumption of Fe(II) in the bulk solution relative to experiments involving irradiated fuel.

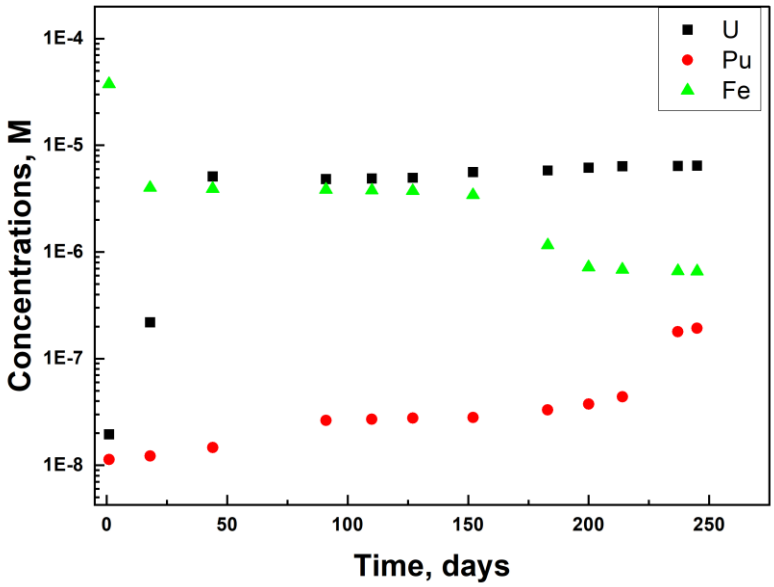

Figure 27. Evolution of U, Pu, and Fe concentrations in solution during leaching of the 10% Pu MOX pellet under Ar in Forsmark groundwater in the presence of magnetite

5.6.2. Solution of the concentrations of U, Pu, and Fe during the leaching test in the presence of chukanovite

The evolution of the total concentrations of U, Pu, and Fe during the leaching of the MOX pellet under an Ar atmosphere in the presence of synthesized chukanovite is presented in Fig. 28 as a function of leaching time. The uranium concentrations remain low, in the range of 2 $x10^{-9}$ M to $4x10^{-9}$ M, with only a slight decrease in concentration was observed over the duration of the experiment. No increase in the U concentrations, which could arise from its oxidative dissolution induced by the strong alpha radiation field of the MOX pellet, is observed. Instead, the results are quite similar to those observed during the leaching of the same MOX pellet under Ar in the presence of metallic iron [114].

The suppression of U oxidation can be attributed to the relatively high Fe(II) concentration established through equilibration between Forsmark groundwater and chukanovite. These reducing conditions effectively inhibit the oxidative effects or dissolution generated by the high alpha field of the MOX pellet. Pu concentrations are slightly higher than the solubility limit of PuO_2(am, hyd) reported as $10^{-10.4}$ M in [172]. Nevertheless, under the prevailing high Fe(II), the concentrations of Pu are quite similar to those reported in [189] for the reductive dissolution of PuO_2(am, hyd) in the presence of 1 mM Fe(II) in solution. The Fe(II) concentration remains essentially constant throughout the experiment. This steady-state behavior indicates that Fe(II) consumed by oxidizing species produced via alpha radiolysis (mainly H_2O_2) is continuously replenished through equilibrium with chukanovite.

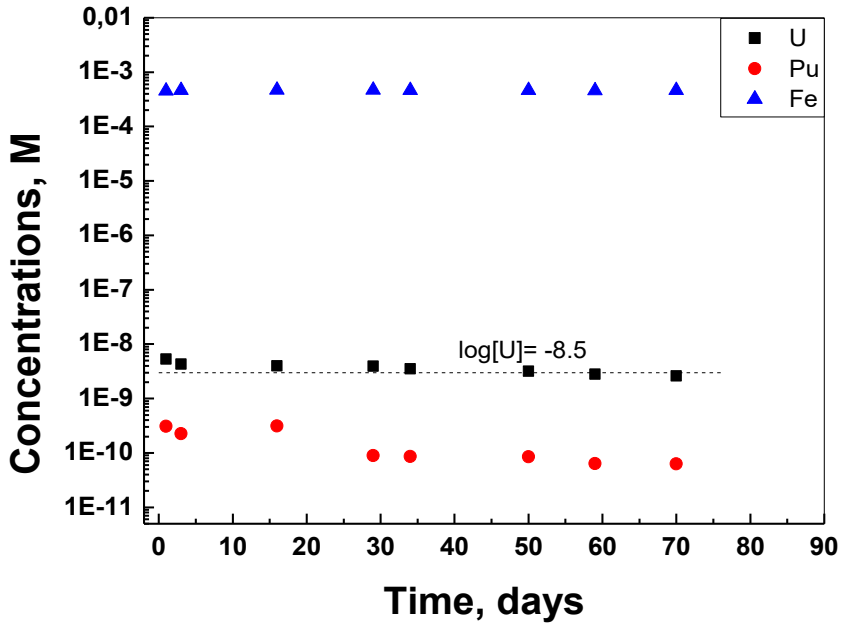

Figure 28. Evolution of U, Pu and Fe concentrations in solutions during leaching of the 10% Pu MOX pellet under Ar in Forsmark groundwater in the presence of chukanovite.

5.6.3 Analysis of the distribution of U and Pu in aqueous solution and sorbed/precipitated on solid surfaces in both the leaching test with magnetite and chukanovite

At the end of the leaching experiment in the presence of magnetite, the distribution of released U and Pu among the different system components was quantified. U was found predominantly in the aqueous phase, accounting for 86.2% of the total amount released (698.9 µg). A smaller fraction was associated with the quartz beaker insert (1.7%, 13.8 µg), while 12.3% (99.7 µg) was retained on magnetite surfaces. The limited retention on magnetite is consistent with the relatively weak sorption affinity of oxidized U species, particularly U(VI) carbonate complexes. In the case of Pu, ~ 47.5% (19.9 µg) was associated with the quartz insert surfaces, while 48.7% (20.4 µg) remained dissolved in solution. Only a minor fraction, 3.7% (1.6 µg), was sorbed onto magnetite.

The distribution of U and Pu released during the leaching of MOX fuel in the presence of chukanovite was also quantified. A total concentration of 9.86 µg for U and 2.03 µg for Pu was released during the entire leaching test. U was predominantly associated with chukanovite, accounting ~ 70% of the total released mass, while 26.7% was found sorbed on the surface of the glass vessel insert and only 3.3% remained in solution. Pu exhibited markedly different behaviour, with majority (~96%) sorbed onto the glass vessel insert surfaces, 3.6% was sorbed onto chukanovite, and less than 0.5% was detected in the aqueous phase.

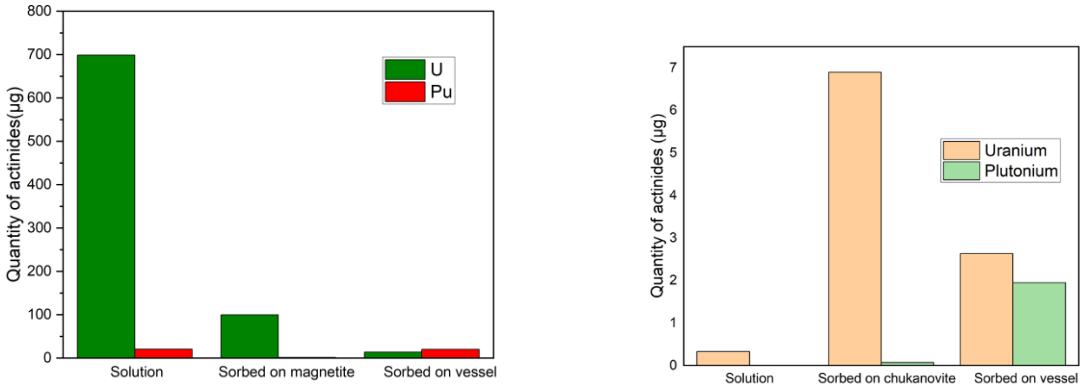

Figure 29: U and Pu partitioning among the solution, sorbed on the quartz glass beaker insert, and sorbed on the magnetite (left) and chukanovite (right) at the end of the leaching experiment.

5.7. Solid characterization of the leached MOX pellet in the presence of magnetite and chukanovite

5.7.1. Results of powder X-ray diffraction for magnetite (P-XRD)

The solid magnetite used in the leaching experiment was characterized by P- XRD, as shown in Fig. 30. The obtained diffractogram displays a narrow, distinct, and sharp peak, indicative of well-crystallized phases. Comparison of the XRD pattern with reference data from the ICDD database confirmed that the observed peaks correspond to the expected crystallographic features of magnetite.

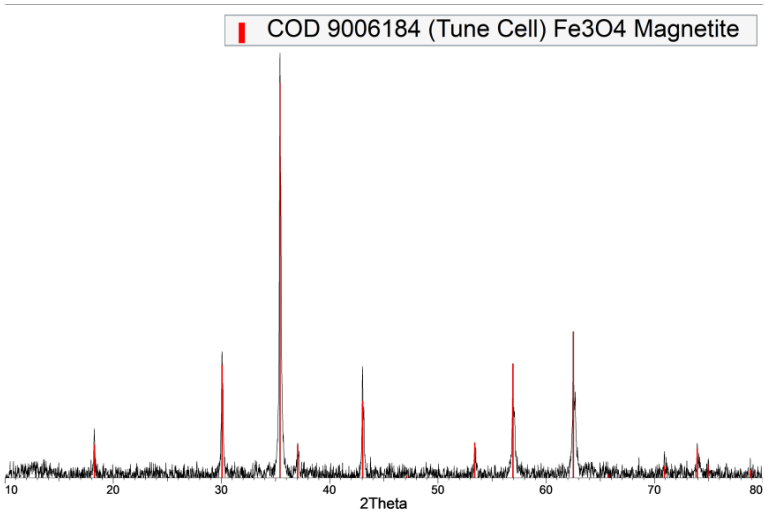

Figure 30: P- XRD measurement of the magnetite used during the autoclave leaching experiment.

5.7.2 FT-IR and Raman spectroscopy results of the synthesized chukanovite

The FTIR spectra of solids synthesized display dominant absorption bands at 3482, 3323, 1520, 1364, and 838 cm^{-1}, corresponding to hydroxyl and carbonate vibrational modes typical of Fe(II)

hydroxycarbonates [193]. No bands characteristic of $Fe(OH)_2$ (3624 cm^{-1}), siderite (1415 cm^{-1}), or Fe(III) phases such as lepidocrocite and goethite were observed [194, 195]. The spectra show three main regions: O–H stretching (~3482 and 3315 cm^{-1}), antisymmetric carbonate stretching (1520–1357 cm^{-1}), and out-of-plane carbonate bending (~838 cm^{-1}), the latter being characteristic of chukanovite [193]. Despite weaker O–H features, the presence of both hydroxyl and carbonate groups supports the identification of chukanovite as the predominant phase. Raman spectroscopy was performed on the synthesized solid precipitates to determine their nature. The recorded spectra (Fig. 31), collected from multiple surface locations, were in good agreement with reference spectra of chukanovite reported by Remazeilles and Refait [193].In particular, the prominent Raman band at approximately 1078 cm^{-1} is consistent with the characteristic peak of chukanovite [92, 193].

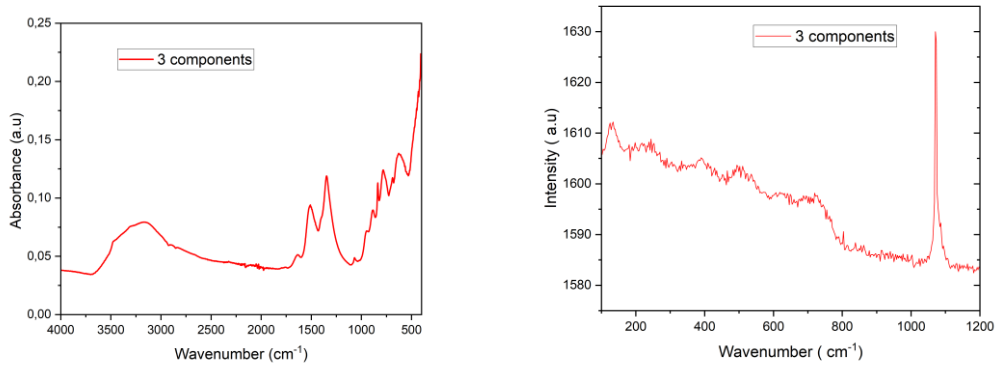

Figure 31: (a) FT-IR spectra, (b) Raman spectra of the synthesized solid chukanovite precipitates

5.7.3 SEM-EDX analysis of the leached MOX fuel pellet in the presence of magnetite

The surface of the MOX pellet after a 245-day leaching experiment in the presence of magnetite was examined at test termination. Visual inspection shows the formation of small precipitates on the pellet surface as observed in Fig 32.

The surface morphology and elemental composition were further characterized using SEM-EDX.SEM micrographs of the corroded MOX pellet, leached in synthetic Forsmark groundwater, were obtained with a Hitachi TM 3000 tabletop SEM housed within the glove box. Small deposits or precipitates can be observed on the surface of the MOX pellet. EDX elemental analysis shown in Fig.34, indicates that the surface precipitates are primarily composed of Na and Cl, likely resulting from the evaporation of the synthetic groundwater.

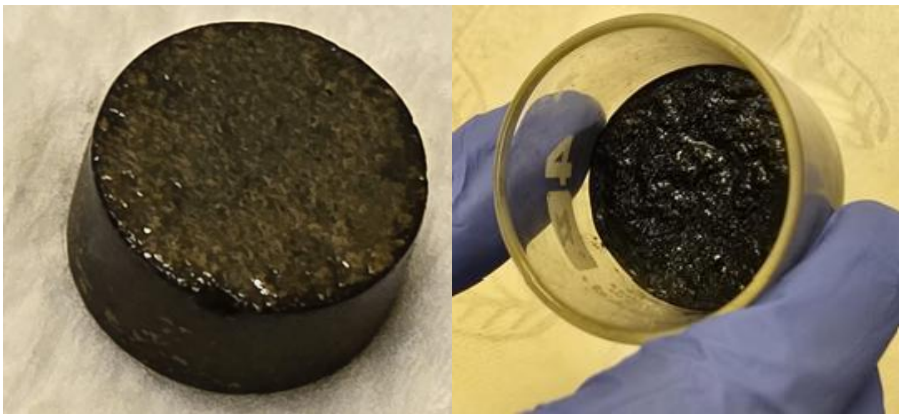

Figure 32. Visual inspection of the corroded MOX pellet and leached magnetite when extracted from the autoclave.

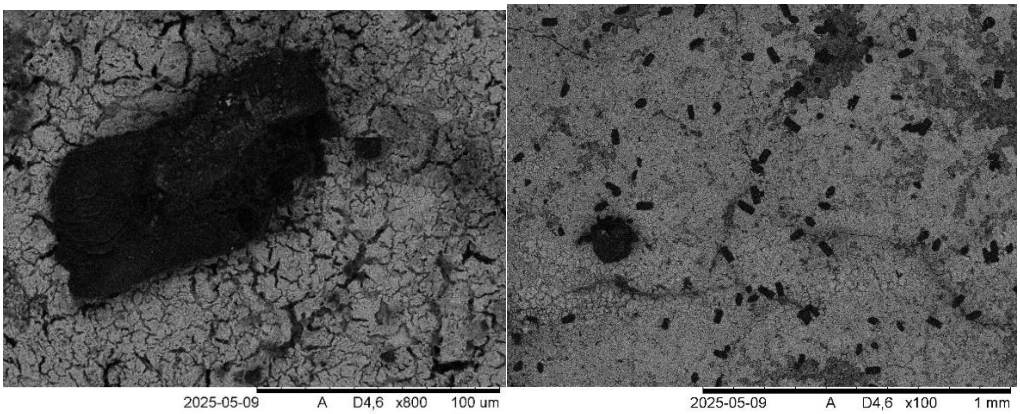

Figure 33: SEM micrographs of the corroded MOX fuel pellet in the presence of magnetite.

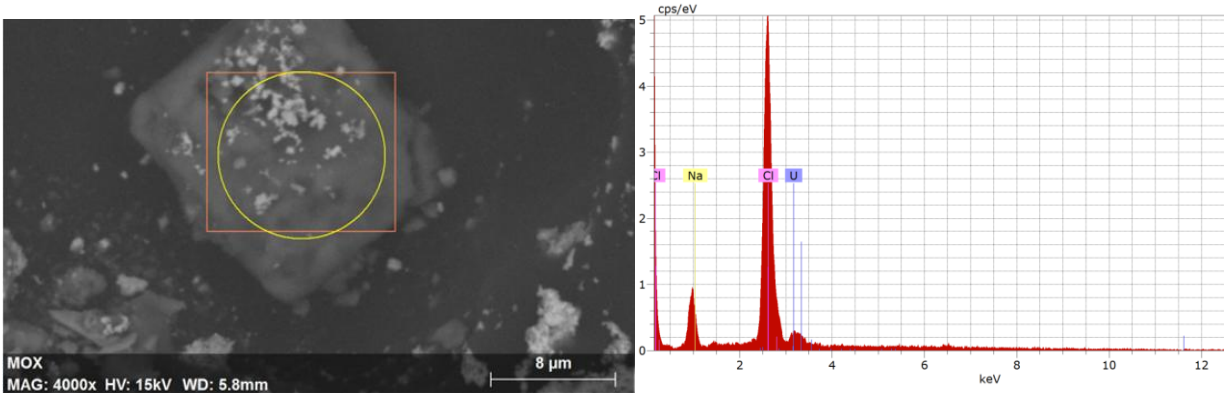

Figure 34: SEM-EDX analysis of the precipitates formed on the surface of the leached MOX pellet in the presence of magnetite.

5.7.4. SEM-EDX analysis of the leached MOX pellet in the presence of chukanovite

The surface of the MOX pellet was characterized by SEM-EDX at the end of the leaching test in the presence of chukanovite. Fig. 35 reveals that the pellet surface was entirely covered by reddish

precipitates formed during the leaching process. SEM micrographs show that the surface layer consists of a few micro- to nanoscale precipitates with a granular morphology.

Elemental analysis by EDX indicates that the surface deposits are mainly composed of Fe and O_2, with no detectable U in the analyzed regions. These observations suggest that the secondary phases mainly consist of iron-bearing compounds formed at the fuel-water interface, likely as a result of Fe(II) oxidation to Fe(III). Comparable investigations of MOX fuel in contact with metallic iron have reported the precipitation of iron oxyhydroxide phases, such as akageneite (β-FeOOH), on the leached MOX fuel surface [114].

Figure 35. Visual inspection of the corroded MOX pellet and leached chukanovite when extracted from the autoclave at the end of the experiment.

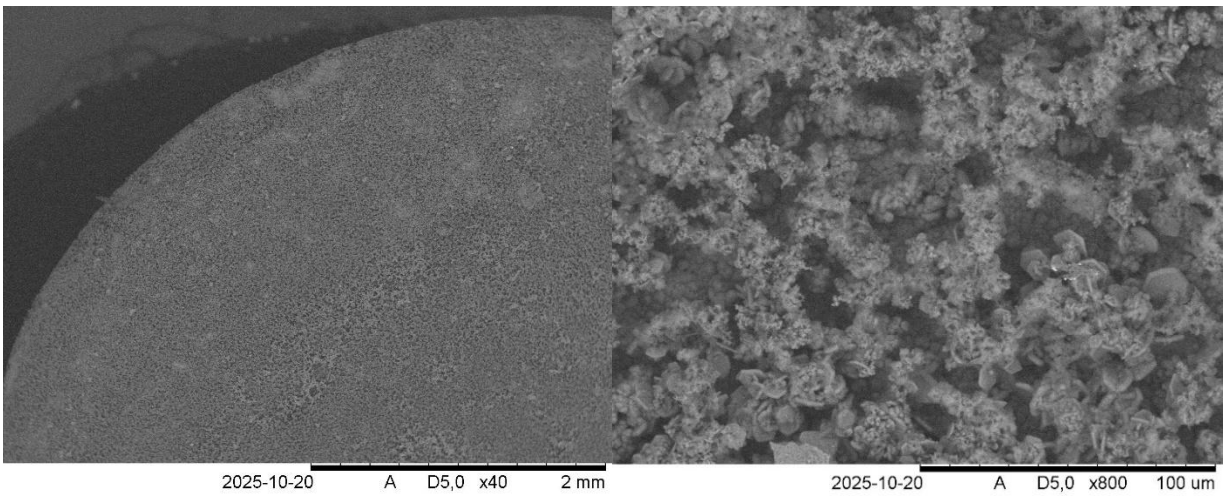

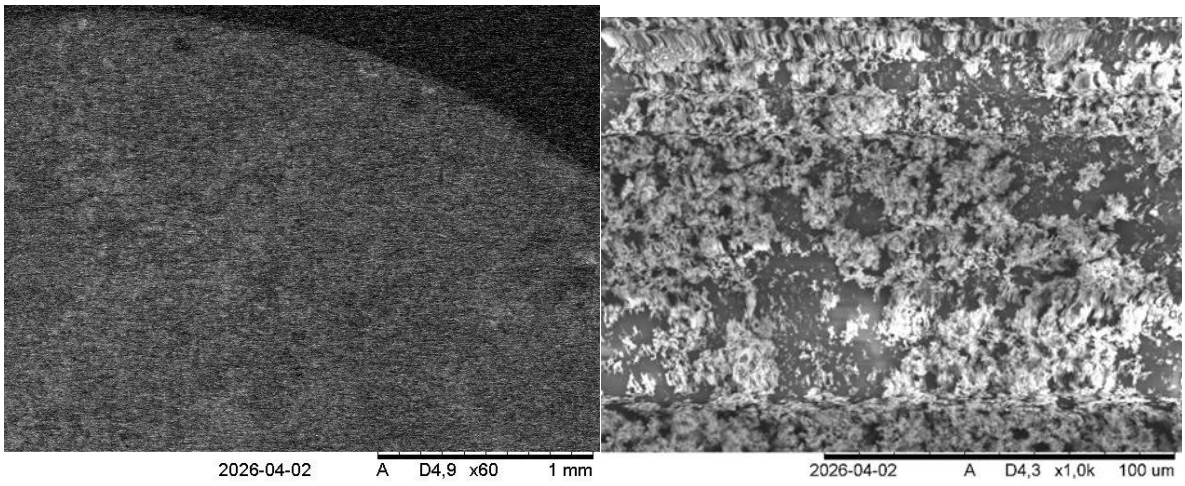

Figure 36. SEM micrographs of the leached MOX pellet in synthetic Forsmark groundwater in the presence of chukanovite.

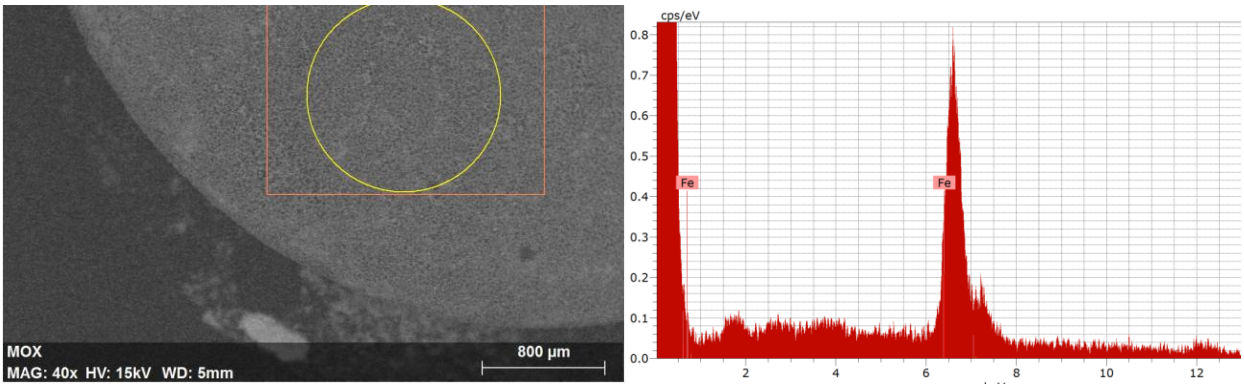

Figure 37. EDX analyses the precipitates formed on the leached MOX pellet surface in the presence of chukanovite.

5.8. U-Ce Coprecipitation results (paper II)

To determine whether equilibrium has been reached between the aqueous and solid phases, to identify the nature of solid solutions formed, and to develop accurate interpretations of the solubility data. Data obtained from both liquid and solid characterizations were analyzed. The findings are discussed below.

5.8.1. U concentrations in equilibrium with the $Ce_{0.01}U_{0.99}$ co-precipitate solid

The behavior of U in equilibrium with the coprecipitated solid containing 1% mole fraction of Ce ($Ce_{0.01}U_{0.99}$) is expected to be quite similar to that of the amorphous UO_2(s). Fig. 38 compares the U concentration data at 30 days with literature solubility measurement data of UO_2(am) in 1 M NaCl [195, 196]. In the $-\log[H^+]$ range of 2-4, the U concentration data are quite similar to those observed in the studies of Rai and coworkers [196,197], where U concentrations decrease by approximately three orders of magnitude for each pH unit increase in $-\log[H^+]$. The dominant hydrolysis species in this interval is the first hydrolysis complex $U(OH)^{3+}$, which is consistent with

several previous studies on UO_2(am) solubility. The corresponding equilibrium reaction for UO2(am) with solution in this pH range is:

$$UO_2(am) + 3\ H^+ \rightleftharpoons U(OH)^{3+} + H_2O(l) \qquad (46)$$

$$*K_{s3} = [U(OH)^{3+}]\ [H^+]^{-3} \qquad (47)$$

At higher –log[H^+] values >4, the measured U concentrations for the $Ce_{0.01}U_{0.99}$ containing solids are consistent with the lower solubility limit of reported for UO_2(am) in this –log [H^+] range (Grenthe and coworker, log [U] = –8.5±1) [16] and with U concentrations from spent fuel leaching tests around pH 8 [18, 207, 208]. The equilibrium reaction is written as :

$$UO_2(am) + 2\ H_2O \rightleftharpoons U(OH)_4(aq) \qquad \log K^0_{s,4} = -8.5\pm1 \qquad (48)$$

The corresponding equilibrium constant expression is defined in terms of activities as:

$$\log K_{s,4} = \frac{\{U(OH)_4(aq)\}}{a^2 w} \qquad (49)$$

The superscripts zero in $K^0_{s,4}$ indicate that the constant is defined at infinite dilution (I=0), where the activity of water is equal to unity. Under the experimental condition of 1 M $NaClO_4$, the activity of water deviates slightly from unity. However, this deviation is small and does not significantly affect the value of log $K_{s,4}$. The U data corresponds to some of the lowest reported values for similar systems, suggesting the absence of U(VI).

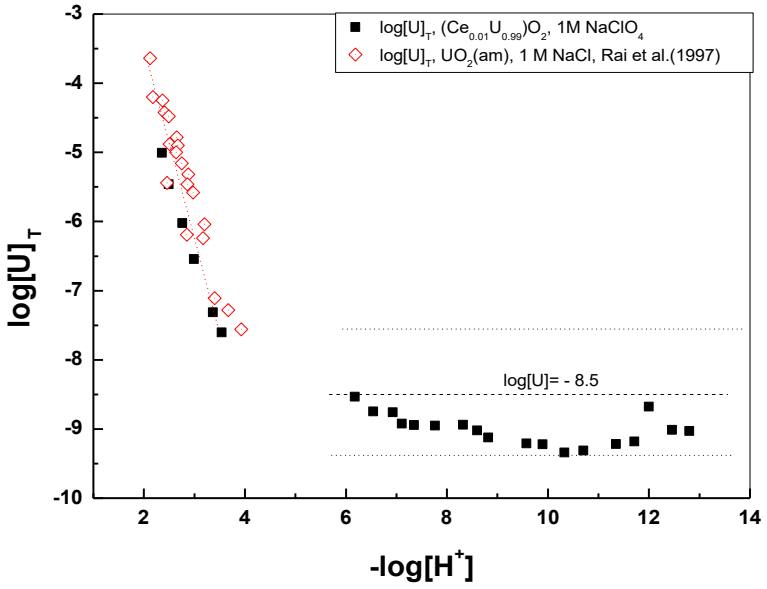

Figure 38. U concentrations in equilibrium with the $Ce_{0.01}U_{0.99}$ solid solution at 30 days. The dotted line with slope -3 is derived from Figure 5 in Rai and coworkers [196], while the horizontal dotted lines represent log[U] = –8.5±1. The data from [196] corresponds to an equilibration period of 8-420 days.

5.8.2. Ce(III) concentrations in equilibrium with the co-precipitate solids ($Ce_{0.01}U_{0.99}$ and $Ce_{0.10}U_{0.90}$)

The measured equilibrium concentrations of Ce(III) in contact with the $Ce_{0.01}U_{0.99}$ co-precipitate are slightly lower than the corresponding U concentrations at –log [H^+] values above 6. While in the acidic region (–log [H^+] of 2-4), the Ce concentration decreases by more than an order of magnitude than that of U at the lowest –log [H^+] and becomes slightly less as the –log [H^+] increases. These observations indicate that the presence of pure $Ce(OH)_3(s)$ in the solid phase can be excluded, as such a phase would dissolve completely under these conditions (–log [H^+] interval of 2-4), producing Ce concentrations considerably higher than those measured. Moreover, the data suggests that the co-precipitate does not behave as an ideal homogeneous solid solution. In an ideal solid solution, the Ce concentration in solution would decrease proportionally with its mole fraction in the solid (0.01), relative to the solubility of pure $Ce(OH)_3(s)$. Instead, the formation of a solid solution in which Ce is the minor component appears to influence the measured concentration of Ce. Experimental data reported by Kragten and Denkop-Weaver [198] indicate that $Ce(OH)_3(s)$ in 1 M $NaClO_4$ begins to precipitate at ~ –log [H^+] 7 and dissolves completely at –log [H^+] values below 4 (see Fig. 39).

At –log[H^+] values above 9.9, the solubility of pure $Ce(OH)_3(s)$ in 1 M $NaClO_4$ remains constant at log $[Ce]_T$ = –5.9, reflecting the dominance of the neutral aqueous species $Ce(OH)_3(aq)$ in solution.

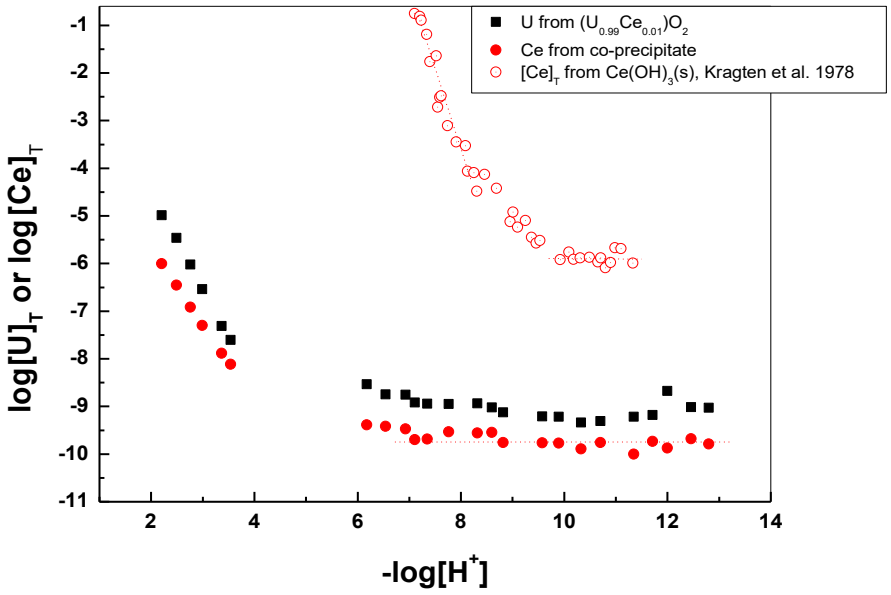

Figure 39. Concentrations of Ce and U in equilibrium with $Ce_{0.01}U_{0.99}$ oxide co-precipitate compared with concentrations of Ce in equilibrium with $Ce(OH)_3(s)$ (Kragten and Denkop-Weaver [198]) at 1 M $NaClO_4$.

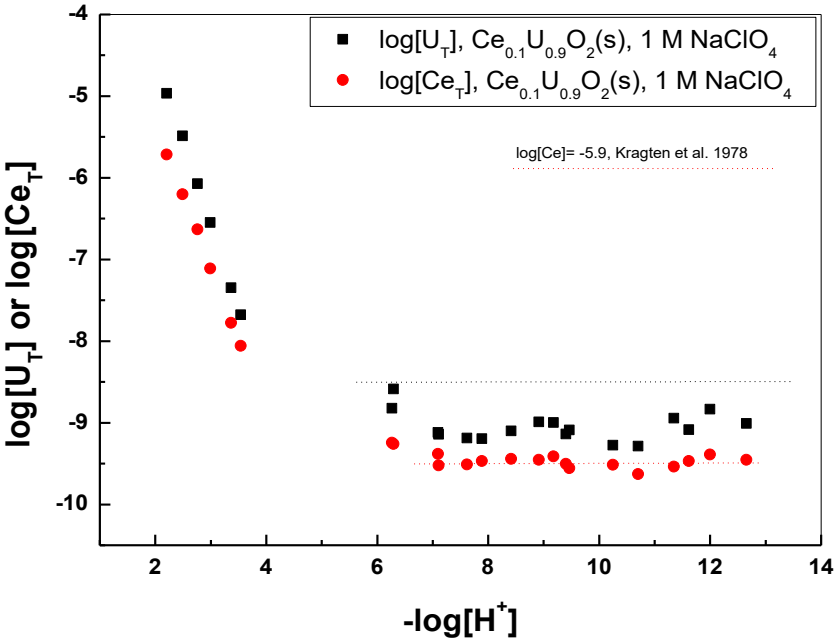

Figure 40. Concentrations of Ce and U in equilibrium with $Ce_{0.10}U_{0.90}$ oxide co-precipitate. The dotted lines in the basic range indicate the solubility of $UO_2(s)$, log[U] = –8.5, and the horizontal part of Ce concentrations for the pure oxide and the coprecipitate.

5.8.3. Estimation of the activity, activity coefficient, and solid phase composition dependent constant K_x from the Co-precipitates solids

U and Ce concentrations were evaluated over two pH ranges, $-\log[H^+]$ 2.2-3.6 and $-\log[H+]$ 6.5-12.8, corresponding to regions where different aqueous species are expected to dominate, as described in the thermodynamic model presented in Section 3.5.

In the acidic region ($-\log[H^+]$ 2.2–3.6), the dissolution of $Ce(OH)_3(s)$ is governed primarily by the reaction below:

$$Ce(OH)_3(s) + 3\ H^+ \rightleftharpoons Ce^{3+} + 3\ H_2O(l) \qquad (50)$$

Within this pH range, the formation of hydrolyzed Ce(III) species is not expected to exist. By considering the thermodynamic equilibrium constant, the concentration of Ce in equilibrium with the co-precipitate, the constant activity coefficients, and the activity of water in 1 M $NaClO_4$ into the conditional constant $*K_{s0}$, we have :

$$\log [Ce^{3+}] = \log *K_{s0} - 3(-\log[H^+]) + \log a_{Ce(OH)_{3(s)}} \qquad (51)$$

where the conditional solubility product ($Ce(OH)_3(s)$ in 1 M $NaClO_4$ was reported as $\log *K_{s0}$ = 20.1 by Kragten and Dencop-Weaver [198].

As discussed in Section 3.5, the composition-dependent parameter K_x can be estimated by fitting the experimental $\log[Ce^{3+}]$ data in the acidic region to a linear relationship with a fixed slope of –3 and extrapolating to $-\log[H^+] = 0$, based on the relation:

$$\log [Ce^{3+}] = \log K_x - 3(-\log[H^+]) \qquad (52)$$

Although hydrolyzed species such as $Ce(OH)^{2+}$ are not expected to form under these conditions, the experimental data exhibit a slope closer to –2 than –3. This deviation is likely related to the difficulty of describing the solubility of a phase that is thermodynamically unstable in this pH range. To obtain a reasonable estimate of K_x, lines with a fixed slope of -3 were constructed through individual data points, and the corresponding intercepts were used to calculate K_x.These results are summarized in Table 6.

Table 6: Estimates of log K_x, $a_{Ce(OH)_3(s)}$ and $\lambda_{Ce(OH)_3(s)}$ derived from data in the $-\log[H^+]$ range 2.2-3.6.

$X_{Ce(OH)_3(s)}$	log K_x	log $a_{Ce(OH)_3(s)}$	log $\lambda_{Ce(OH)_3(s)}$
1	20.1	0.00	0.00
0.1	2.5±0.7	–17.6 ±0.7	–16.6±0.7
0.01	2.3±0.7	–17.8±0.7	–15.8±0.7

The obtained values are approximately 18 orders of magnitude lower than those reported by Kragten and Decnop-Weaver [198] for the pH region where $Ce(OH)_3(s)$ exists. The activity of $Ce(OH)_3(s)$ in the solid phase was estimated by subtracting the value of log $*K_{s0}$ (20.1) from the corresponding log K_x values. The calculated equilibrium activities are also summarized in Table 6. Furthermore, the activity coefficients of the solid phase (λ) were derived from the relationship between the activity and composition expressed as :

$$a_{Ce(OH)_3(s)} = x\ \lambda_{Ce(OH)_3(s)} \qquad (53)$$

As shown in Table 6, K_x values exhibit a slight increase with increasing mole fraction x, for the composition investigated, suggesting behaviour consistent with a solid solution. For both compositions investigated, the equilibrium concentrations of Ce remain consistently lower than those of U across the entire pH range. However, these results should be interpreted with caution due to the considerable uncertainties associated with determining the conditional solubility product of $Ce(OH)_3(s)$ from coprecipitated systems in a pH region where the pure solid phase is not stable or cannot exist.

In the basic region (–log[H+] 6.5-12.8), assuming that $Ce(OH)_3(aq)$ is the dominant species in solution, the total dissolved Ce concentration can be expressed as:

$$\log [Ce]_T = \log *K_{s0} + \log *\beta_3 \qquad (54)$$

where $*\beta_3$ is the conditional formation constant in 1 M $NaClO_4$ corresponding to the equilibrium:

$$Ce^{3+} + 3\ H_2O(l) \rightleftharpoons Ce(OH)_3(aq) + 3\ H^+ \qquad (55)$$

Under these conditions, the equilibrium expression becomes:

$$\log [Ce] = \log K_x + \log *\beta_3 \qquad (56)$$

By using the value log $*\beta_3 = -26$ reported by Kragten and Dencop-Weaver [198], for 1 M $NaClO_4$, the constants corresponding to different Ce mole fractions (log $K_{0.01}$ and log $K_{0.1}$) can be

determined from the experimentally measured Ce concentrations at high –log[H^+] values. As illustrated in Figs. 39 and 40, at –log[H^+] > 9.5, the dissolved Ce concentrations are controlled by congruent dissolution of the coprecipitate with UO_2(s), showing a consistent decrease relative to U concentrations.

Table 7 summarizes the values of K_x derived from Ce concentrations in equilibrium with the co-precipitates at –log[H^+] > 9.5, together with the corresponding activities and activity coefficients (λ) of $Ce(OH)_3$ in the solid phase. As shown in Figs. 39 and 40, the horizontal part in Ce(III) concentrations extends into the intermediate pH range (–log[H^+] ≈ 6–9.5), even though the solubility of pure $Ce(OH)_3$(s) increases steeply in this region due to the formation of aqueous species such as Ce^{3+} and its hydrolyzed complexes. This behaviour provides further evidence that the release of Ce(III) from the co-precipitate is not governed by the intrinsic solubility of $Ce(OH)_3$(s), but is instead controlled by the release of the U.

Table 7. Values of log K_x, $a_{Ce(OH)_3(s)}$ and $\lambda_{Ce(OH)_3(s)}$ estimated from data –log [H^+] > 9.5.

$X_{Ce(OH)_3}$	log K_x	log $a_{Ce(OH)_3(s)}$	log $\lambda_{Ce(OH)_3(s)}$
1	20.1	0.00	0.00
0.1	16.5	–3.6	–2.6
0.01	16.3	–3.8	–1.8

As presented in Table 7, the $K_x$values show a slight increase with increasing mole fraction x for the compositions investigated. The corresponding activity coefficients of $Ce(OH)_3$ in the co-precipitate are negative and significantly lower than unity, suggesting highly favorable mixing within the solid phase. The solubility and hydrolysis data reported by Kragten and Decnop-Weaver [198] were employed in the present analysis, as they remain the only available dataset for Ce(III) in 1 M $NaClO_4$ under conditions comparable to this study. In particular, their experiments involved freshly precipitated $Ce(OH)_3$(s) equilibrated over time periods ranging from one week to one month, which is consistent with the equilibration conditions of the co-precipitates investigated here.

To enable comparison with more recent studies on lanthanide hydrolysis, these data were extrapolated to zero ionic strength using the Specific Ion Interaction Theory (SIT). This extrapolation yielded a solubility product of log $K^0_{s,0}$= 18.8 and a hydrolysis constant for $Ce(OH)_3$(aq) of log β^0_3= –24.7. These values are in good agreement with those reported in more recent literature, supporting the reliability of the older data [199, 200]. Although a comprehensive evaluation of Ce(III) hydrolysis was beyond the scope of this work, this comparison provides confidence that the thermodynamic data used in the present analysis are appropriate and reasonable.

5.9. Characterization of the U-Ce solid phase

5.9.1. Total chemical analysis from the U-Ce coprecipitate solids

The molar ratios of U-Ce in the solid phases were determined before and after equilibration. Small amounts of the solids, 30 - 40 mg, were completely dissolved in 2 M HNO_3, and the resulting solutions were analyzed by ICP-MS to quantify the elemental composition. Similar results were

obtained after 30 days of equilibration and after an extended period of 93 days at pH 8.2, as summarized in Table 8.

Table 8. Analytical molar fractions of U and Ce in the initial and equilibrated solids.

Target composition	Before equilibration		93 days of equilibration	
Ce_xU_{1-x}	Ce	U	Ce	U
$Ce_{0.01}U_{0.99}$	0.01	0.99	0.01	0.99
$Ce_{0.10}U_{0.90}$	0.09	0.90	0.09	0.90

The composition of the solids after equilibration remained essentially unchanged compared with the solid before equilibration. The longer equilibration time for the different sets of coprecipitated solids was selected to allow comparison with previous studies by Rai and coworkers [201], who reported extended equilibration periods for solid-phase characterization relative to the reported solubility measurement.

5.9.2. SEM-EDX results for the U-Ce coprecipitate solids

The U–Ce solid samples were characterized before and after equilibration using SEM-EDX in backscattered electron mode. The micrographs revealed a uniform morphology with no visible compositional difference, indicating the absence of regions enriched in either U or Ce. EDX analysis of the sample containing 10% Ce (see Fig. 42) showed that U and Ce are homogeneously distributed in the coprecipitated solid sample. Initial scans were performed over the entire powder on the SEM holder, followed by analyses of areas displaying features such as agglomerates and other features. In all analyzed regions, EDX results consistently indicated a uniform distribution of U and Ce in the solid. Elemental mapping analysis also confirms the homogenous distribution of U and Ce in the solid samples.

For the sample containing 1% Ce, the Ce concentration was below the detection limit of EDX. The absence of compositional heterogeneity and the uniform elemental distribution suggest that the solid samples consist of a single solid phase rather than a mixture of separate phases. Similar observations were obtained after equilibration, with no additional phases detected and the homogeneous distribution of U and Ce preserved (see Fig. 44), supporting the formation of a solid solution.

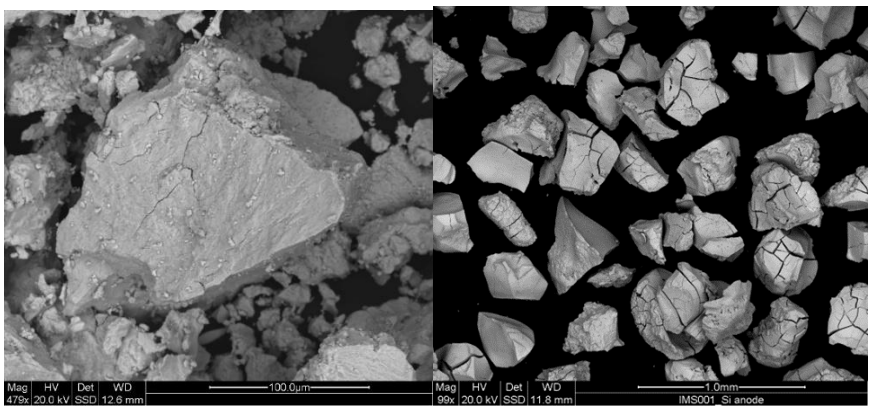

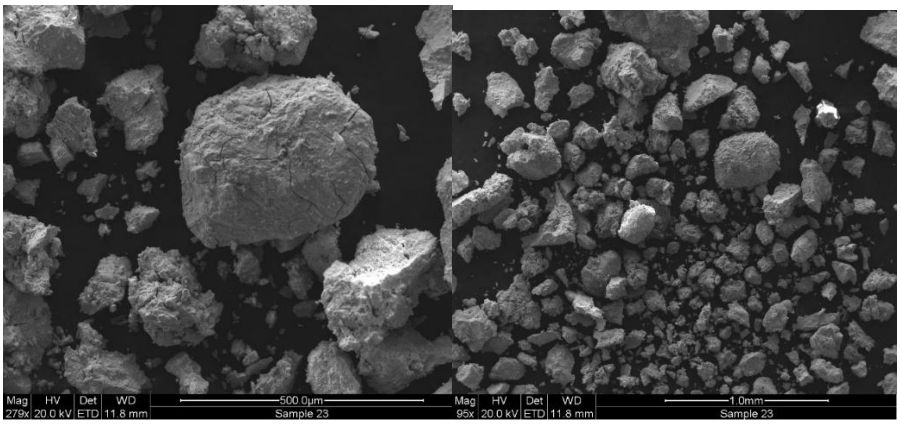

Figure 41. SEM micrographs of solid samples before and after equilibration in $NaClO_4$ solutions ($Ce_{0.01}U_{0.99}$, top figure; $Ce_{0.10}U_{0.90}$, bottom figure).

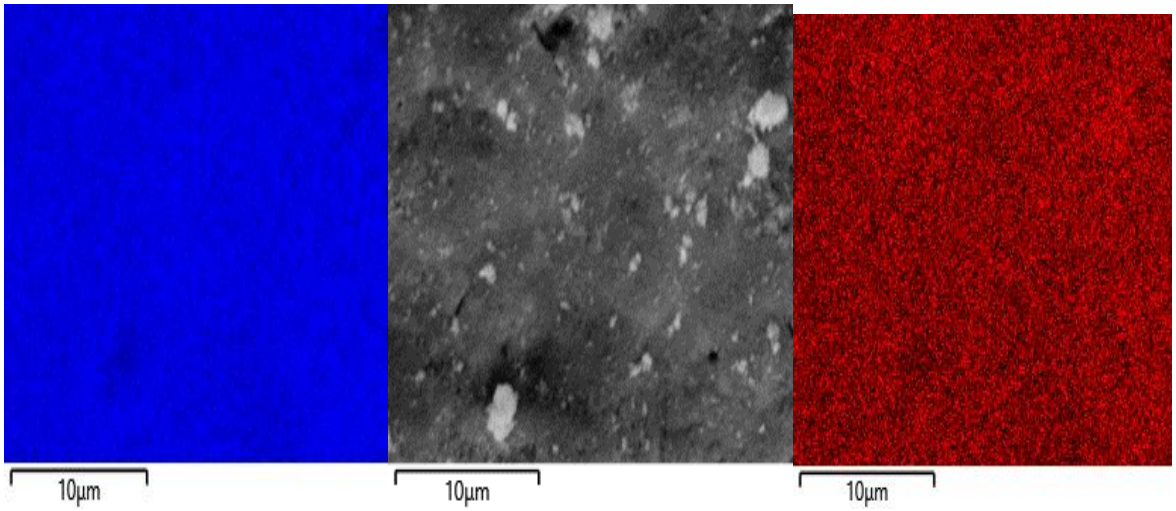

Figure 42. SEM micrograph of ($Ce_{0.10}U_{0.90}$) $O_{2\pm x}$ solid (center) and SEM-EDX U mapping (left) and Ce mapping (right) of the same area. Analysis made before equilibration.

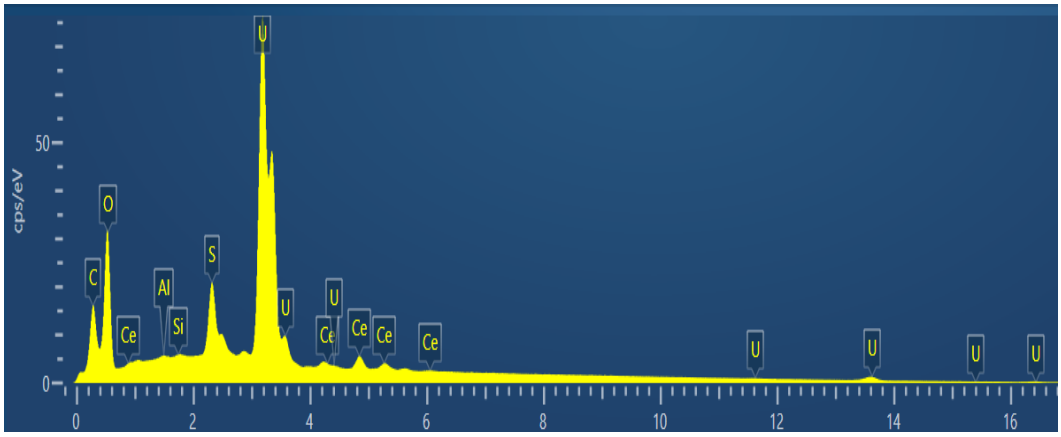

Figure 43. SEM-EDX spectrum of the $Ce_{0.10}U_{0.90}$ solid. Solid after equilibration, S originates from dithionite.

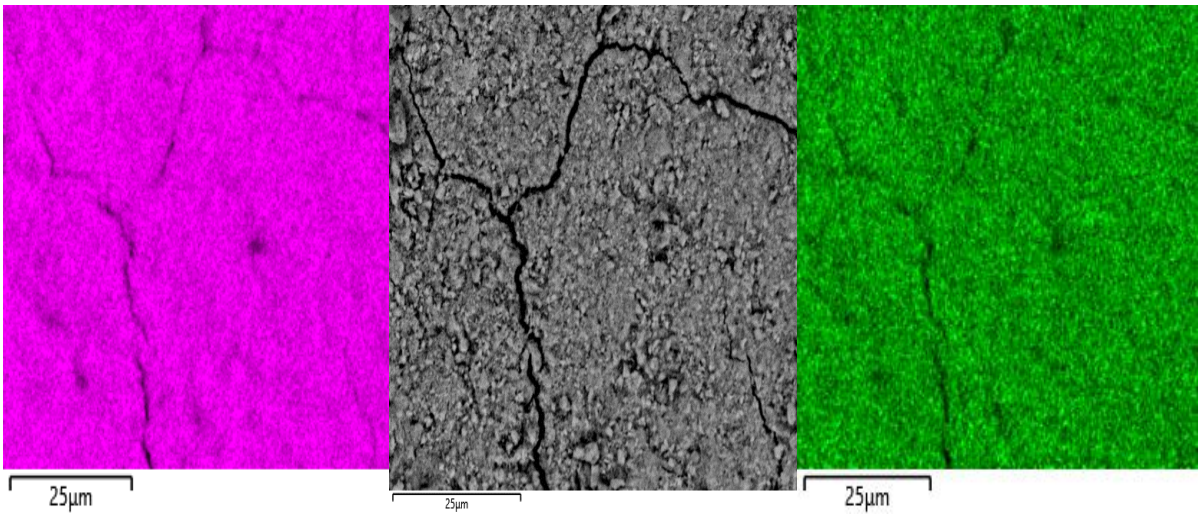

Figure 44. SEM micrograph of ($Ce_{0.10}U_{0.90}$) $O_{2\pm x}$ solid (center) and SEM-EDX U mapping (left) and Ce mapping (right) of the same area. Analysis made after equilibration.

5.9.3. XRD results for the U- Ce coprecipitate solids

The X-ray diffraction patterns of the solids collected before and after equilibration show a broad and not well-defined peak, as shown in Fig.45. Such diffraction features indicate that the precipitated solids are mainly amorphous, although the presence of minor microcrystalline cannot be completely excluded. These observations suggest that the solubility-controlling solids are primarily amorphous.

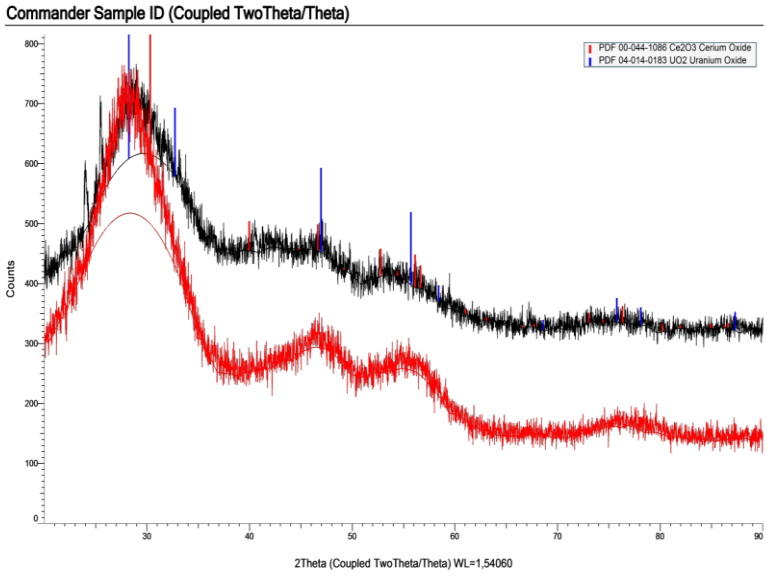

Figure 45. XRD pattern of the $Ce_{0.10}U_{0.90}$ solid before (upper) and after (lower) equilibration.

The solid co-precipitate samples sintered at 900 °C under reducing conditions exhibited sharp and well- defined crystalline narrow peaks for both $Ce_{0.01}U_{0.99}$ and $Ce_{0.10}U_{0.90}$ solid compositions, as illustrated in Fig.46. The presence of these sharp and narrow peaks indicates the formation of well-crystallized phases following the high-temperature treatment.

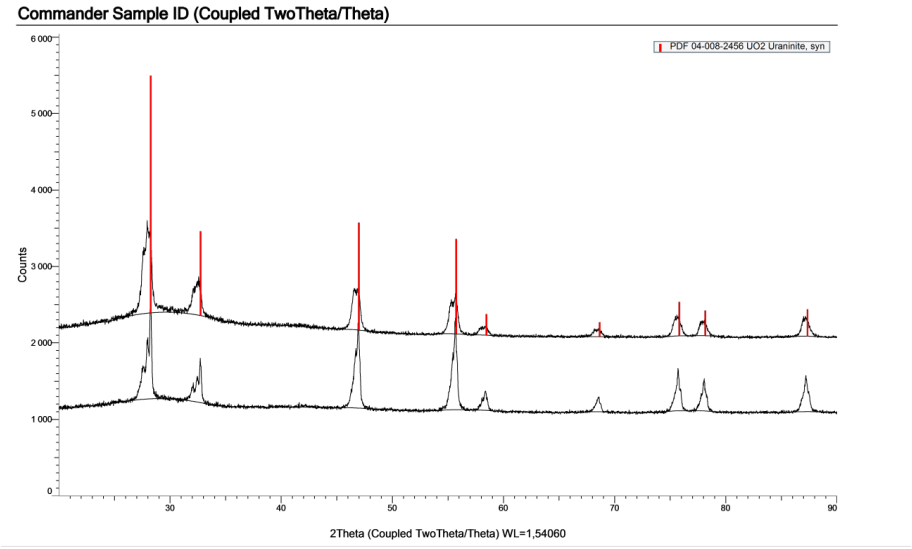

Figure 46: XRD pattern of the U-Ce equilibrated solid heated at 900 °C under reducing conditions. The upper pattern is for $Ce_{0.10}U_{0.90,}$ while the lower pattern is for $Ce_{0.01}U_{0.99.}$

The lattice parameters of the sintered coprecipitated solids were refined using the GSAS-II software [202]. The refinement was performed for both $Ce_{0.01}U_{0.99}$ and for $Ce_{0.10}U_{0.90}$ solid samples obtained after sintering at 900 °C under reducing conditions.

The lattice parameter of the fluorite-type structure is known to vary systematically with the incorporation of actinide or lanthanide cations into the UO_2 matrix. The lattice parameter of the solid solution is expected to change linearly as a function of the composition of the pure end members.

For the binary mixed oxide systems containing U and Ce, the lattice parameter of the solid solution can be related to the mole fraction of the substituting cation according to the empirical relationship reported in the literature by Kleykamp [203]:

$$a(Ce_xU_{1-x}O_2) = 4.7127\ \text{Å} - 0.058\ x \qquad (57)$$

As discussed by Kleykamp [203], the lattice parameter of the solid solution contracts when compared with the pure UO_2 with increasing Ce content. The refined lattice parameters for our coprecipitate solids are in good agreement with the expected behavior for the investigated solid solution. A linear decrease in the cell parameter with Ce content is observed, as shown in Table 9 below.

Table 9: Lattice parameters for the U-Ce solid samples sintered at 900 °C.

Composition	Expected from Eq. (56)	a (Å) refined
$UO_{2.00}$	-	-
$Ce_{0.01}U_{0.99}$	5.4707	5.4709 (1)
$Ce_{0.10}U_{0.90}$	5.4655	5.4660 (1)

5.9.4. XPS results for the U-Ce coprecipitate solid

Surface chemical analysis of the U-Ce oxide solids was performed using X-ray photoelectron spectroscopy (XPS). For the $Ce_{0.01}U_{0.99}$ solid, the Ce concentration was below the instrumental detection limit (~1.0 at.%), and consequently, no detectable features were observed in the Ce 3d spectral region. However, the high-resolution spectrum of the U 4f region (see Fig.48a) exhibits characteristic signals of U(IV), including a U $4f_{7/2}$ peak at approximately 380.5 eV, a spin–orbit splitting of about 10.9 eV between the U $4f_{7/2}$ and U $4f_{5/2}$ components, and the presence of distinct satellite features associated with the U(IV) doublet [204, 205].

The absence of a U $4f_{7/2}$ peak at binding energies ≥ 381.0 eV indicates that higher oxidation states such as U(VI) are absent, confirming that U is predominantly present as U(IV) in the coprecipitated solid sample.

For the $Ce_{0.10}U_{0.90}$ solid, the high-resolution Ce 3d spectrum (see Fig. 47) shows two characteristic spin–orbit doublets corresponding to the $Ce3d_{5/2}$ and $Ce3d_{3/2}$, components, which are consistent with the spectrum of Ce(III) [206].

The U 4f spectrum (see Fig. 48b) similarly shows features indicative of U(IV), with a U $4f_{7/2}$ peak located at approximately 379.5 eV, a spin-orbit splitting of ~10.9 eV, and clearly resolved satellite peaks associated with the U(IV) oxidation state. These results demonstrate that the $Ce_{0.10}$ $U_{0.90}$ solid contains U predominantly in the U(IV) oxidation state together with Ce(III) oxide (Ce_2O_3).

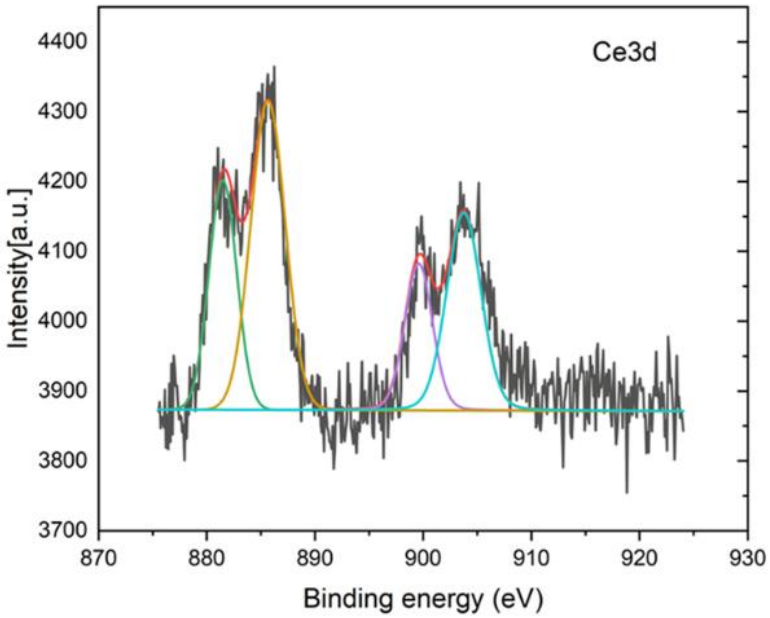

Figure 47: High-resolution XPS scans in the Ce3d for the $Ce_{0.10}U_{0.90}$ solid.

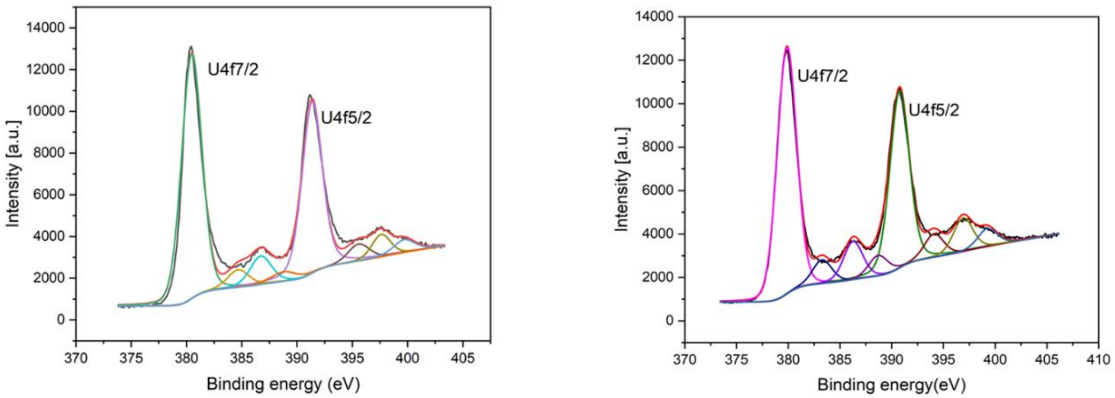

Figure 48. High-resolution XPS scans in the U4f region for the (a)$Ce_{0.01}U_{0.99}$ solid.(b) U4f region for the $Ce_{0.10}U_{0.90}$ solid.

5.10. Equilibrium distribution between the U-Ce solid and aqueous phase

At equilibrium between the solid phase and the aqueous phase, the distribution of elements follows the Berthelot-Nernst homogeneous distribution law as expressed in Eqn. 57. The plot of the normalized concentrations of Ce relative to U concentration has quite some spreads, particularly at the low –log [H^+] range but consistently indicates that the Ce release from the solid matrix is totally controlled by U dissolution and does not vary with time, demonstrating a congruent release mechanism. The corresponding distribution factor was calculated according to the Berthelot–Nernst relationship (McIntire 1963) [207].

$$\frac{[\mathrm{Ce(III)}]_{(s)}}{[\mathrm{U(IV)}]_{(s)}} = \mathrm{D}\frac{[\mathrm{Ce(III)}]_{(aq)}}{[\mathrm{U(IV)}]_{(aq)}} \qquad (58)$$

The D values were calculated for both compositions and resulted in D = 0.05 for the $Ce_{0.01}U_{0.99}$ solid and D = 0.27 for the $Ce_{0.1}U_{0.9}$ solid.

5.11. Kinetics of solubility equilibria for the U-Ce coprecipitated solids

The evolution of the U-Ce concentrations in solutions as a function of equilibration time was studied to determine whether the system reached equilibrium during solubility experiments. As shown in Fig. 49 , the total concentrations of U and Ce in contact with the coprecipitated solids remain very similar after 7, 14, 21, and 30 days. Only a slight decrease in concentration over time is observed, which is likely due to the aging of the initially amorphous solid phase.

The observed decrease in concentrations agrees with the typical behavior of amorphous solids, where aging can lower the solubility. Therefore, it can be expected that even longer equilibration times would lead to a more noticeable decrease in the measured concentrations. Similar observations have been reported in previous studies on amorphous UO_2-based coprecipitates. For instance, Bruno and Sandino [121] observed steady-state U concentrations after ~ 50 hours of contact with the solid phase, while Rai and coworkers [201] also reported that equilibrium in comparable systems is typically achieved within about three days. Consistent with these literature reports, the results from this study indicate that equilibrium between the solution and the freshly precipitated solids was attained during the experiments. However, at longer equilibration times,

the initially amorphous coprecipitates are expected to gradually transform into more crystalline phases, which would result in lower solubilities.

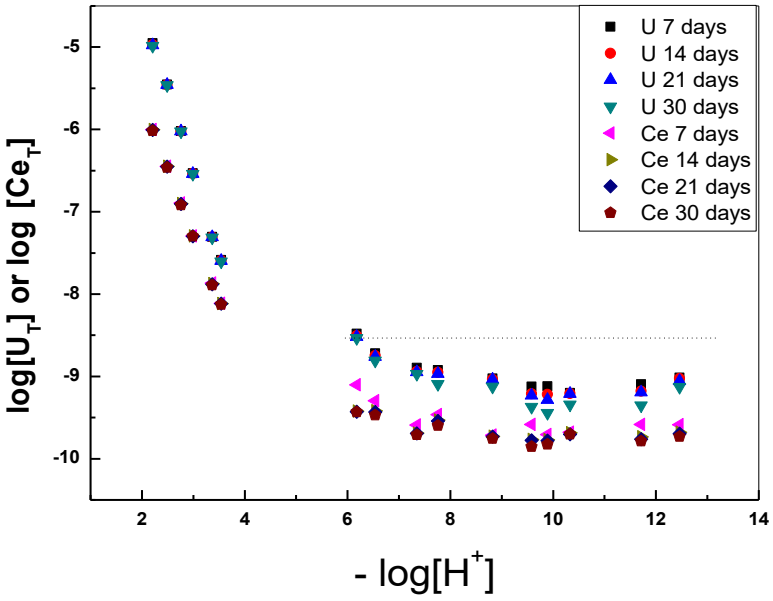

Figure 49. Evolution of total U and Ce concentrations during 30 days of equilibration across the investigated pH range for the solid containing 1% Ce.

5.12. U-Pu-Np coprecipitation results (paper IV)

To better understand the behaviour of SNF observed during leaching test in the presence of H_2 and to investigate the potential formation of actinide oxide solid solutions of (U, Pu, and Np) as well as the nature of the resulting solid phases formed, precipitation experiments were conducted in aqueous solution (0.01 M NaCl) representative of repository conditions. Both aqueous and solid-phase characterization data were evaluated, and the results are discussed below.

5.12.1 Characterization of the U-Pu-Np solid phase

5.12.2 Total chemical analysis for the U-Pu-Np coprecipitate solids

The total molar ratios of U, Pu, and Np were determined for solid samples before and after equilibration. A few mg of the solids were dissolved in 2 M HNO_3 and analyzed by ICP-MS to determine their respective compositions. The composition of the solid phase after 126 days at equilibrium with a solution at pH 8.5 was quite similar to the solid before equilibration, as shown in Table 9. The analysis was also carried out for 30 days with similar results to the 126 days. For the samples with a higher concentration of Pu (5 mol %), the analysis was carried out after 30 and 95 days of equilibration, with both showing similar results.

The longer equilibration period for the set of solid samples was chosen in analogy to Rai and coworkers [201], who reported solid analysis for a longer equilibration period of 238 days against the solubility data reported for 38 days.

Table 9: Analytical molar fractions of U and Ce in the initial and equilibrated solids.

Target composition	Before equilibration			After equilibration		
$Pu_xNp_yU_{1-x-y}$	Pu	Np	U	Pu	Np	U
$Pu_{0.01}Np_{0.001}U_{0.989}$	0.01	0.001	0.989	0.01	0.001	0.989
$Pu_{0.05}Np_{0.005}U_{0.945}$	0.05	0.005	0.944	0.05	0.005	0.944

5.12.3. SEM-EDX/WDS results for the U-Pu-Np coprecipitate solids

The U–Pu–Np coprecipitates solid samples were characterized before and after equilibration using SEM in secondary electron imaging mode. The obtained micrographs (see Figs. 50 and 51) show a uniform surface microstructure without observable compositional contrasts. No distinct phases or segregated regions enriched in U or Pu were detected, which suggests a homogeneous distribution of the elements within the solid material.

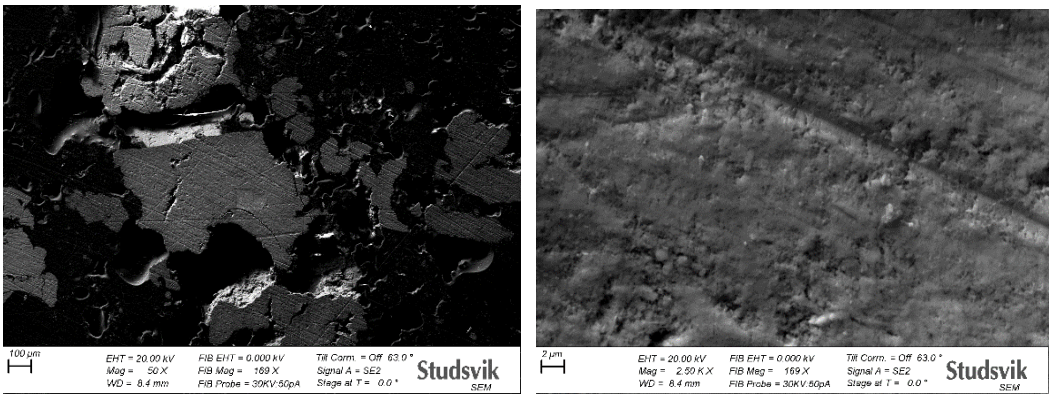

Figure 50: SEM micrographs of the solid samples ($U_{0.945}Pu_{0.05}Np_{0.005}$) before equilibration at different magnifications.

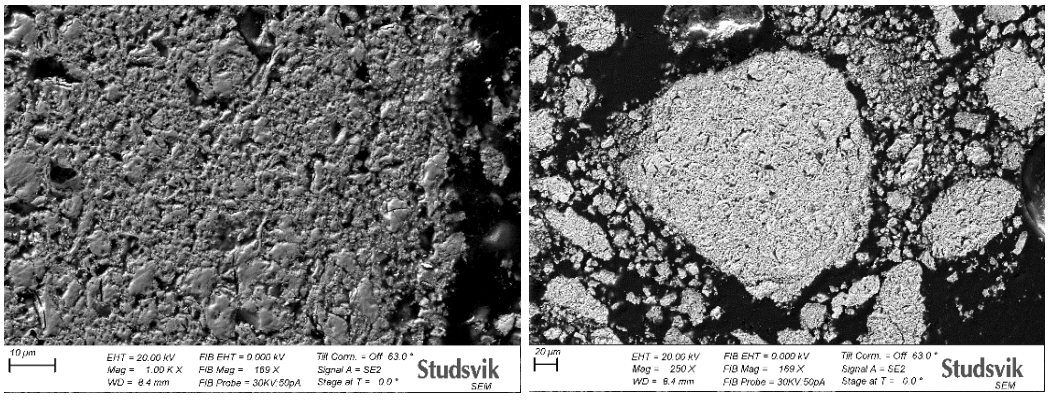

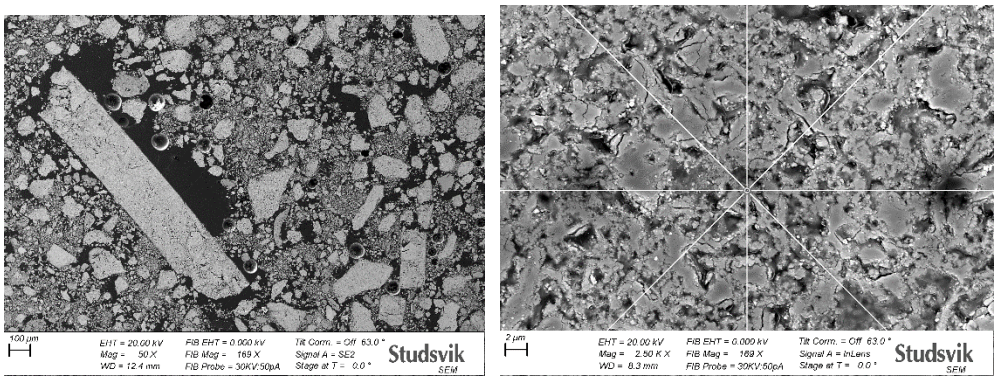

Figure 51: SEM micrographs of the solid samples ($U_{0.945}Pu_{0.05}$ $Np_{0.005}$) after equilibration at different magnifications.

SEM-EDX analysis of the solid samples before and after equilibration (see Figs. 52 and 54) confirms the presence of U, Pu, and Np in the sample. EDX and WDS elemental mapping analysis of the solids (see Figs. 53 and 55 for only EDX) indicate that U, Pu, and Np are uniformly distributed within the solid samples. A scan in several different areas or spots showed a homogeneous distribution of U, Pu, and Np.

For the sample containing $Pu_{0.01}Np_{0.001}U_{0.989}$, the Pu and Np concentrations were below the detection limit of the EDX/WDS analyses. The absence of compositional heterogeneity suggests that the solid samples consist of a single phase rather than a mixture of distinct solid phases. The uniform elemental distribution observed in the EDX mappings supports the interpretation that the solids form a solid solution. Furthermore, no additional phases were detected after equilibration, and the homogeneous distribution of U, Pu, and Np remained unchanged (see Figs. 52 and 54). These findings are also supported by the EDX and WDS line scan analysis carried out on the solid samples (see Fig. 56 for only WDS), which also confirms the uniform distribution of Pu and U in the coprecipitated solid samples. However, the instrument is limited in the detection of Np, but very useful in distinguishing between the U and Pu peaks.

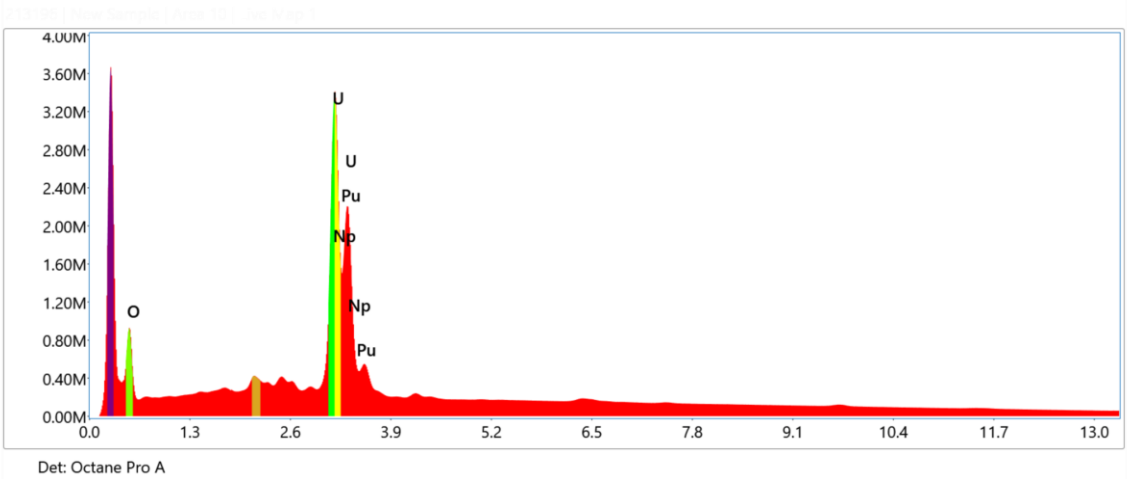

Figure 52: SEM-EDX spectrum of the solid samples ($U_{0.945}Pu_{0.05}$ $Np_{0.005}$) before equilibration.

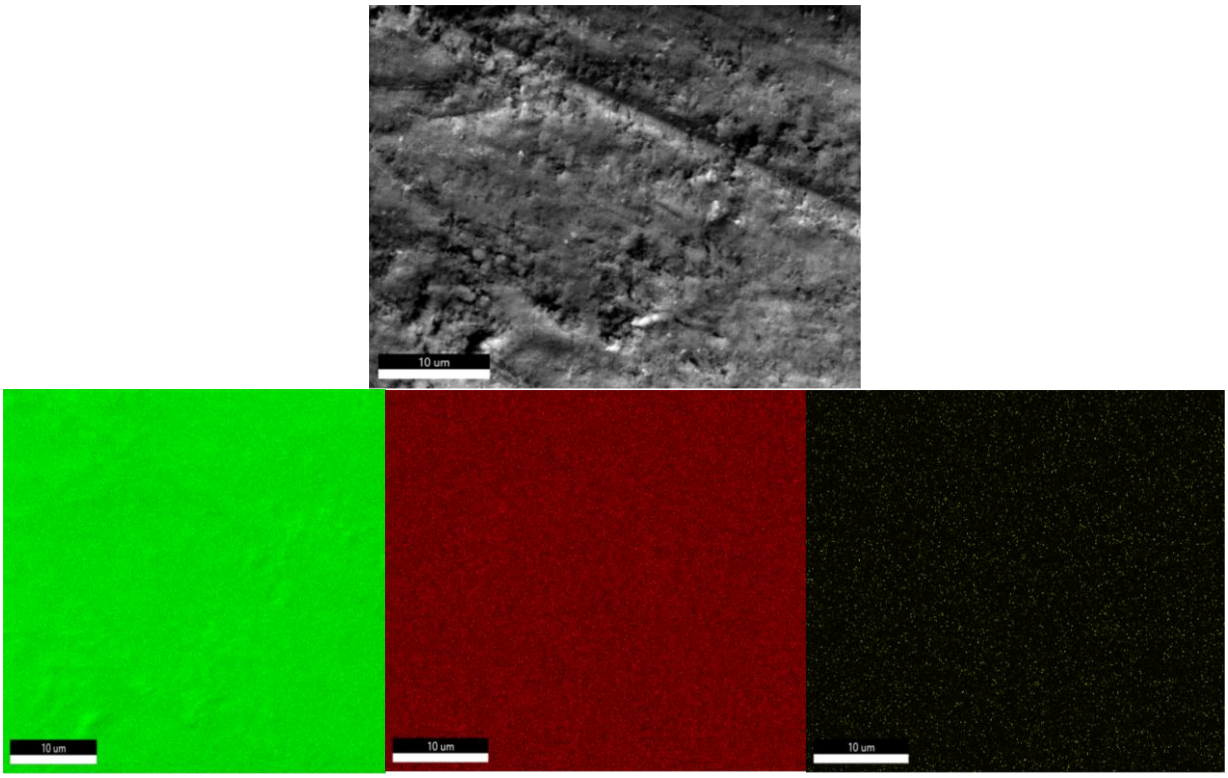

Figure 53: Micrograph and EDX mapping (left-U, center Pu, right-Np) of the solid sample (U $U_{0.945}Pu_{0.05}$ $Np_{0.005}$) before equilibration.

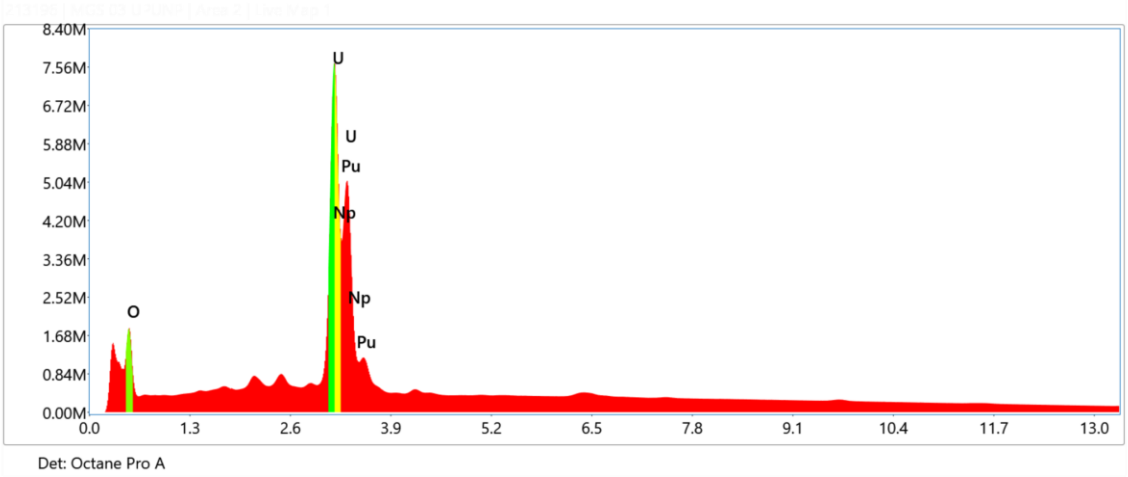

Figure 54: SEM-EDX spectrum of solid samples ($U_{0.945}Pu_{0.05}$ $Np_{0.005}$) after equilibration.

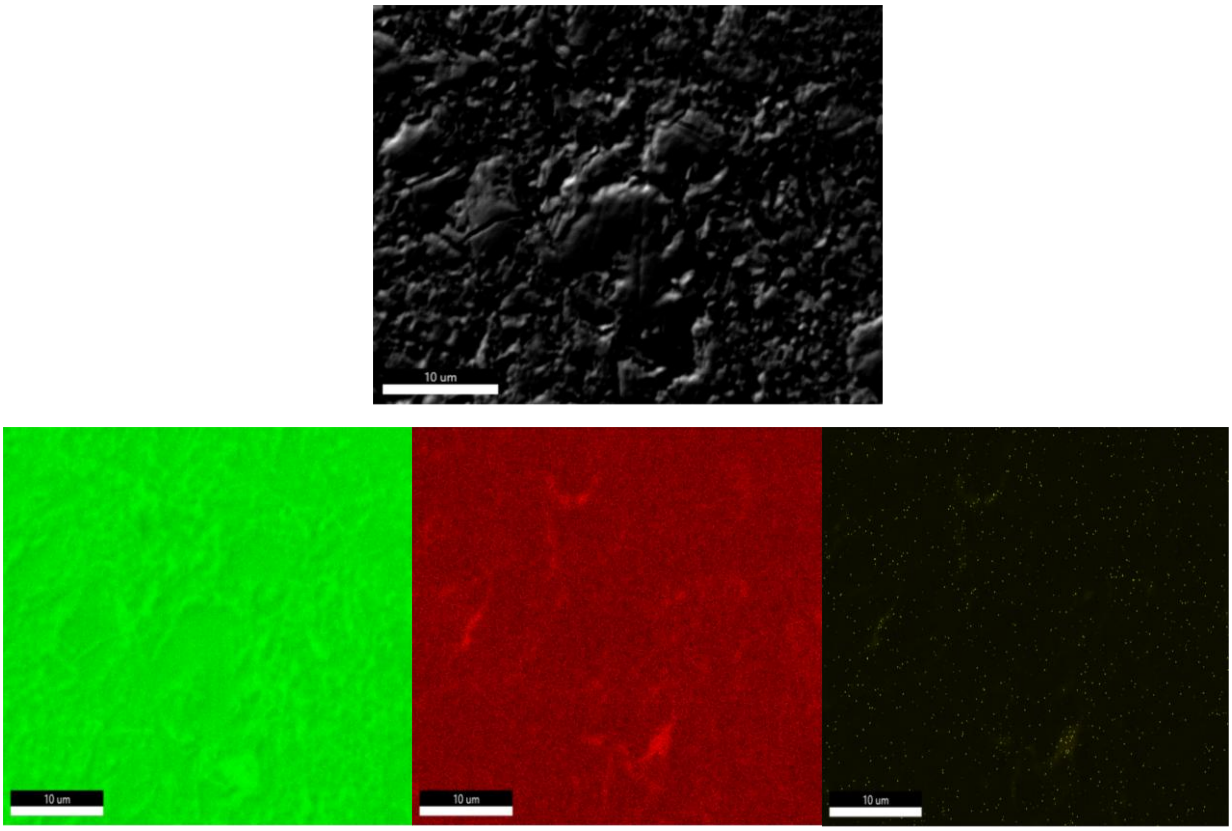

Figure 55: Micrograph and EDX mapping (left-U, center Pu, right-Np) of the solid sample ($U_{0.945}Pu_{0.05}$ $Np_{0.005}$) after equilibration.

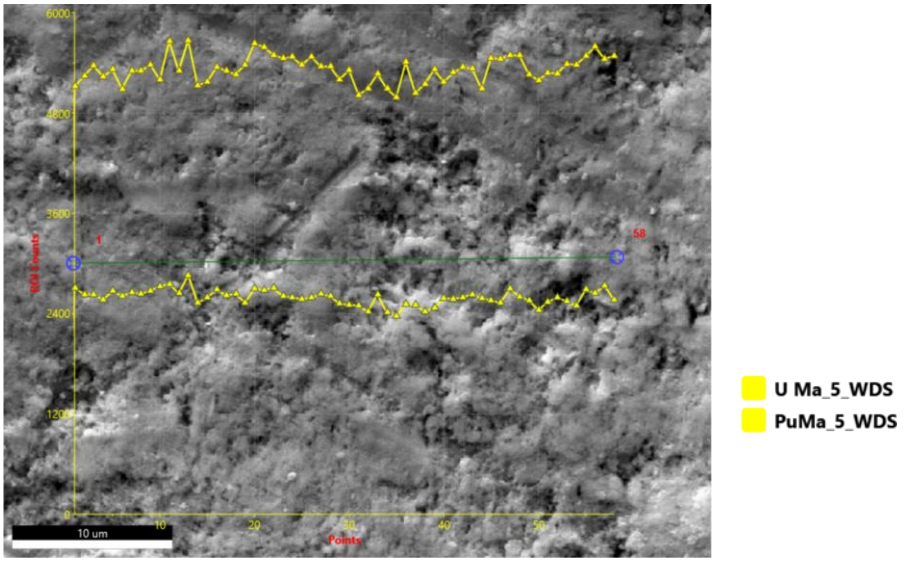

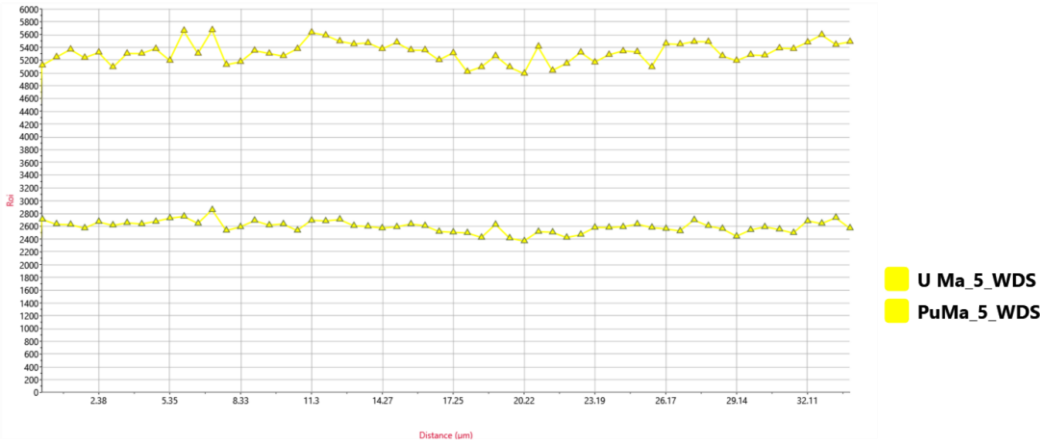

Figure 56: WDS Line scan of the solid samples ($U_{0.945}Pu_{0.05}$ $Np_{0.005}$) before equilibration

5.12.4. High-resolution XRD results for the U-Pu-Np coprecipitate solids

The diffraction peaks of the solids before and after equilibration were similar in appearance. The representative samples show broad peaks and not well-defined peaks. Peak indexing was carried out using crystallographic data obtained from the Inorganic Crystal Structure Database (ICSD). Phase identification and indexing were performed with GSAS-II, while structural refinement was conducted using the ICSD entry with collection code 246854 as the initial model for the refinement procedure. The solid precipitate peaks indicate that the solids are mainly amorphous, and the presence of microcrystallinity cannot be ruled out.

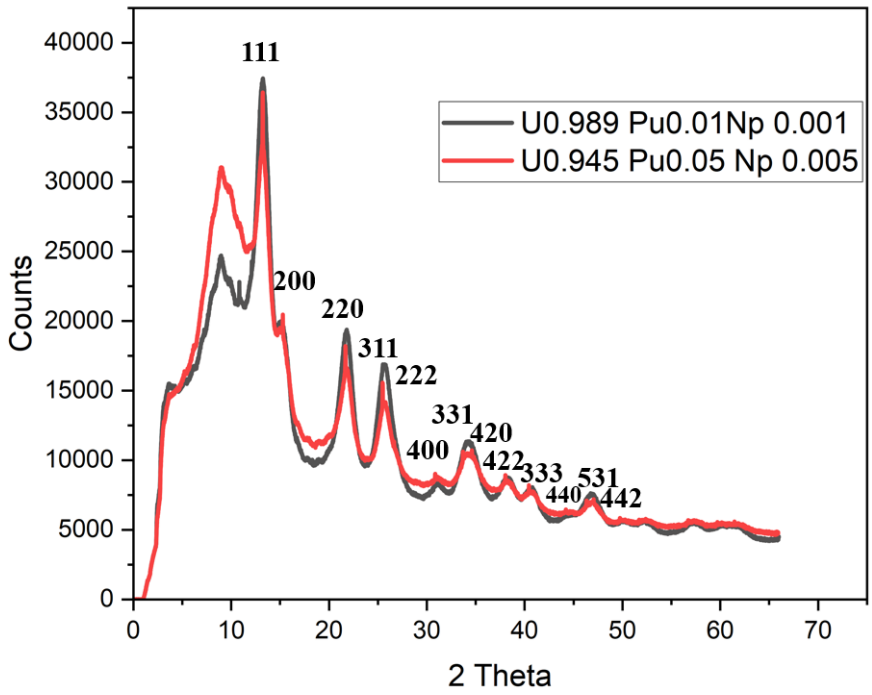

Figure 57. XRD spectra of the $U_{0.989}$ $Pu_{0.01}$ Np $_{0.001}$ solid (black) and $U_{0.945}Pu_{0.05}$ $Np_{0.005}$ (red). Both after equilibration of the solid.

The samples sintered at 900 °C under reducing atmosphere had well-defined crystalline narrow peaks for both samples, as shown in Figs.58 and 59.

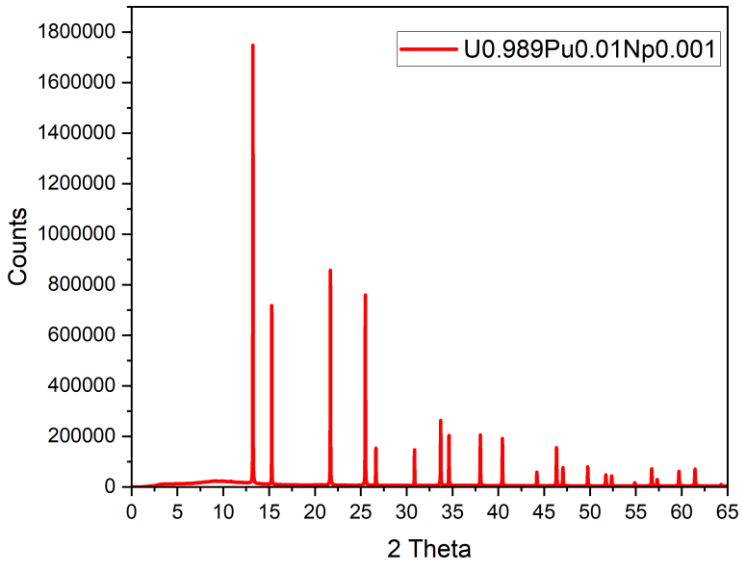

Figure 58. XRD pattern of the equilibrated $U_{0.989}Pu_{0.01}Np_{0.001}$ solid heated at 900 ˚C under reducing conditions.

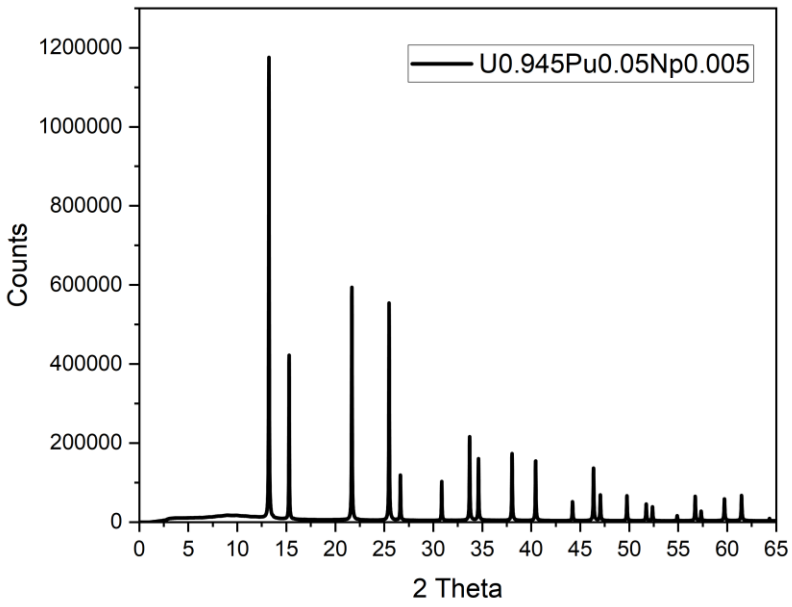

Figure 59. XRD pattern of equilibrated $U_{0.945}Pu_{0.05}Np_{0.005}$ solid heated at 900 °C under reducing conditions.

The behavior of solid solution structures can be investigated using diffraction methods. The lattice parameter of mixed actinide oxides is a critical structural property that reflects the degree of substitution of cations in the fluorite lattice. The lattice parameter of the mixed oxide was refined using the GSAS-II software [202] and is reported in Table 10. The lattice parameter of $U_{1-x-y}Pu_xNp_yO_{2\pm x\pm y}$ solid solution is expected to change linearly as a function of the composition of the pure end members. For the ternary U–Pu–Np system, the lattice parameter can be expressed as the mole-fraction weighted average of the end-member lattice parameters. Vegard's law extends to ternary systems like:

$$a(U_{1-x-y}Pu_xNp_yO_2) = (1-x-y)a_{UO_2} + xa_{PuO_2} + ya_{NpO_2} \quad (59)$$

where x_i represents the mole fraction of the cation i and a_i is the lattice parameter of the corresponding pure oxide. The following lattice parameters have been reported in previous studies: $UO_{2.00}$ is 5.47127 Å , $PuO_{2.00}$ is 5.3960 Å and NpO_2 as 5.434 Å [208-210]. The refined lattice parameters for the investigated coprecipitates are shown below.

Table 10. Lattice parameters for the U-Pu-Np solid samples sintered at 900 °C.

Composition	Expected from Eq. (58)	a (Å) refined
$UO_{2.00}$	-	-
$Np_{0.001}Pu_{0.01}U_{0.989}$	5.4704	5.4691 (1)
$Np_{0.005}Pu_{0.05}U_{0.945}$	5.4673	5.4669 (1)

As seen from Table 10, the refined lattice parameters for our annealed coprecipitate solid samples are quite similar to the values calculated with the extended Vegard's law. However, the ratio O/M was not investigated in this study. A face-centered cubic structure was observed for both the $Np_{0.001}Pu_{0.01}U_{0.989}$ sample and the $Np_{0.005}Pu_{0.05}U_{0.945}$ samples. An increase in the Pu and Np content in the solid solution would lead to contraction of the solid solution lattice parameter when compared to pure UO_2. This trend confirms the successful incorporation of these cations into the UO_2 lattice and supports the formation of homogeneous solid solutions or mixed oxides. The refinement data support the formation of fluorite-type solid solutions in the U–Pu–Np system.

5.12.5. XANES result from the U-Pu-Np coprecipitate solids

XANES spectra are typically divided into three distinct regions: the pre-edge, the absorption edge (including the white line), and post-edge features. The spectra presented in Fig.60 have been collected at the Pu L_3 edge for PuO_2 (red reference spectrum) and two UO_2-based samples doped with varying concentrations of Pu and Np, namely $U_{0.989}Pu_{0.01}Np_{0.001}$ (green) and $U_{0.945}Pu_{0.05}Np_{0.005}$ (blue). The position of the absorption edge and, in particular, the white line serve as a reliable indicator or sensitive probe of the oxidation state of Pu [211].In the present study, the excellent agreement between the white line of PuO_2 and that of UO_2 doped with Pu confirms that Pu is present in the tetravalent state (Pu(IV)) in all the investigated materials. To support the experimental XANES observations, theoretical spectra were calculated using the FEFF10 code based on multiple scattering theory. The simulations, performed for both PuO_2 and Pu substituted into the UO_2 lattice, show excellent agreement with the experimental data, validating the structural interpretation. This analysis confirms that the local coordination environment of Pu in UO_2 doped with Pu differs from that in pure PuO_2. Specifically, the Pu–O

bond distances in the doped UO_2 are longer (~2.36 Å) than in PuO_2 (~2.33 Å). The lattice parameter has decreased from 5.46 Å (in case of UO_2) to 5.39 Å. This effect is observable at the lowest doping concentration of 1% Pu in UO_2. As the doping concentration increases to 5%, the local structure around Pu becomes increasingly similar to that of PuO_2, indicating that higher Pu concentrations restore a coordination environment closer to the reference PuO_2 structure.

Similar results have been previously reported by P.Martin and coworkers [208]. This observation confirms that Pu has been successfully incorporated into the UO_2 structure, occupying lattice sites within the fluorite framework.

The local coordination environment around Pu closely resembles that of U in UO_2, indicating that the dopant atoms substitute into the U host lattice without forming separate or distinct PuO_2 phases at lower Pu concentrations. Such incorporation also suggests that the overall crystal structure remains stable and maintains its integrity even at low to moderate Pu doping levels. The XANES results confirm that Pu is present in the tetravalent state Pu(IV) in all investigated solid samples, including both precipitated solids and thermally treated solid samples.

However, prior to the coprecipitation experiment, we confirmed using UV–Vis that Pu was present in the acidic solution in the +3 oxidation state. Two scenarios may explain the observations. Either Pu(III) is unstable under alkaline conditions and is oxidized to Pu(IV), which subsequently coprecipitates with U(IV) and Np(IV), or Pu(III) was initially incorporated into the freshly precipitated solid and later oxidized to Pu(IV) during extended storage in the glove box (~ 8 months between precipitation and XANES analysis), or during sample preparation, transport, or during measurement.

To our knowledge, the only reported case of a U(IV)–Pu(III) coprecipitate is an early study (Bruno and Sandino, [121]), where the presence of Pu(III) was based on reduction of Pu(IV) in acidic solution by U(IV), but no analysis of the oxidation state was carried out. Several studies related to synthesis of U-Pu fuels have reported coprecipitation of U(IV) and Pu(III) oxalates (Arab-Chapelet and coworkers [212, 213], Grandjean and coworkers [214]), but Pu is converted to Pu(IV) in the oxide obtained during sintering of oxalates at high temperature under Ar atmosphere. In spite of sintering under H_2 atmosphere, we could expect this to happen for our two high temperature samples, but not for the as precipitated ones, which are the main objective of the study.

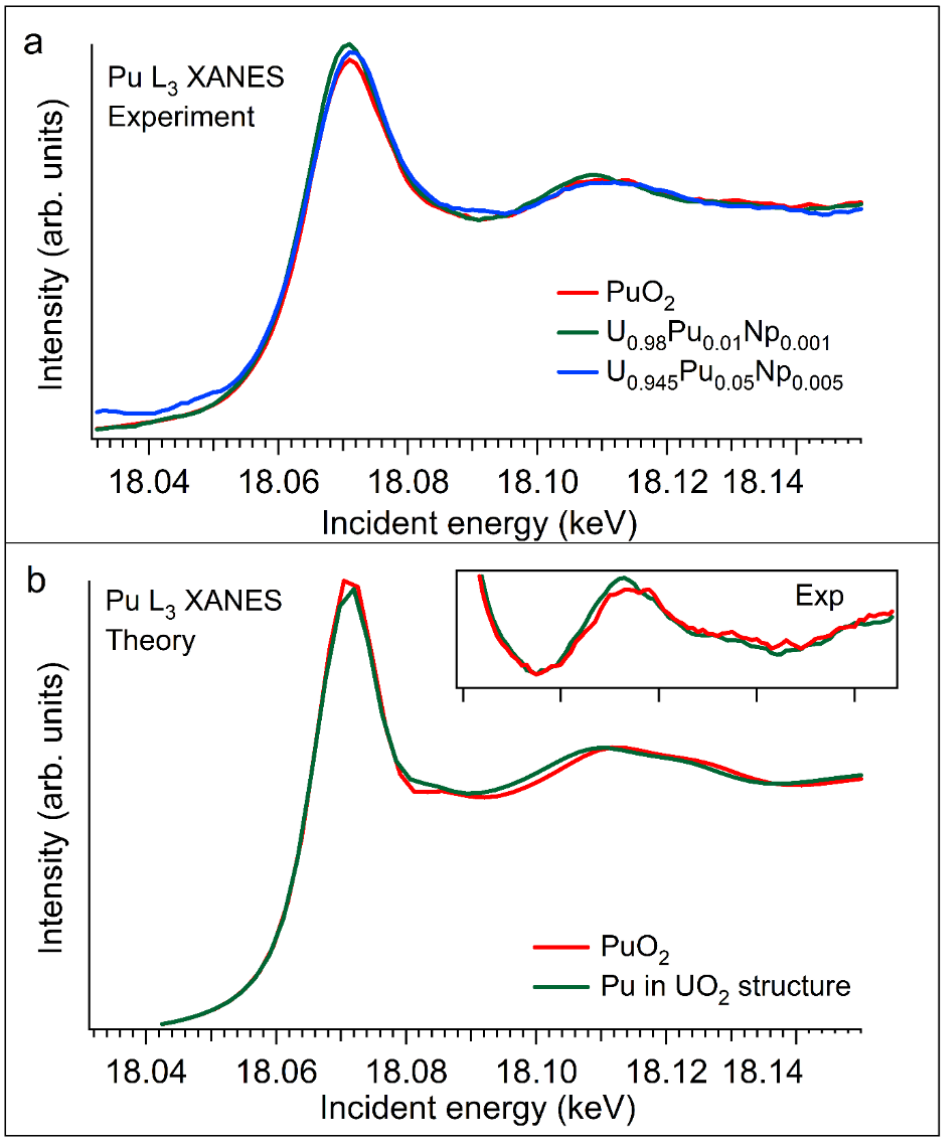

Figure 60. (a) Experimental XANES spectra recorded at the Pu L_3 edge for PuO_2 (red), $U_{0.98}Pu_{0.01}Np_{0.001}$ (green) and $U_{0.945}Pu_{0.05}Np_{0.005}$ (blue) (b) Theoretical XANES spectra calculated using the FEFF code for PuO_2 and UO_2 doped with Pu structure.

According to Grenthe and coworkers [16] and Cho and coworkers [215], Pu(OH)3(s) is stable within the water stability field. It has also been used as a precursor for $Pu(OH)CO_3$(s) synthesis and solubility studies (Müller and coworkers [216]), where Pu(III) in the solid was confirmed by dissolving it in HCl and identifying Pu(III) by UV–Vis.

This approach is not applicable here in this present study, as dissolved uranium would reduce Pu(IV) to Pu(III) in acidic solution, preventing the identification of Pu(III) in the solid. Our coprecipitates are very fine powders and appear highly sensitive to oxidation. A similar U–Ce coprecipitation study in previous work by Saleh and coworkers [217] showed U(VI) by EXAFS but U(IV) by XPS.

In this study, XRD shows a cubic UO_2 structure, indicating no major oxidation. Pu appears as Pu(IV) in all samples. Due to limited resources, no XANES for U or XPS analysis was performed. Since both SEM-EDX and XANES indicate homogeneous Pu distribution, an ideal solid solution with UO_2 was assumed. Under reducing conditions, Pu(IV) is expected to dissolve as Pu(III). To account for possible oxidation of the sample after precipitation, solubility data were evaluated assuming both Pu(IV) and Pu(III) in the solid.

5.13. Characterisation of the U-Pu-Np liquid phase

5.13.1. U concentrations in equilibrium with the $Np_{0.001}Pu_{0.01}U_{0.989}$ co-precipitate solid

The behaviour of U in equilibrium with $Np_{0.001}Pu_{0.01}U_{0.989}$ co-precipitated solid is expected to closely resemble that of amorphous UO_2(am), as the low Pu-Np content is not anticipated to significantly alter the UO_2(am) solubility. As shown in Fig. 61, the measured U concentrations after 30 days are in good agreement with literature solubility data for UO_2(am) in 0.01 M NaCl solution [196, 197].

In the acidic pH region of 2–4, U concentrations decrease by approximately three orders of magnitude per unit increase in pH, consistent with the reported behaviour observed in the U-Ce study. Within this pH range, U(IV) speciation is dominated by the formation of the first hydrolysis species, $U(OH)^{3+}$, as consistently reported in studies on the solubility of amorphous UO_2. Accordingly, the equilibrium between UO_2(am) and the aqueous phase in this region is primarily governed by the following reaction:

$$UO_2(am) + 3\ H^+ \rightleftharpoons U(OH)^{3+} + H_2O(l) \qquad (60)$$

$$*K^0_{s3} = \{U(OH)^{3+}\}\ a_w\ \{H^+\}^{-3} \qquad (61)$$

At higher pH values > 4, the measured U concentrations agree well with the lower solubility limit reported for UO_2(am), with log[U] = – 8.5 ± 1 [16]. These values are also consistent with U concentrations observed in spent nuclear fuel leaching studies under similar conditions [18, 207, 208]. No direct determination of the oxidation states of U, Np, or Pu was performed at these low concentrations. However, the measured U concentrations are among the lowest reported for UO2(am) under similar experimental conditions, which strongly suggests the absence of U(VI). Assuming that U remains reduced, it is reasonable to infer that Pu and Np are likewise not oxidized under the same conditions.

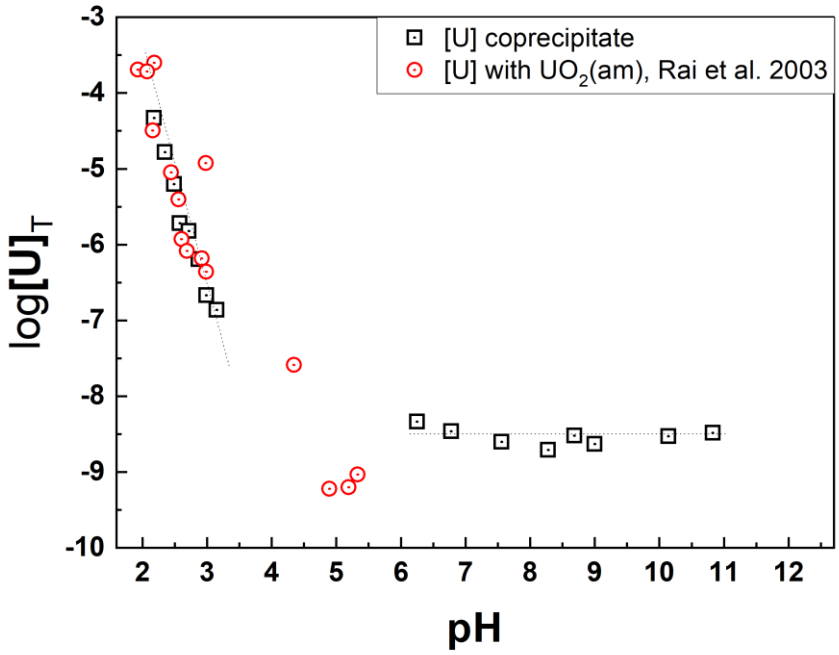

Figure 61. Concentrations of U in equilibrium with the $Np_{0.001}Pu_{0.01}U_{0.989}$ solid solution at 30 days. The dotted line with slope -3 is from Fig. 4 in (Rai and coworkers [197]), while the horizontal dotted line indicates log[U] = -8.5.

5.13.2. Np and Pu concentrations in equilibrium with the co-precipitate solid ($Np_{0.001}Pu_{0.01}U_{0.989}$ and $Np_{0.005}Pu_{0.05}U_{0.945}$)

For the U-Pu-Np-containing solids, the measured Np concentrations are about three orders of magnitude lower than the solubility of pure NpO_2(am). Previous studies by Rai and coworkers [201] have indicated that both U(IV) and Np(IV) form ideal solid solutions. In such solids, the solubility of the minor component is proportional to its mole fraction in the solid. Our results confirm this, with the expectation that the solubility of Np from the co-precipitate is directly proportional to its mole fraction in the solid phase i.e. $0.001K_s^0$ or $0.005K_s^0$, where K_s^0 is the solubility product of NpO_2(am, hydr).

XANES analysis indicates that Pu is present in the +IV oxidation state in the solid phase. However, it cannot be determined whether Pu(III), initially introduced before precipitation, was oxidized to Pu(IV) during the precipitation process or at a later stage, such as during storage in the glove box, sample handling, transport, or exposure to the accelerator beam. For the interpretation of the solution data, it is therefore first assumed that Pu is present as Pu(IV) in the solid phase under the conditions of the equilibration experiments with groundwater and dithionite. Under this assumption, it is reasonable to consider that U(IV), Np(IV), and Pu(IV) can form an ideal solid solution due to their similar chemical properties and ionic radii.

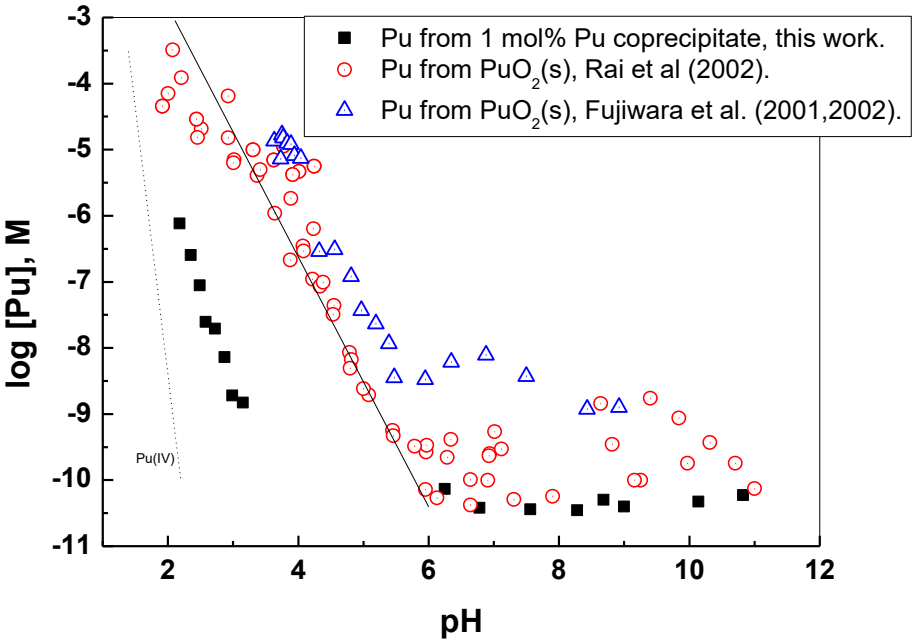

Figure 62. Concentrations of Pu in equilibrium with 1 mol% Pu coprecipitate and with pure PuO_2(am, hydr) from the data of Rai and coworkers [189] and Fujiwara and coworkers [218, 219]. Datasets in tables A.1 and A.II for 4 to 43 days equilibration from under and oversaturation [189] and 3 months equilibration data [218]. Lines from Fig. 1 in [189].

In this case, equilibrium Pu concentrations should correspond to $0.01K_s^0$ or $0.05K_s^0$ where Ks^0 is the solubility product of PuO_2(am,hyd).Fig. 63 compares the $Np_{0.001}Pu_{0.01}$ $U_{0.989}$ data with literature studies on reductive dissolution of PuO_2(am, hydr) in the presence of Fe(II) (Rai and coworkers [189] and dithionite (Fujiwara and coworkers [218, 219]). These studies show that PuO_2 (am, hydr) dissolves reductively, releasing Pu(III) into solution.

$$PuO_2(am, hyd) + 4\ H^+ + e^- \rightleftharpoons Pu^{3+} + 2\ H_2O \qquad (62)$$

The Pu concentrations from the coprecipitate (see Fig.63) are much higher than Pu(IV) concentrations measured in equilibrium with PuO_2(s) [189] but lower than values reported for reductive dissolution of PuO_2 (am, hydr). The difference is most pronounced in the acidic range, where concentrations are 2–4 orders of magnitude lower. In neutral to alkaline conditions, they are about 0.5–1 order of magnitude lower than data from Rai and coworkers [189]. Data from [218] in the alkaline range are excluded due to colloid formation during their oversaturation solubility study. For the 5 mol% Pu coprecipitate (Fig. 64), Pu concentrations are slightly higher than for 1 mol% in the acidic range and about $10^{-9.5}$ M in the neutral to alkaline pH range. Pu(IV) may dissolve reductively under acidic conditions, while in neutral to alkaline conditions, it may be released as Pu(IV). Rai and coworkers [189] attribute low and scattered Pu concentrations at high pH to low PuO_2 solubility, detection limits, and possible redox changes,

In this study, SEM-EDX-WDS and XANES confirm homogeneous Pu distribution in the UO_2 matrix. However, measured total Pu concentrations (~$10^{-10.5}$ M for 1 mol% and ~$10^{-9.5}$ M for 5 mol% at pH > 6) are significantly higher than expected for an ideal U(IV)–Pu(IV) solid solution

($\approx 10^{-12.4}$ M). This indicates that the observed concentrations cannot be explained solely by equilibrium with a homogeneous U(IV)–Pu(IV) coprecipitate. The observed differences (2.1-3.6 orders of magnitude decrease in acidic range and <1 order in neutral to alkaline range) deviate from ideal behaviour, suggesting the coprecipitate's solid is non-ideal. This supports the assumption that Pu was initially present as Pu(III) in the solid. Any conversion to Pu(IV) likely occurred during storage, sample handling, or XANES analysis. Therefore, the solubility data were also evaluated assuming Pu(III) in the coprecipitate.

5.13. 3. Pu(III) concentrations in equilibrium with the co-precipitate solid ($Np_{0.001}Pu_{0.01}U_{0.989}$ and $Np_{0.005}Pu_{0.05}U_{0.945}$)

In this section, we consider that Pu is present as Pu(III) in the co-precipitated solids. The measured Pu(III) concentrations in equilibrium with the $Pu_{0.01}Np_{0.001}U_{0.989}$ co-precipitate are approximately 1.7-2 orders of magnitude lower than those of U across the entire investigated pH interval.For each chemical component in the system UO_2 xH_2O(s)-Pu $(OH)_4$(s)-H_2O at equilibrium the chemical potential (μ) must be equal in the solid and in the aqueous phase μ^s (Pu $(OH)_3$) = μ^{aq} (Pu$(OH)_3$). The thermodynamic model follows the same approach described for the U–Ce coprecipitation system. In the acidic region (pH 2.1–3.2), where Pu^{3+} is the dominant aqueous species, the dissolution of $Pu(OH)_3$(s) can be represented as:

$$Pu(OH)_3(s) + 3H^+ \rightleftharpoons Pu^{3+} + 3\ H_2O(l) \qquad (63)$$

Within this pH range, the formation of hydrolyzed Pu(III) complexes is not expected to exist. By considering the thermodynamic equilibrium constant ($^*K^0_{s0}$) , concentration of Pu in equilibrium with the co-precipitates and the activity of water in 0.01 M NaCl (which is close to one), we have the following expression:

$$\log \{Pu^{3+}\} = \log\ ^*K^0_{s0} - 3\,pH + \log\ a_{Pu(OH)_3(s)} \qquad (64)$$

Following the same formulation as for the U-Ce system, a composition-dependent constant K_x is introduced to account for the activity of $Pu(OH)_3$(s) in the solid solution:

$$\log [Pu^{3+}] = \log\ K_x - 3\,pH \qquad (65)$$

This relationship allows the determination of K_x by fitting the experimental log $\{Pu^{3+}\}$ data in the acidic region to a line of -3 slope and extrapolating to pH=0. The activities of Pu(III) were calculated from total concentrations using the Specific Ion Interaction Theory (SIT) ($\varepsilon(Pu^{3+}, Cl^-)$) with interaction parameters taken from Grenthe and coworkers [16].

Table 11. Values of log K_x, $a_{Pu(OH)_3(s)}$ and $\lambda_{Pu(OH)_3(s)}$ estimated from data in the pH range 2.1-3.2.

$X_{Pu(OH)_3(s)}$	log K_x	log $a_{Pu(OH)_3(s)}$	log $\lambda_{Pu(OH)_3(s)}$
1	14.6	0.00	0.00
0.05	0.7	-13.9	-12.6
0.01	0.5	-14.1	-12.1

The resulting $K_x$values are approximately 14 orders of magnitude lower than those reported for pure $Pu(OH)_3$(s) in a pH range where $Pu(OH)_3$(s) exists (Felmy and coworkers, Cho and coworkers, [215, 220].

The activity of $Pu(OH)_3(s)$ in the solid phase was determined by subtracting the value of log $*K_{s0}$ (14.6) from the corresponding log K_x values (see Eq. 63). The calculated equilibrium activities are summarized in Table 11. The activity coefficients of $Pu(OH)_3$ in the co-precipitate (λ) were obtained from the relationship between activity and composition, expressed as:

$$a_{Pu(OH)_3(s)} = x\,\lambda_{Pu(OH)_3(s)} \qquad (66)$$

As shown in Table 11, the K_x values exhibit a slight increase with increasing mole fraction x, indicating behavior consistent with solid solution thermodynamics. For all investigated compositions, the equilibrium concentrations of Pu remain consistently lower than those of uranium across the entire pH range.

The determination of the conditional solubility product of $Pu(OH)_3(s)$ from co-precipitate systems within a pH range where the pure solid phase $Pu(OH)_3(s)$ cannot exist is associated with significant uncertainty, therefore, these data should be treated with caution.

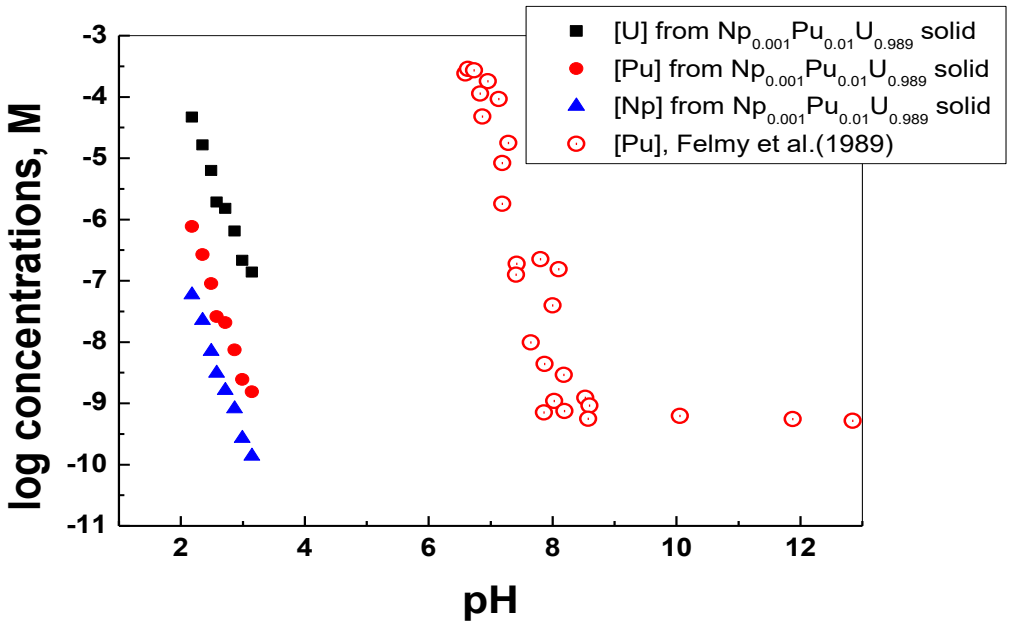

Figure 63. Concentrations of Np, Pu and U in equilibrium with $Np_{0.001}Pu_{0.01}U_{0.989}$ oxide co-precipitate at the acidic pH range compared with concentrations of Pu in equilibrium with Pu $(OH)_3(s)$ (Felmy and coworkers [220]) in distilled water.

For pH values above 9, if $Pu(OH)_3(aq)$ is assumed to be the dominant aqueous species, the total dissolved Pu concentration can be expressed as :

$$\log [Pu]_T = \log *K^0_{s0} + \log *\beta_3 \qquad (67)$$

where $*\beta_3$ is the constant corresponding to the equilibrium reaction:

$$Pu^{3+} + 3\,H_2O(l) \rightleftharpoons Pu(OH)_3(aq) + 3\,H^+ \qquad (68)$$

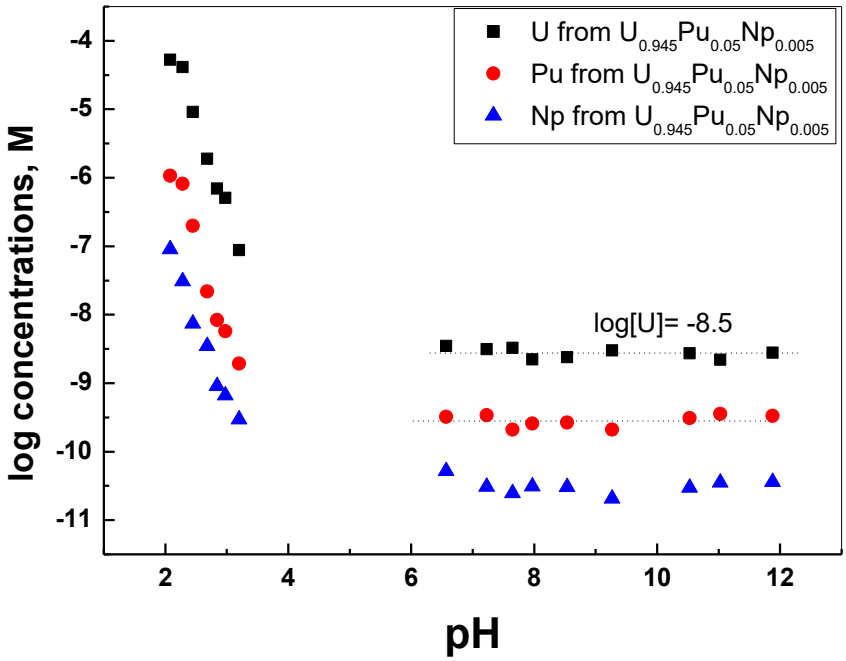

Figure 64. Concentrations of Pu, Np and U in equilibrium with $Pu_{0.05}Np_{0.005}U_{0.945}$ oxide co-precipitate. The dotted lines in the basic range indicate the solubility of UO_2(s), log[U] = - 8.5 and the horizontal part of Pu concentrations for the pure oxide and the coprecipitate.

The concentrations of Pu in equilibrium with UO_2-based co-coprecipitates are expected to be lower than those in equilibrium with pure $Pu(OH)_3$(s), due to the activity of $Pu(OH)_3$(s) within the solid solution. Under these conditions, the dissolved Pu concentration can be expressed as:

$$\log [Pu] = \log K_x + \log {}^*\beta_3 \quad (69)$$

There is no published data of $^*\beta_3$ for $Pu(OH)_3$(aq), only estimations mainly based on analogies with Am(III) systems exist and its corresponding solubility product [221-223]. However, as discussed by Grenthe and coworkers [16] based on the work of Cho and coworkers [218], Pu(III) exhibits stronger hydrolysis behaviour than Am(III) and, along with the solubility product, which is more than one order of magnitude lower.

In the present study, an approximate value of log $^*\beta_3$= -23.6. was derived by combining experimental data from Felmy and coworkers [220], which report log $[Pu]_T \sim -9$ in the pH range 9-12, and the constant $^*K_{s,3}$ =-9.3 for $Am(OH)_3$(am) (Guillaumont and coworkers [172], and with the value $^*K_{s0}$= 14.6 from [218]. Using this estimate, the composition -dependent constants (log $K_{0.01}$ and log $K_{0.05}$) were determined from Pu concentrations measured at high pH in equilibrium with the corresponding solids.

As illustrated in Fig. 64, Pu concentration at pH > 9 is completely determined by congruent dissolution with UO_2(s), showing a constant decrease relative to U concentrations. The corresponding $K_x$values, along with the calculated activities and activity coefficients λ of $Pu(OH)_3$ in the coprecipitates, are summarized in Table 12.

Furthermore, the horizontal part observed in Pu(III) concentrations extends to the pH = 6 - 9.5 interval, where the solubility of pure Pu $(OH)_3(s)$ would be expected to increase steeply due to the formation of Pu $(OH)^{2+}$ or Pu^{3+}species. This behaviour further indicates that the release of Pu(III) from the co-precipitate is mainly controlled by the release of U.

Table 12. Values of log K_x, $a_{Pu(OH)_3(s)}$ and $\lambda_{Pu(OH)_3(s)}$ estimated from data for pH > 9.

$X_{Pu(OH)_3}$	log K_x	log $a_{Pu(OH)_3(s)}$	log $\lambda_{Pu(OH)_3(s)}$
1	14.6	0.00	0.00
0.05	13.9	-0.7	0.6
0.01	13.2	-1.4	0.6

5.14. Kinetics of solubility equilibria for the U-Pu-Np coprecipitate solids

The evolution of U-Pu-Np concentrations in solutions as a function of equilibration time was studied to determine whether the system reached equilibrium during solubility experiments. As shown in Fig. 65, the total concentrations of U and the minor components Pu-Np in contact with the coprecipitated solids remain very similar after 7, 14, 21, and 30 days. Only a slight decrease in concentration over time is observed, which is likely due to the aging of the initially amorphous solid phase. A similar observation was also observed in the U-Ce coprecipitate study and similar conclusion can be made.

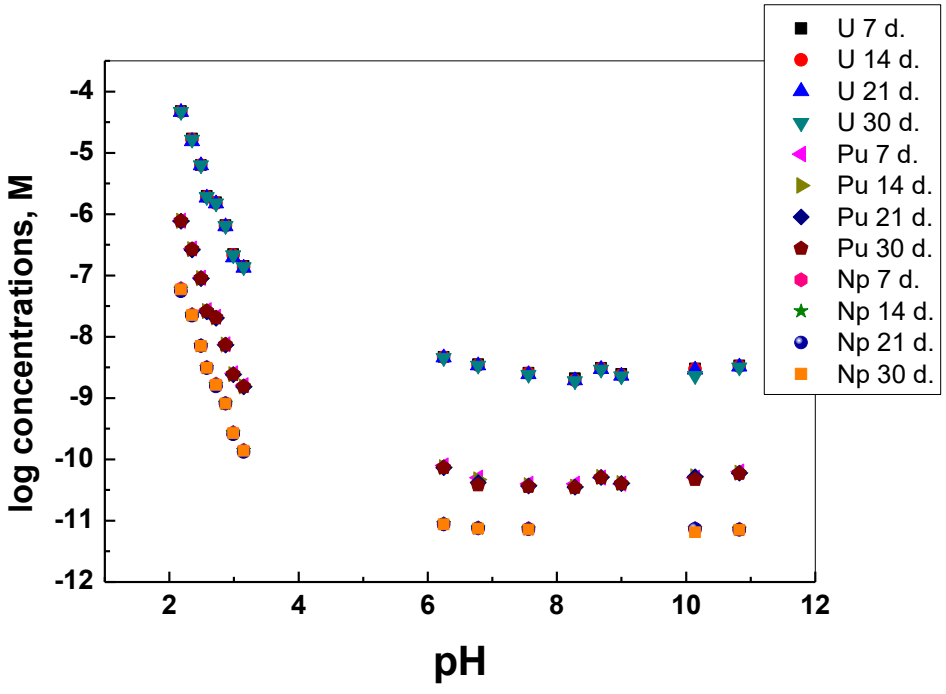

Figure 65: Evolution of total U, Pu, and Np concentrations during 30 days of equilibration for the solid containing 1% Pu and 0.1% Np.

5.15. Equilibrium distribution between the U-Pu-Np solid and aqueous phase

The plot of the normalized concentrations of Pu-Np relative to U concentration have quite some spreads, particularly at low pH range, but indicates that the Pu or Np release from the solid matrix is totally controlled by U dissolution and remains independent of time, demonstrating a congruent release mechanism. The corresponding distribution factor, calculated according to the Berthelot–Nernst relationship (McIntire 1963) [207].

$$\frac{[\text{Pu or Np}]_{(s)}}{[\text{U(IV)}]_{(s)}} = \text{D}\frac{[\text{Pu or Np}]_{(aq)}}{[\text{Pu or Np}]_{(aq)}} \qquad (70)$$

A similar behavior is observed for Ce with respect to U concentration, where the plot of the normalized concentrations with respect to U concentration also shows some spread at low pH but confirms congruent release controlled by uranium dissolution.

The calculated distribution factors are D = 0.62 for both the 1% Pu solid and 5% Pu solid. The corresponding distribution coefficient for Np was D = 0.48 for the 0.5% Np solid and 0.62 for the 0.1% Np solid.

6.0 Conclusions

Understanding the migration behavior of UO_2 in groundwater systems in the presence of iron is essential for evaluating the safety of geological repositories and predicting the environmental fate of dissolved U. Investigation of the reduction of Ca- uranyl complexes in the presence of metallic iron demonstrates that iron within fuel canister inserts provides an additional reducing capacity to the system. The reducing effect of the iron foils resulted in a significant decrease in the dissolved U concentration from ~ $4.2 \cdot 10^{-6}$ M to ~10^{-9} M across all groundwater compositions, which is quite similar to the reported equilibrium solubility limit of UO_2(am) [35]. Solid characterizations of the iron foil using SEM-EDX and XPS confirmed the formation of UO_2(s) precipitates on the iron foil surfaces. These precipitates occurred on carbonate green rust formed on the corroding iron foil surfaces. While Ca–uranyl–carbonato complexes slightly reduced the reaction rate, they did not inhibit reductive precipitation, indicating that dissolved U(VI) can be effectively reduced and immobilized as UO_2(s) on corroding iron surfaces under repository-relevant conditions. These results indicate that, in the event of a canister failure within a geological repository, dissolved U present as U(VI) would be expected to undergo reduction and subsequently reprecipitate as probably UO_2 on the corroding iron surface.

In the leaching study, the corrosion of an un-irradiated MOX fuel pellet (10 wt% Pu with high specific alpha activity of 1.79 GBq/g) was investigated under an Ar atmosphere in simplified carbonate-containing water solution (10 Mm NaCl and 2mM $NaHCO_3$, referred to as 10:2 solution) and in simulated Forsmark groundwaters in the presence of metallic iron foils and iron powder. The findings in the carbonate-containing 10:2 solutions in the absence of metallic iron show a steady increase in U concentrations over the entire duration of the leaching test. This indicates that oxidized U(VI) was released in the solution due to the formation of radiolytic oxidants such as H_2O_2 at the pellet surface, thereby increasing U solubility. The results clearly demonstrate that, in the absence of metallic iron, radiolytic oxidants formed under α-radiation promote oxidative dissolution of the MOX fuel, leading to a continuous increase in dissolved concentrations. In contrast, in the presence of metallic iron and simulated Forsmark groundwater, the study shows that anoxic iron corrosion effectively establishes and maintains reducing conditions. The generation of Fe(II) and H_2, together with the formation of iron corrosion products, successfully counteracts the oxidative effect induced by α-radiolysis. As a result, the oxidative dissolution of MOX fuel is strongly suppressed. This is evidenced by the consistently measured low dissolved U concentrations, which are in good agreement with the lower solubility limit of UO_2(am), and Pu concentrations are below the detection limits.

Furthermore, the linear increase in Fe(II) concentration and the accumulation of dissolved H_2 (1.6 m M) confirm corrosion of the metallic iron in contact with the synthetic Forsmark groundwater as occurred at the end of the 508- day leaching period. The very limited total uranium release over more than one year, together with its predominant association with solid phases, indicates that uranium remains largely in the reduced U(IV) state and is effectively retained within the system. Surface characterization supports these findings, showing the formation of Fe(III)-bearing secondary phases on the MOX pellet, likely resulting from the consumption of radiolytic oxidants, as well as Fe(II)-containing corrosion products formed on iron surfaces. These processes further contribute to buffering the redox conditions. Overall, this study demonstrates that under repository-relevant conditions, the presence of metallic iron can effectively mitigate α-radiation-induced oxidative dissolution of MOX fuel. This confirms that iron can play a critical role in maintaining reducing conditions and enhancing the long-term stability of spent nuclear fuel in a

deep geological repository. In the subsequent study, to better understand if dissolved H_2 has any influence on the process, a leaching test of the same MOX fuel pellet (10% Pu) in the presence of magnetite and synthesized chukanovite was carried out. A strong inhibiting effect on fuel dissolution was observed for chukanovite. The relatively high Fe(II) concentrations resulting from the equilibration of the Forsmark groundwater with chukanovite counteract the oxidative dissolution caused by the high alpha field of the MOX fuel pellet. Whereas magnetite, on the other hand, produces much lower concentrations of Fe(II) in equilibrium with groundwater, which are not sufficient to suppress or inhibit the radiolytic dissolution of the MOX pellet. Magnetite exhibited a comparatively weaker reducing capacity despite its ability to reduce U(VI) to some extent.

In the final work, the coprecipitation studies were undertaken to understand the behaviour of SNF observed during the spent nuclear fuel leaching test carried out in the presence of H_2.In this work, the study of the solubility behaviour of U and the minor components of the nuclear waste matrix in relation to the major component UO_2 was investigated. This study addresses the potential coprecipitation formation behaviour of the UO_2 matrix in connection with a near-field situation under repository conditions. In the preliminary study, solid containing two different proportions of U(IV) with Ce(III), ($Ce_{0.01}U_{0.99}$ and $Ce_{0.10}U_{0.90}$) and in the subsequent study solid containing two different proportions of U(IV) with Pu and Np ($Pu_{0.01Np0.001}U_{0.989}$ and $Pu_{0.05Np0.005}U_{0.945}$) similar to their composition in SNF were successfully co-precipitated as amorphous solid solutions through neutralization of their acidic solutions at room temperature in glove box atmosphere and in the presence of sodium dithionite. The coprecipitate solids were then equilibrated over a wide pH range in 1 M $NaClO_4$(U-Ce) and 0.01 M NaCl solution (U-Pu-Np) containing dithionite, in an undersaturation test. The results demonstrate that the amorphous coprecipitates attained equilibrium rapidly, typically within one week in both cases. In both coprecipitation studies, the measured concentrations of U in equilibrium with the coprecipitate were in excellent agreement with the reported solubility of UO_2(am) under reducing conditions [35].In the initial study, the Ce concentrations were completely dominated by the release of U. Ce concentrations were consistently lower than U across the pH range and increased slightly with higher Ce content in the solids, indicating that $Ce_xU_{1-x}O_{2\pm y}$ solids behave thermodynamically as solid solutions. The activity coefficients of $Ce(OH)_3$(s) in the coprecipitate are much less than 1, indicating thermodynamically favorable mixing behavior of $Ce(OH)_3$ with UO_2. Several multiple analytical techniques were used to characterize the solids (chemical analysis, SEM-EDX, XRD, XAS, XPS) to determine nature of solid solution formed. The SEM-micrographs obtained show that the solids are uniform in appearance, with elemental mapping analysis confirming homogeneous distribution of Ce in the UO_2 matrix. The XRD results indicate that the solubility controlling solids are amorphous in both studies. The systematic decrease in lattice parameters with increasing Ce content provides further evidence of solid solution formation and structural integration within the UO_2 matrix. Surface XPS analysis confirms that U was present as U(IV) while Ce was present as Ce(III) oxidation state in the U-Ce coprecipitated solid.

In the U-Pu-Np study, the releases of Np indicated formation of ideal solid solutions between UO_2(s) and NpO_2(s). The release of Pu from the coprecipitates was totally dominated by the release of uranium in the whole pH range. The Pu concentrations decrease slightly with the decrease of Pu content in the solid, suggesting that $Pu_xNp_yU_{1-x-y}O_{2\pm x\pm y}$ solids behave thermodynamically as solid solutions. Solid characterizations by SEM-EDX/WDS analysis with elemental mapping indicate that U, Pu and Np appear homogenously distributed in the coprecipitated solid. XRD

analysis shows the lattice parameter decreases with increasing Pu and Np content, following Vegard's law and confirming homogeneous solid solution formation with lattice contraction relative to UO_2. XANES analysis confirms the oxidation state of Pu in the solids as Pu(IV) and not Pu(III) which can probably be attributed to the oxidation of the samples as a result of the long storage in the glove box or during transport of the samples to the beamline.

In both coprecipitation studies, the measured solubilities and calculated conditional solubility products of $Ce(OH)_3$ or $Pu(OH)_3$ from the coprecipitate were several orders of magnitude lower than their pure hydroxides solid phases. These results imply that incorporation into the UO_2 matrix can significantly lower the effective solubility of these minor components (Ce, Pu, Np) relative to their corresponding pure hydroxide phases. These findings suggest that, under reducing conditions relevant to geological repositories, the concentration of transuranic actinides and other lanthanides released from the UO_2 fuel matrix during spent fuel alteration or oxidative dissolution will not be determined by their individual solubilities when they coprecipitate with UO_2(s) at the iron surface of the canister insert but will be orders of magnitude lower. It can be concluded that the solubility of the minor components cannot be only predicted on the basis of their individual solid phases but rather also on their coprecipitation behaviour (formation of solid solutions) with other radionuclides present in the spent fuel matrix.

Future work

Building on the methodology and experience gained from the study of the co-precipitation of Pu and Np with UO_2, future work should focus on improved control of sample handling and characterization to ensure the preservation of the redox state of the coprecipitated solids. All sample preparation and transfer should be carried out entirely under an inert atmosphere (glove box). In addition, characterization of the coprecipitates should be performed immediately after synthesis to minimize any alteration of the original oxidation states. To further strengthen the understanding of redox chemistry and local structure within the solid phases, complementary spectroscopic techniques such as XANES and XPS should be carried out.

Additionally, studies on the dissolution behaviour of spent nuclear fuel in the presence of iron corrosion products (such as chukanovite or siderite) should be carried out to better simulate repository conditions and to provide further insights into radionuclide release under reducing conditions. This is especially important for thick carbon steel canisters, which in the majority of cases will be almost completely corroded when fuel contacts water, and only corrosion products can counteract the oxidative dissolution of the spent fuel.

The work of Rai and coworkers [224] demonstrates the strong sensitivity of Pu solubility to redox conditions. The observed variability in the neutral to alkaline pH range further highlights the difficulty of maintaining a well-defined oxidation state in aqueous systems. These findings point to the need for improved understanding of Pu(III) chemistry under reducing conditions. Future work should therefore focus on the stability and behaviour of Pu(III) under repository-relevant reducing conditions, particularly in systems containing metallic iron and iron corrosion products. The work of Rai and coworkers [224] has shown that Pu(IV) can be reduced to Pu(III) in the presence of Fe(II), and that the extent of this reduction is strongly influenced by the nature of Fe(III) solid phases formed. However, complete equilibration is often not achieved, and the molecular-scale mechanisms controlling electron transfer at mineral–water interfaces remain unresolved.

In the context of SNF disposal systems where metallic iron is present, it is therefore essential to investigate the stability of Pu(III), its interaction with iron corrosion products, and its potential impact on plutonium mobility under long-term reducing conditions. Systematic studies of Pu(III) solubility, hydrolysis, and carbonate complexation are essential, as these processes are expected to govern plutonium speciation in deep geological repository environments. Improved thermodynamic data for Pu(III) would reduce uncertainties in geochemical models and enhance the reliability of long-term safety assessments.

Acknowledgments

Reaching this milestone has been challenging yet rewarding, and I am deeply grateful to everyone who has contributed to and supported me along the way.

First and foremost, I would like to express my profound gratitude to my supervisor, Prof. Christian Ekberg, for his leadership, unwavering guidance, invaluable insights. His high standards and clear expectations have continually challenged me to grow as a researcher. I am equally grateful for the opportunity to study in Sweden at Chalmers University of Technology.

I also extend my sincere appreciation to my co-supervisor, Prof. Kastriot Spahiu, and Dr. Marcus Hedberg, whose expertise, interest, and support have been crucial to my work. Your support has been indispensable, and I am deeply appreciative of the time and effort you have devoted to my research and development, which have helped me navigate the challenges of this journey.

I would like to express my sincere gratitude to my examiner, Prof. Teodora Retegan Vollmer, for her kindness, insightful feedback, and continuous encouragement, which greatly contributed to the development of this thesis and my professional growth.

I want to acknowledge everyone from the Nuclear Chemistry and Industrial Material Recycling group, beginning with the seniors, post doc. and to my colleagues, especially Esraa, Letizia, Mariam, Pawan, Kwanele and my wonderful office mates Luca and Georgios for providing a stimulating and supportive academic environment. The group's commitment to excellence and quality research has been a continuous source of inspiration and admiration.

My sincere gratitude also goes to Dr. Stellan Holgersson and Dr. Stefan Allard for ensuring that all necessary resources were always available and for maintaining an efficient, organized, and safe laboratory environment, which has had a positive impact on my work.

I would also like to thank our administrator, Sandra Nayeri, for her support and kindness, and for ensuring that all my administrative needs are met.

My heartfelt appreciation goes to my parents, sisters and brothers, my beloved and adorable wife (Fatima), my children (Mubarak and Inaya), my role model (Prof. Foluke), and my close friends (Arma, Mubarak, Ismaili, Tasleem, Hamza, Emeka, Levi, David) both far and near, for your unwavering love, support, and encouragement. Your belief in me has been my greatest source of strength and motivation throughout this journey.

This thesis is as much a result of your support as it is of my work. Thank you all for being part of this journey with me.

Lastly, the Swedish Nuclear and Fuel and Waste Management Company (SKB) is greatly acknowledged for funding this research project (I.D.: 21235062), and I extend my gratitude to Dr. Lena Zetterström Evins.

Mustapha G. Saleh

May 2026, Gothenburg

References

[1] International Energy Agency (IEA), Electricity Report (2024). Analysis and forecast to 2026.
[2] World Nuclear Association. (2024). Nuclear Power in the World Today. London: WNA.
[3] International Energy Agency. World Energy Outlook (2024). Paris: IEA; 2024.
[4] International Atomic Energy Agency (IAEA). (2025). IAEA Raises Nuclear Power Projections for Fifth Consecutive Year. Press Release No. 89/2025. Vienna: IAEA.
[5] International Atomic Energy Agency (IAEA). (2025). Power Reactor Information System (PRIS). Vienna: IAEA. https://pris.iaea.org/pris/.
[6] Kornecki, K. Wise, C.F (2024). The role of advanced nuclear reactors and fuel cycles in a future energy system. PNAS Nexus, vol. 3, no. 2, pp.030.

[7] Kim, Y., Kim, W.,Kim, M. (2014). An international comparative analysis of public acceptance of nuclear energy. Energy policy 66 pp. 475-483.

[8] OECD Nuclear Energy Agency. (2013). Nuclear energy today (2nd ed.). OECD Publishing. https://doi.org/10.1787/9789264179233-en
[9] Clayton, R., Kirk, J., Banford, A., Stamford, L. (2025). A review of radioactive waste processing and disposal from a life cycle environmental perspective. Clean Technologies and Environmental Policy, Vol. 27, pp. 665–682.
[10] World Nuclear Waste Report. (2019). Focus Europe. Heinrich-Böll-Foundation, Nuclear Transparency Watch, Bund für Umwelt und Naturschutz Deutschland (BUND).
[11] Park, S., Ewing, R. C. (2023). US legal and regulatory framework for nuclear waste from present and future reactors and their fuel cycles. Annual Review of Environment and Resources, 48, pp.713–736.
[12] World Nuclear Association. (NEA). (2026). Nuclear power in Sweden.
[13] Svensk Kärnbränslehantering AB. (2011). Technical report TR-11-01 Volume 1 – Long-term safety for the final repository for spent nuclear fuel at Forsmark.
[14] Selroos, J., Gylling, M. (2023). Disposal of high-level radioactive waste in crystalline rock: On coupled processes and site development. Rock Mechanics Bulletin, 2(3), 100061.
[15]Strömberg.B., Sonnerfelt., L., Öberg. H. (2019). Exploratory what-if analysis of some debated canister failure modes in the review of a licence application for the construction and operation of a spent nuclear fuel repository in Sweden.Advances in Geoscience, 49, pp. 67–75.
[16] Grenthe, I., Gaona, X., Plyasunov, A., Rao, L., Runde, W. H., Grambow, B., Konings, R. J. M. Smith, A. L., Moore, E. E. (2020). Second update on the thermodynamics of U, Np, Pu, Am and Tc. OECD Nuclear Energy Agency Data Bank Eds., OECD publications, Paris, France.
[17] Spinks, J.W.T., Woods, R. J (1990). An Introduction to Radiation Chemistry, 3rd ed., John Wiley & Sons Inc, New York,
[18] Puranen, A., Barreiro-Fidalgo, A., Evins, L.Z., K. Spahiu. (2020). Spent fuel corrosion and the impact of iron corrosion – The effects of hydrogen generation and formation of iron corrosion products, J. Nucl. Mater. 542, 152 423.
[19] Choppin G.R, Liljenzin J.O, Rydberg J, Ekberg C. (2013). Radiochemistry and Nuclear Chemistry. 4th Edition. Amsterdam: Elsevier.
[20] Clark D.L, Hecker S.S, Jarvinen G.D, Neu M.P. (2006). Actinide chemical behavior and properties. In: Morss LR, Edelstein N, Fuger J, editors. The chemistry of the actinide and transactinide elements. Dordrecht: Springer. pp. 813–1264.

[21] Grenthe, I., Drożdżyński, J., Fujino, T., Buck, E. C., Albrecht-Schmitt, T. E., & Wolf, S. F. (2008). Uranium. In L. R. Morss, N. M. Edelstein, & J. Fuger (Eds.), The chemistry of the actinides and the transactinide elements (4th ed., pp. 253–698). Springer.
[22] Kasztelan S, Grambow B, Dressler R. (2012). Aqueous chemistry of plutonium. In: Hoffman DC, editor. The Plutonium Handbook. 2nd Edition. La Grange Park (IL): American Nuclear Society; pp. 1469–1588.
[23] Holden, N. (1977). Isotopic composition of the elements and their variation in nature: a preliminary report, in, Brookhaven National Lab.
[24] Burns P.C, Finch R, editors. (1999). Uranium: Mineralogy, Geochemistry and the Environment. Reviews in Mineralogy & Geochemistry, Vol. 38. Washington (DC): Mineralogical Society of America.
[25] Langmuir D. (1997). Aqueous Environmental Geochemistry. Upper Saddle River (NJ): Prentice-Hall.
[26] Costa Peluzo, B. M. T., Kraka, E. (2022). Uranium: The Nuclear Fuel Cycle and Beyond. International Journal of Molecular Sciences, 23(9), 4655.
[27] Hixon, A. E. Powell, B. A. (2018). Plutonium environmental chemistry: Mechanisms for the surface-mediated reduction of Pu(V/VI). Environmental Science*:* Processes and Impacts, 20(10), pp.1306–1322.
[28] Neck, V., Kim, J.I. (1989). Solubility and hydrolysis of plutonium. Radiochim Acta. 2001(1) pp.1-16
[29] Geckeis, H., Salbu, B., Schäfer, T., Zavarin, M. (2016). Environmental chemistry of plutonium. In D. L. Clark, D. A. Geeson, & R. J. Hanrahan, Jr. (Eds.), Plutonium Handbook (2nd ed.). American Nuclear Society.
[30] Rai, D., Moore, D. A. (2003). Plutonium adsorption and solubility in natural and engineered systems. Journal of Radioanalytical and Nuclear Chemistry, 258(1), pp. 1–17.
[31] Kersting, A. B. (2013). Plutonium transport in the environment. Inorganic Chemistry, 52 (7), pp.3533–3546.
[32] Yoshida, Z., Johnson, S. G., Kimura, T., Krsul, J. R. (2010). Neptunium. In L. R. Morss, N. M. Edelstein, J. Fuger (Eds.), The Chemistry of the Actinide and Transactinide Elements (Vol. 2, pp. 699–812. Springer
[33] Kerridge J.F, Platt A.W. (1982). Aqueous chemistry of neptunium. Coord Chem Rev. 41(1): pp.1–36.
[34] Silva, R. J., Bidoglio, G., Rand, M. H., Robouch, P. B., Wanner, H., Puigdomènech, I. (1995). Chemical thermodynamics of neptunium. OECD Nuclear Energy Agency.
[35] Neck, V., Kim, J. I. (2001). Solubility and hydrolysis of tetravalent actinides. Radiochimica Acta, 89, pp.1–16.
[36] OECD Nuclear Energy Agency. (2021). Strategies and considerations for the back end of the fuel cycle (Nuclear Technology Development and Economics). OECD Publishing.
[37] OECD/NEA (2024). Progress and Challenges in the Back End of the Nuclear Fuel Cycle. Organisation for Economic Co-operation and Development, Nuclear Energy Agency, Paris.

[38] Kutty, T. R. G., Hegde, P. V., Khan, K. B., Basak, U., Pillai, S. R., Sengupta, A., Jain, G. C., Majumdar, S. H., Kamath, H. S., Purushotham, D. S. C. (2002). Densification of UO_2 in six different atmospheres. Journal of Nuclear Materials, 305(2–3) pp.159–168.

[39] OECD/NEA (2025). Scientific Updates on Advanced Nuclear Fuel Cycle Research. OECD Nuclear Energy Agency.

[40] Ewing, R.C. (2008). Nuclear fuel cycle. Environmental impact, MRS Bulletin, Volume 33 pp.338-340.

[41] Rodríguez-Penalonga, L., Moratilla Soria, B. Y. (2017). A review of the nuclear fuel cycle strategies and the spent nuclear fuel management technologies. Energies, 10(8), 1235.

[42] Nuclear Engineering and Technology (2025). Comprehensive review of small modular reactor development, focusing on challenges in the backend nuclear fuel cycle. Nuclear Engineering and Technology.

[43] IAEA (2023). Periodic Safety Review for Nuclear Fuel Cycle Facilities. International Atomic Energy Agency, Vienna.

[44] World Nuclear Association (2025). World Nuclear Fuel Report 2025. World Nuclear Association.

[45] U.S. NRC. (2017). Nuclear Regulatory Commission, United State of America.

[46] Bruno, J., Ewing, R.C. (2006). Spent nuclear fuel. Elements, Volume 2. pp.343-349.

[47] Cui, D., Lowa, J., Spahiu, K. (2011). Environmental behaviors of spent nuclear fuel and canister materials. Energy Environ.Sci., 4, pp.2537-2545.

[48] International Atomic Energy Agency. (2022). Status and trends in spent fuel and radioactive waste management (IAEA Nuclear Energy Series No. NW-T-1.14). Vienna: IAEA. https://www.iaea.org/newscenter/news/international-conference-on-spent-fuel-management-starts-today

[49] Ewing, R.C., Runde, W., Albrecht-Schmitt, T.E. (2010). Environmental impact of the nuclear fuel cycle: Fate of actinides MRS bulletin volume 35.

[50] Johnson, L.H., Shoesmith, D.W. (1988). Spent Fuel. In: Lutze W, Ewing RC (eds) Radioactive Waste Forms for the Future. North-Holland, Amsterdam, pp. 635-698.

[51] Oversby, V.M. (1994). Nuclear Waste Materials. In: Cahn RW, Haasen P, Kramer EJ (eds) Materials Science and Technology, Chapter 12 from volume 10B, VCH Verlagsgessellschaft mbH, pp. 391-442.

[52] Klosek, V., Hunault, M. O. J. Y., Schlutig, S., Tomczak, W., Rochedy, M., Solari, P. L., Noirot, J. (2023). Fission product speciation across a UO_2 spent nuclear fuel. Journal of Nuclear Materials, 586, 154660.

[53] Jevremovic, T. (2009). Nuclear Principles in Engineering 2nd edition; Nuclear Reactor Control pp. 491-516 Springer.com.

[54] Cammi, A., Loi, L., Missaglia, A., Tumminelli, L., Giacobbo, F., Padovani, E. (2025). Photonuclear treatment for spent fuel radiotoxicity reduction: A case study investigation on minor actinides. Nuclear Engineering and Design, 442, Article 114204.

[55] Hedin, A. (1997). spent nuclear fuel- How Dangerous is it? Technical report TR-97-13 1-60 (SKB).

[56] Ewing, R.C. (2015). Long-term storage of spent nuclear fuel Nature material Vol 14.

[57] Terranova, M. L., Tavares, O. A. P. (2024). Trends and perspectives on nuclear waste management: Recovering, recycling, and reusing. Journal of Nuclear Engineering, 5(3), pp.299–317.

[58] Kleykamp, H (1985). The chemical state of the fission products in oxide fuels. Journal of Nuclear Material 131,pp.221-226.

[59] Sakib, S., Lu, Y., Howard, C. B., Burns, J., Chen, W.-Y., Malakkal, L., Jiang, C., Biswas, S., Cappia, F., He, L. (2025). In-situ ion irradiation of a spent UO_2 fuel: Evolution of fission products and nanograins with radiation dose. Journal of Nuclear Materials, 614, 155859.

[60] Buck E.C, Hanson B.D, McNamara B.K. (2004). The geochemical behaviour of Tc, Np and Pu in spent nuclear fuel in an oxidizing environment. In: Gieré R, Stille P (eds) Energy, Waste, and the Environment: a Geochemical Perspective. The Geological Society of London Special Publication 236: pp 65-88.

[61Adeola,A.O., Iwuozor,K.O., Akpomie,G.,Adegoke,K.A., Oyedotun,K.O., Ighalo,J.O.,Amaku, J.F., Olisah,C.,Conradie,J. (2023). Advances in the management of radioactive wastes and radionuclide contamination in environmental compartments: a review., Environ Geochem Health 45: pp.2663–2689.

[62] Darda, S.A., Gabbar, H.A., Damideh, V., Aboughaly, M., Hassen.I. (2021). A comprehensive review on radioactive waste cycle from generation to disposal Journal of Radioanalytical and Nuclear Chemistry (2021) 329: pp.15–31.

[63] Kreusch, J., Neumann,W., Appel,D., Diehl,P. (2006). Nuclear Fuel Cycle Nuclear Issues Paper No. 3.

[64] Na¨slund,J.O.,Brandefelt, J., Liljedahl,L.C.(2013). Climate Considerations in Long-Term Safety Assessments for Nuclear Waste Repositories AMBIO, 42:393–401.

[65] Nuclear Energy Agency (NEA) (2020). Management and disposal of high-level radioactive waste: Global progress and solutions.

[66] Holm, M. (2011). RadTox, a computer program for assessing radiotoxicity curves for used nuclear fuel. Chalmers University of Technology, Department of Nuclear Chemistry, Master's thesis.

[67] Brantberger, M., Zetterqvist, A., Arnbjerg-Nielsen, T., Olsson, T., Outters, N., & Syrjänen, P. (2006). Final repository for spent nuclear fuel: Underground design Forsmark, layout D1.

[68] Nuclear Energy Agency, NEA (2023). Deep Geological Repositories and Nuclear Liability (OECD Publishing). NEA No. 7596

[69] Shoesmith D.W. (2000). Fuel corrosion processes under waste disposal conditions. Journal of Nuclear Materials 282: pp.1-31

[70] OECD/NEA. (2020). National Inventories and Management Strategies for Spent Nuclear Fuel and Radioactive Waste. Final Methodology. NEA no.7323

[71] Swedish Government office (2022). Government approves final repository for spent nuclear fuel at Forsmark. Press release, 27 January 2022, Stockholm, Sweden.

[72] Fuel and Canister Process Report for the Safety Assessment SR-Can. (2006). SKB Technical Report, TR-06-22.

[73] Ewing, R.C., Weber, W.J., Clinard, F.W. (1995). Radiation effects in nuclear waste forms for high-level waste radioactive waste, progress in nuclear energy, 29 pp.63-127.

[74] Herm, M., Walschburger, A., König, T., Metz, V.,Geckeis, H. (2023). Experimental investigation of uranium release from spent nuclear fuels under conditions expected in a deep geological repository. Safety of Nuclear Waste Disposal, 2, pp.149–150.

[75] Spahiu, K., Cui, D., Lundström, M. (2004). The fate of radiolytic oxidants during spent fuel leaching in the presence of dissolved near-field hydrogen. Radiochim. Acta 92, pp. 625–629.

[76] Sunder, S., Shoesmith, D.W., Miller, N.H. (1997).Oxidation and dissolution of nuclear fuel (UO_2) by the products of the alpha radiolysis of water. Journal of Nuclear Materials 244 pp. 66–74.

[77] Christensen, H., Sunder, S. (2000). Current State of Knowledge of Water Radiolysis Effects on Spent Nuclear Fuel Corrosion, Nuclear Technology, 131:1, pp.102-123.

[78] Johnson, L.H., Leneveu, D.M., Shoesmith, D.W., Oscarson, D.W., Gray, M.N., Lemire, R.J., Garisto, N.C. (1994). The disposal of Canada's Nuclear Fuel Waste: The Vault Model for Post-Closure Assessment, Atomic Energy of Canada Limited Report, AECL-10714.

[79] Shoesmith, D.W., Sunder, S. Hocking, W.H. (1994). in: Electrochemistry of Novel Materials, eds. J. Lipkowski and P.N.Ross VCH, New York, p. 297.

[80] Parks, G. A., Pohl, D.C. (1988). Hydrothermal solubility of uraninite Geochim. Cosmochim. Acta 52,.pp 863-875.

[81] Lemire, R.J., Garisto, F. (1989). The Solubility of U, Nb, Pu, Th and Tc in a Geological Disposal Vault for Used Nuclear Fuel, Atomic Energy of Canada Limited Report, AECL10009.

[82] Amme, M., Svedkauskaite, J., Bors, W., Murray, M., Merino, J. (2007). A kinetic study of UO_2 dissolution and H_2O_2 stability in the presence of groundwater ions. Radiochimica Acta, 95 (12), pp. 683–692.

[83] Springell, R., Rennie, S., Costelle, L., Darnbrough, J., Stitt, C., Cocklin, E., Lucas, C., Burrows, R., Sims, H., Wermeille, D., Rawle, J., Nicklin, C., Nuttall, W., Scott, T., Lander, G. (2015). Water corrosion of spent nuclear fuel: Radiolysis driven dissolution at the UO_2 /water interface. Faraday Discussions, 180, pp.301–311.

[84] Jonsson, M., Nielsen, F., Roth, O., Ekeroth, E., Nilsson, S., Hossain, M.M. (2007). Radiation induced spent nuclear fuel dissolution under deep repository conditions. Envir. Sci. Technol. 41, pp.7087-7093.

[85] Ekeroth, E., Roth, O., Jonsson, M. (2006). The relative impact of radiolysis products in radiation induced oxidative dissolution of UO_2 . Journal of Nuclear Materials 355 pp. 38–46.

[86] Merino , J., Cera ,E., Bruno, J., Quinones, J., Casas, I., Clarens, F., Gimenez , J., de Pablo, J., Rovira, M., Martınez-Esparza, A. (2005). Radiolytic modelling of spent fuel oxidative dissolution mechanism. Calibration against UO_2 dynamic leaching experiments, Journal of Nuclear Materials. Vol. 346, Issue 1, pp. 40-47.

[87] Olsson, D., Aydogan, H., Jonsson, M. (2024). The influence of bicarbonate concentration and ionic strength on peroxide speciation and overall reactivity towards UO_2. RSC Advances, 14 (23), pp.16248–16254.

[88] Buck, E. C., Wittman, R. S., Skomurski, F. N., Cantrell, K. J., McNamara, B. K., & Soderquist, C. Z. (2012). Radiolysis process modeling results for scenarios. Used fuel disposition. (PNNL-21554). Pacific Northwest National Laboratory.

[89] Criticality Effects of Long-Term Changes in Material Compositions and Geometry in Disposal Canisters. (2016) SKB Technical Report, TR-16-06 .

[90] Jonsson, M. (2012). Radiation Effects on Materials Used in Geological Repositories for Spent Nuclear Fuel, ISRN Materials Science, Article ID 639520, 13.

[91] Saheb, M., Neff, D., Dillmann, P.H., Matthiesen, H., Foy, E. (2008). Long-term corrosion behaviour of low-carbon steel in anoxic environment: Characterisation of archaeological artefacts, J. Nucl. Mater. 379 pp. 118–123.

[92] Odorowski, M., Jegou,C., de Windt, C.L.,Broudic,V.,Jouan,G.,Peuget,S.,Martin,.C. (2017). Effect of metallic iron on the oxidative dissolution of UO_2 doped with a radioactive alpha emitter in synthetic Callovo-Oxfordian water, Geochim. Cosmochim. Acta 219, pp.1-21.

[93] Ishikawa, T., Kondo,Y., Yasukawa,A., Kandori, K. (1998). Formation of magnetite in the presence of ferric oxyhydroxides, Corros. Sci. 40 pp. 1239–1251.

[94] Ritter, K., Odziemkowski, M.S., Gillham, R.W. (2002). An in-situ study of the role of surface films on granular iron in the permeable iron wall technology, J. Contam. Hydrol. 55, pp.87–111.

[95] Smart, N.R., Blackwood, D.J., Werme, L. (2001). The anaerobic corrosion of carbon steel and cast iron in artificial groundwaters, SKB Technical Report TR-01-22.

[96] Smart, N.R., Rance, A.P., Werme, L.O (2008). The effect of radiation on the anaerobic corrosion of steel, J. Nucl. Mater. 379. pp. 97-104,

[97] Loida, A., Kelm,M., Kienzler, B., Geckeis, H., Bauer,A.(2006).The Effect of Nearfield Constraints on the Corrosion Behavior of High Burnup Spent Fuel, Mat. Res. Soc. Symp. Proc. 932 (72.1).

[98] Neretnieks, I. (1985). Some aspects of the use of iron canisters in deep lying repositories for nuclear waste.Nagra.

[99] Bonin, B., Colin, M., Dutfoy, A. (2000). Pressure building during the early stages of gas production in a radioactive waste repository. Journal of Nuclear Materials, 281(1) pp. 1-14.

[100] Wu, L., Qin, Z., Shoesmith, D.S. (2014). An improved model for the corrosion of used nuclear fuel inside a failed waste container under permanent disposal conditions, Corros. Sci. 84, pp. 85–95.

[101] Amme, M., Pehrman ,R., Deutsch, R., Roth,O., Jonsson, M. (2012). Combined effects of Fe (II) and oxidizing radiolysis products on UO_2 and PuO_2 dissolution in a system containing solid UO_2 and PuO_2. Journal of Nuclear Materials, 430(1-3): pp. 1-5.

[102] Smith, P.A., Johnson, L.H. Spent Fuel Dissolution: An Examination of the Impacts of Alpha-Radiolysis. MRS Online Proceedings Library 608, 29 (1999).

[103] Carbol, P., Patrik Fors, P., Gouder, T., Spahiu, K. (2009). Hydrogen suppresses UO_2 corrosion. Geochimica and Cosmochimica Acta, 73(15): pp. 4366-4375.

[104] Fors, P., Carbol, P., Winckel,S.V., Spahiu, K. (2009). Corrosion of high burn-up structured UO_2 fuel in presence of dissolved H_2, J. Nucl. Mater. 394 pp. 1–8.

[105] Puranen,A., Roth,O., Evins,L-Z., Spahiu, K. (2018). Aqueous leaching of high burnup UO_2 fuel under hydrogen conditions, in: MRS Advances Scientific Basis for Nuclear Waste Management XLI, 3, Materials Research Society, pp. 1013– 1018.

[106] Ekeroth, E., Granfors, M., Schild, D., Spahiu, K. (2020). The effect of temperature and fuel surface area on spent nuclear fuel dissolution kinetics under H_2 atmosphere, J. Nucl. Mater. 531 , 151981.

[107] Cui, D., Ekeroth, E., Fors, P., Spahiu, K. (2008). Surface Mediated Processes in the Interaction of Spent Fuel or alpha-doped UO_2 with H_2, MRS Symp. Proc. 1104 pp.87–99.

[108] Spahiu, K., Devoy, J., Cui, D., Lundström,M. (2004). The reduction of U(VI) by near field hydrogen in the presence of UO2 (s). Radiochimica Acta, 92(9-11): pp 597-601.

[109] Mennecart, T., Cachoir, C., Lemmens, K., Gaggiano, R., Meert, K., Vandoorne, T. (2024). Fission product release from spent nuclear UOX fuel dissolution: Comparison between anoxic and reducing conditions and impact of pH. MRS Advances, 9, pp.363–367.

[110] Spahiu. K. (2021). EURAD State of Knowledge (SoK) Report, Spent Nuclear Fuel Domain 3.1.1Version, 2021 - ejp-eurad.eu.

[111] Duro, L., Riba, O., Martínez-Esparza, A., Bruno, J. (2013). Modelling the Activation of H_2 on Spent Fuel Surface and Inhibiting Effect of UO_2 Dissolution Mater. Res. Soc. Symp. Proc. Vol. 1518.

[112] Broczkowski, M.E., Zagidulin, D., Shoesmith, D. W. (2010). The Role of Dissolved Hydrogen on the Corrosion/Dissolution of Spent Nuclear Fuel ACS Symposium Series; American Chemical Society: Washington, DC.

[113] Hansson, N. L., Jonsson, M. (2023). Exploring H_2-effects on radiation-induced oxidative dissolution of UO_2-based spent nuclear fuel using numerical simulations. Radiation Physics and Chemistry, 210, 111055.

[114] Saleh, M., Hansson, N. L., Hedberg, M., Spahiu, K., Ekberg, C. (2026). Dissolution of unirradiated MOX fuel in the presence of metallic iron. Journal of Nuclear Materials, 618, 156202.

[115] Fellhauer, D., Gaona, X., Altmaier, M., Geckeis, H. (2021). Radionuclide geochemistry: Solubility and thermodynamics in an HLW repository. SaND: Safety of Nuclear Waste Disposal, 1, pp.149–150

[116] Aspinall, H. C. (2023). Editorial: Solubility phenomena in the context of nuclear waste disposal. Frontiers in Nuclear Engineering, 9, 1332806.

[117] Bruno, J.,Sandino, A. (1998). Coprecipitation of radionuclides with calcite: Estimation of partition coefficients based on a review of laboratory investigations and geochemical data. Applied Geochemistry, 13(8), pp.885–896.

[118] Metz, V., Geckeis, H., González-Robles, E., & Loida, A. (2012). Radionuclide behaviour in the near-field of a geological repository for spent nuclear fuel. Radiochimica Acta, 100(8-9).

[119] Bruno, J., Grenthe, I., Munoz, M. (1985). Studies on radionuclide coprecipitation-solid solution formation. The UO_2(s)-$La(OH)_3$(s) coprecipitation as an analogue for the UO_2(s)-Pu $(OH)_3$(s) system. MRS Symp. Proc. 50, pp.717-726.

[120] Bruno, J., Sandino, A. (1987). Radionuclide coprecipitation, SKB Technical Report TR-87-23, Svensk Kärnbränslehantering AB

[121] Bruno, J., Sandino, A. (1988) The thermodynamics and kinetics of coprecipitation and its effect on radionuclide solubility, Radiochim. Acta 44/45, pp.17-21.

[122] Shannon, R. D. (1976). Revised effective ionic radii and systematic studies of interatomic distances in halides and chalcogenides. Acta Crystallographica Section A, 32(5), pp.751–767.

[123] Rousseau,G., Fattahi,M., Grambow,B., Boucher,F., Ouvrard,G. (2006). Coprecipitation of thorium and lanthanum with UO_{2+X}(s) as host phase. Radiochim.Acta 94,pp. 517-522.

[124] Rousseau, G., Fattahi, M., Grambow. B., Boucher, F., Ouvrard, G. (2002). Coprecipitation of thorium with UO_2 Radiochim. Acta 90,pp. 523-527.

[125] Wu, L., Beauregard, Y., Qin, Z., Rohani, S., Shoesmith, D. W. (2012). A model for the influence of steel corrosion products on nuclear fuel corrosion under permanent disposal conditions. Corrosion Science, 61,pp. 83-91.

[126] Myllykylä, E. (2008). Reduction of uranium in disposal conditions of spent nuclear fuel. Posiva. Posiva Working Report No. 2008-9

[127] Carbol, P., Fors, P., Van Winckel, S., Spahiu, K. (2009). Corrosion of irradiated MOX fuel in the presence of dissolved H_2. J. Nucl.Mater, 392(1), pp.45–54.

[128] Gras, J.-M., Do Quang, R., Masson, H., Lieven, T., Ferry, C., Poinssot, C., Debes, M., & Delbecq, J.-M. (2007). Perspectives on the closed fuel cycle: Implications for high-level waste matrices. Journal of Nuclear Materials, 362(2–3), pp.383–394.

[129] World Nuclear Association. (2024). Mixed oxide fuel (MOX). https://world-nuclear.org/information-library/nuclear-fuel-cycle/fuel-recycling/mixed-oxide-fuel-mox?utm.

[130] Ghislain, J., Jégou, C., De Windt, L., Broudic, V., Peuget, S., Magnin, M., Tribet, M., & Martin, C. (2008). Characterization of plutonium distribution in MIMAS MOX by image analysis. Journal of Nuclear Materials, 375(1),pp. 86–94.

[131] Boulore, A. (2001). Etude et modelisation de la densi fication en pile des oxydes nucleaires UO_2 et MOX, PhD thesis, INP Grenoble and MINES Saint-Etienne.

[132] Odorowski, M., Jégou, C., De Windt, L., Broudic, V., Peuget, S., Magnin, M., Tribet, M., Martin, C. (2016). Oxidative dissolution of unirradiated MIMAS MOX fuel (U/Pu oxides) in carbonated water under oxic and anoxic conditions. Journal of Nuclear Materials, 468, pp.17–25.

[133] Kitamura, A., Takase, H. (2016). Effects of α-radiation on a direct disposal system for spent nuclear fuel – (1) Review of research into the effects of α-radiation on the spent nuclear fuel, canisters and outside canisters. Journal of Nuclear Science and Technology, 53 (1), 1–18.

[134] Spahiu, K., Cui, D., Lundström, M. (2004). The fate of radiolytic oxidants during spent fuel leaching in the presence of dissolved near-field hydrogen. Radiochim.Acta 92, pp.625-629

[135] Jégou, C., Odorowski, M., Kerleguer, V., Broudic, V., Schlegel, M. L., Jouan, G., & Marques, C. (2022). MOX fuel corrosion processes under waste disposal conditions. Corrosion Science, 195, 109964.

[136] Kerleguer, V., Jégou, C., De Windt, L., Broudic, V., Jouan, G., Miro, S., Tocino, F., & Martin, C. (2020). The mechanisms of alteration of a homogeneous $U_{0.73}Pu_{0.27}O_2$ MOX fuel under alpha radiolysis of water. Journal of Nuclear Materials, 529, 151920.

[137] Jégou, C., Caraballo, R., De Bonfils, J., Broudic, V., Peuget, S., Vercouter, T., Roudil, D. (2010). Oxidizing dissolution of spent MOX47 fuel subjected to water radiolysis: Solution chemistry and surface characterization by Raman spectroscopy. Journal of Nuclear Materials, 399(1), pp.68–80.

[138] Kitano, K., Akiyama, H., Nakae, N. (2017). A methodology to predict a fission gas release ratio of MOX fuel with heterogeneous microstructure. Journal of Nuclear Science and Technology, 54(9), pp.1190–1197.

[139] Magnin, M., Jégou, C., Caraballo, R., Broudic, V., Tribet, M., Peuget, S., & Talip, Z. (2015). Oxidizing dissolution mechanism of an irradiated MOX fuel in underwater aerated conditions at slightly acidic pH. Journal of Nuclear Materials, 462, pp.230–241.

[140] Schreinemachers, C., Leinders, G., Mennecart, T., Cachoir, C., Lemmens, K., Verwerft, M., Brandt, F., Deissmann, G., Modolo, G., Bosbach, D. (2022). Caesium and iodine release from spent mixed oxide fuels under repository-relevant conditions: Initial leaching results. MRS Advances, 7, pp.100–104.

[141] Auqué, L. F., Gimeno, M. J., Gómez, J. B., Puigdomenech, I., Smellie, J., & Tullborg, E.-L. (2006). Groundwater chemistry around a repository for spent nuclear fuel over a glacial cycle: Evaluation for SR-Can (Technical Report TR-06-31). University of Zaragoza and Svensk Kärnbränslehantering AB.

[142] Vieno T. (2000). Groundwater Salinity at Olkiluoto and its Effect on a Spent Fuel Repository, Posiva Oy, POSIVA Report 2000-11.

[143] Laaksoharju, M., Smellie, J., Tullborg, E.-L., Gimeno, M., Molinero, J., Gurban, I., & Hallbeck, L. (2008). Hydrogeochemical evaluation and modelling performed within the Swedish site investigation programme. Applied Geochemistry, 23(7), pp.1761–1795.

[144] Kwon, E., Kwon, J.-S., Park, K.-W., & Ju, Y. (2025). A comparative review on groundwater hydrogeochemistry in countries preferring crystalline rock for deep geological disposal. Nuclear Engineering and Technology, 57(6), 103463.

[145] Puigdomenech, I., Trotignon, L., Kotelnikova, S., Pedersen, K., Griffault, L., Michaud, V., Lartigue, J.E., Hama, K., Yoshida, H., West, J.M., Bateman, K., Milodowski, A. E., Banwart, S. A., Rivas Perez, J., Tullborg, E.L (2000). O_2 consumption in a granitic environment. In R. W. Smith & D. W. Shoesmith (Eds.), Scientific Basis for Nuclear Waste Management XXIII: Materials Research Society Symposium Proceedings (Vol. 608, pp. 179–184). Materials Research Society.

[146] Genin, J.M., Abdelmoula,M., Ruby, C. Upadhyay. C (2006). Speciation of iron; characterisation and structure of green rusts and FeII-III oxyhydroxycarbonate fougerite, C. R. Geoscience 338, pp. 402–419.

[147] Duro, L., Bruno, J., Grivé, M., Montoya, V., Kienzler, B., Altmaier, M., & Buckau, G. (2014). Redox processes in the safety case of deep geological repositories of radioactive wastes: Contribution of the European RECOSY collaborative project. Applied Geochemistry, 49, pp.206–217.

[148] Balboni, E., Zavarin, M., Smith, K., Booth, C. (2020). M4SF-20LL010302042: Process model for radionuclide incorporation into corrosion products (LLNL-TR-812110). Lawrence Livermore National Laboratory.

[149] Smedley, P.L., Kinniburgh, D. G. (2023). Uranium in natural waters and the environment: Distribution, speciation and impact. Applied Geochemistry, 148, 105534.

[150] Liu, Z., Liang, Y., Zhu, P., Xu, S., Fei, J., Uralbekov, B.,Wang, Y. (2025). Uranium contamination in groundwater: Sources, speciation, transformations, migration, and remediation strategies. ACS ES&T Water, 5(8), pp.4301–4321.

[151] Nolan, P. J., Bone, S. E., Campbell, K. M., Pan, D., Healy, O. M., Stange, M., Bargar, J. R., Weber, K. A. (2021). Uranium (VI) attenuation in a carbonate-bearing oxic alluvial aquifer. Journal of Hazardous Materials, 412, 125089

[152] Bernhard, G., Geipel, G., Reich,T., Brendler,V., Amayri,S., Nitsche, H. (2001). Uranyl(VI) carbonate complex formation: Validation of the $Ca_2UO_2(CO_3)_3$ (aq.) species. Radiochimica Acta, . 89(8): pp. 511-518.

[153] Kalmykov, S.N., Choppin, G.R. (2000). Mixed Ca^{2+}/ UO_2^{2+}/ CO_3^{2-} complex formation at different ionic strengths. Radiochimica Acta, 88(9-11): pp. 603-608.

[154] Stanley, D. M., Wilkin, R. T. (2019). Solution equilibria of uranyl minerals: Role of the common groundwater ions calcium and carbonate. Journal of Hazardous Materials, 377, pp.315–320.

[155] Grambow, B., Smailos, E., Geckeis, H., Müller, R., Hentschel, H. (1996). Sorption and reduction of uranium (VI) on iron corrosion products under reducing saline conditions, Radiochimica Acta 74, pp.149–154,

[156] D. Cui, K. Spahiu. (2002). The reduction of U (VI) on corroded iron under anoxic conditions, Radiochimica Acta 90, pp. 623-628.

[157] Dewey, C., Sokaras, D., Kroll,T., Bargar, J.R., Fendorf .S.(2020). Calcium-uranyl-carbonato species kinetically limit U (VI) reduction by Fe (II) and lead to U (V)-bearing ferrihydrite, Environ. Sci. Technol. 54, pp. 6021–6030.

[158] Jeon, B.-H., Dempsey, B. A., Burgos, W. D., Barnett, M. O., & Roden, E. E. (2005). Chemical reduction of U(VI) by Fe(II) at the solid–water interface using natural and synthetic Fe(III) oxides. Environmental Science & Technology, 39(15), 5642–5649.

[159] Scott, T., Allen, G.,Heard, P., Randell.M. (2005). Reduction of U (VI) to U (IV) on the surface of magnetite, Geochim. Cosmochim. Acta 69, pp. 5639–5646.

[160] E.J. O'Loughlin, S.D. Kelly, R.E. Cook, R. Csencsits, K.M. Kemner. (2003). Reduction of uranium (VI) by mixed iron (II)/iron (III) hydroxide (green rust): formation of UO_2 nanoparticles, Environ. Sci. Technol. 37, pp. 721–727.

[161] Brooks, S. C., Fredrickson, J. K., Carroll, S. L., Kennedy, D. W., Zachara, J. M., Plymale, A. E., Kelly, S. D., Kemner, K. M., Fendorf, S. (2003). Inhibition of bacterial U(VI) reduction by calcium. Environ.Sci. Technol. 37(9), pp.1850–1858.

[162] Belli, K. M., DiChristina, T. J., Van Cappellen, P., Taillefert, M. (2015). Effects of aqueous uranyl speciation on the kinetics of microbial uranium reduction. Geochimica et Cosmochimica Acta, 157,pp. 109–124.

[163] William, J.D. (1997). Groundwater Geochemistry: Fundamentals and applications to contaminant CRC Press Taylor & Francis Group 6000 Broken Sound Parkway NW, Suite 300 Boca Raton, FL pp.33487-2742.

[164] Bajaj, N.S., Joshi, R.A. (2021). Chapter 3-Energy materials: synthesis and characterization techniques, Energy Materials. Fundamentals to Applications.pp. 61-82.

[165] Carlsson, T., Aalto, H. (1997). Coprecipitation of Ni with Calcite: An Experimental Study. MRS Online Proceedings Library 506, pp.621–627.

[166] Bruno, J., Montoya, V. (2012).From aqueous solution to solid solutions: A process-oriented review of the work performed within the FUNMIG project.Applied Geochemistry, Vol. 27, Issue 2, pp. 444-452.

[167] Rane, A.V., Kanny,K., Abitha,V.K., Thomas,S. (2018). Methods for Synthesis of Nanoparticles and Fabrication of Nanocomposites Chapter 5. Synthesis of Inorganic Nanomaterials pp. 121-13.

[168] Enzo Curti, E. (1999). Coprecipitation of radionuclides with calcite: estimation of partition coefficient based on a review of laboratory investigations and geochemical data. Applied Geochemistry Vol. 14, pp. 433-445.

[169] Abbaschian R., Reed, H., Robert, E. (2008). Physical Metallurgy Principles. ISBN 978-0-495-08254-5.

[170] Stumm, W., Morgan, J.J. (1981).Aquatic chemistry: An introduction, emphasizing chemical equilibria in natural waters, Second Edition. Chapter 5 pp. 287-298.

[171] Doerner H. A., Hoskins W. M. (1925). J. Am. Chem. Soc. 47, 662.

[172] Guillaumont, R., Fanghänel, T., Fuger, J., Grenthe, I., Neck, V., Palmer, D.A., Rand, M.H. (2003). Update on the Chemical Thermodynamics of Uranium, Neptunium, Plutonium, Americium and Technetium, Vol.5 of Chemical Thermodynamics, in Elsevier Science Publishers, Amsterdam,
[173] Rai, D., Felmy, A.R., Ryan, J. L. (1990). Uranium (IV) hydrolysis constants and solubility product of $UO_2 \cdot xH_2O$(am), Inorg. Chem. 29, pp.260-264.

[174] Mesmer, R.E., Baes, C.F. (1990). Review of Hydrolysis Behavior of Ions in Aqueous Solutions. MRS Online Proceedings Library 180, 85.

[175] Kim, J. I. (1991). Actinide colloid generation in groundwater. Radiochimica Acta, 52–53, pp.71–81.

[176] KTH (1959). Some Laboratory Methods, TRITA-OOK-T128. Royal Institute of Technology, Stockholm, Sweden.

[177] M. Laaksoharju, J. Smellie, E.L. Tullborg, M. Gimeno, L. Hallbeck, J. Molinero, N. Waber, (2008). Bedrock hydrogeochemistry Forsmark, Site Descriptive Modelling SDM-Site Forsmark,

[178] Chen, R., Chen, J., Hong, M., Zhang, W. (2016). Formation of chukanovite in simulated groundwater containing CO_3^{2-}. Environ. Techn. 37, pp.2786–2792

[179] Fanghänel, T., Neck, V., Kim, J. I. (1996). The ion product of H_2O, dissociation constants of H_2CO_3, and Pitzer parameters in the system $Na^+/H^+/OH^-/HCO_3^-/CO_3^{2-}/ClO_4^-/H_2O$ at 25 °C. Journal of Solution Chemistry, 25, pp.327–343

[180] Yamada.N (2015). Kinetic energy discrimination in collision/reaction cell ICP-MS: theoretical review of principles and limitations, Spectrochimica Acta Part B: Atomic Spectrosc. 110.pp. 31– 44.

[181] Ghormley, J., A. Stewart, A. (1956). Effects of γ-radiation on ice 1, J. Am. Chem. Soc. 78 (13) pp. 2934–2939.

[182] Chaves. L.H. (2005). The role of green rust in the environment: a review, Revista Brasileira de Engenharia Agrícola e Ambiental 9, pp. 284–288.

[183] Taylor,R., McKenzie, R. (1980). The influence of aluminum on iron oxides. VI. The formation of Fe (II)-Al (III) hydroxy-chlorides,-sulfates, and carbonates as new members of the pyroaurite group and their significance in soils, Clays Clay Miner 28 , pp.179–187.

[184] E.J. O'Loughlin, S.D. Kelly, R.E. Cook, R. Csencsits, K.M. Kemner, (2003). Reduction of uranium (VI) by mixed iron (II)/iron (III) hydroxide (green rust): formation of UO_2 nanoparticles, Environ. Sci. Technol. 37, pp. 721–727,

[185] T. Gouder, R. Eloirdi, R. Caciuffo, (2018). Direct observation of pure pentavalent). Directing U_2O_5 thin films by high resolution photoemission spectroscopy, Sci. Rep. 8, pp. 1–7 .

[186] Santos, B., Nesbitt, H., Noel, J.Shoesmith.D. (2004).X-ray photoelectron spectroscopy study of anodically oxidized SIMFUEL surfaces, Electrochimica Acta 49, pp.1863–1873

[187] Parkhurst, D.L. Appelo, C. (2013).D). Description input and examples for PHREEQC version 3—a computer program for speciation, batch-reaction, one-dimensional transport, and inverse geochemical calculations, US Geol. Surv. Tech. Methods 6 497 .

[188] Ekberg, C., Emrén.A. (1993). Finding and correcting calculation errors in PHREEQE, 4th Int. Conf. on the Chem. and Migr. Behaviour of Actinides and Fission Products in the Geosphere, Charleston, SC USA, Dec. 12-17,Oldenbourg Verlag, Munich.

[189] D. Rai, Y.A. Gorby, J.K. Fredrickson, D.A. Moore, M. Yui (2002).Reductive dissolution of PuO_2(am): the effect of Fe(II) and hydroquinone, J. Soln. Chem. 31, pp.433–453.

[190] Neff. D. (2003).Apport Des Analogues Arch´eologiques a L´Estimation Des Vitesses Moyennes Et a L´´ Etude Des M´ecanismes De Corrosion a Tr` es Long Terme Des Aciers Non Alli´es Dans Les Sols, Ph.D. Thesis, Universit´ e de Technologie de Compi`egne, France,

[191] De Faria, D.J.A., Silva,S.V.., de Oliveira. M.J. (1997). Raman micro spectroscopy of some iron oxides and hydroxides, J. Raman Spectrosc. 28, pp.873–876.

[192] Schlegel, M.L., Bataillon, C., Brucker, F., Blanc,C., Pret, D., Foy E., Chorro.M.(2014). Corrosion of metal iron in contact with anoxic clay at 90 degrees C: characterization of the corrosion products after two years of interaction, Appl. Geochem. 51, pp.1–14.

[193] Remazeilles, C., Refait, P. (2009). Fe(II) hydroxycarbonate $Fe_2(OH)_2CO_3$ (chukanovite) as iron corrosion product; Synthesis and study by Fourier Transform Infrared Spectroscopy. Polyhedron 28 pp. 749-756.

[194] Lutz, H. D., Möller, H., Schmidt, M. (1994). Lattice vibration spectra. Part LXXXII. Brucite-type hydroxides $M(OH)_2$ (M = Ca, Mn, Co, Fe, Cd): IR and Raman spectra; neutron diffraction of $Fe(OH)_2$. Journal of Molecular Structure, 328, pp. 121–132

[195] Matthiesen, H., Hilbert, L. R., Gregory, D. J. (2003). Siderite as a corrosion product on archaeological iron from a waterlogged environment. Studies in Conservation, 48(3), pp.183–194

[196] Rai D., Felmy, A., Sterner, S.M., Moore, D.A., Mason M.J. (1997). The solubility of Th (IV) and U (IV) hydrous oxides in concentrated NaCl and $MgCl_2$ solutions, Radiochim. Acta 79, pp.239-247.

[197] Rai, D., Yui, M., Moore, D.A. (2003). Solubility and solubility product at 22°C of UO_2(c) precipitated from aqueous U(IV) solutions. J. Solution Chem., 32, pp. 1–17.

[198] Kragten, J., Decnop-Weever, L. G. (1978). Solubility and hydrolysis of cerium(III) in sodium perchlorate solutions. Talanta, 25(3), pp.147–150.

[199] Brown, P., Ekberg, C. (2016). Studies on the Hydrolysis of Metal Ions. Wiley VCH.

[200] Jordan, N., Thoenen, T., Spahiu, K., Kelling, J., Starke, S., Brendler, V. (2024). A critical review of the solution chemistry, solubility, and thermodynamics of europium: Recent advances on the Eu(III) hydrolysis. Coordination Chemistry Reviews, 510, 215702

[201] Rai D., Hess N., Yui M., Felmy A., Moore D. (2004). Thermodynamics and solubility of $U_xNp_{1-x}O_2$ (am) solid solutions in the carbonate system, Radiochim. Acta, 92, pp.527-535.

[202] Toby, B.H. and Von Dreele, R.B. (2013). GSAS-II: the genesis of a modern open-source all-purpose crystallography software package, J. Appl. Crystallography 46, pp. 544-549.

[203] Kleykamp, H. (1993). The solubility of selected fission products in UO_2 and (U, Pu) O_2, Journal of Nuclear Materials,206, pp. 82-86

[204] Hansson, N.L, Tam, P.L, Ekberg, C., Spahiu, K. (2019).XPS study of external alpha radiolytic oxidation of UO_2 in the presence of argon or hydrogen, J.Nucl.Mater., Vol. 543,152604

[205] Ilton, E.S., Bagus,P. S. (2011). XPS determination of uranium oxidation states, Surf. Interface Anal.43, pp. 1549-1560.

[206] Paparazzo, E. (2018). Use and misuse of X-ray photoemission spectroscopy of Ce3d spectra of Ce_2O_3 and CeO_2. Journal of Physics: Condensed Matter, Vol 30, 343003.

[207] McIntire, W.L. (1963). Trace element partition coefficients- a review of the theory and applications to geology, Cosmochim.Geochim.Acta 27, pp.1209-1264.

[208] Martin P., Grandjean S., Valot C., Carlot G., Riper, M., Blanc P., Hennig C., 2007. XAS study of $(U_{1-y}Pu_y)O_2$ solid solutions. J. All. Comp., 444-445, pp. 410-414.

[209] Leinders, G., Cardinales T., Binnemans, K., Verwerft, M. (2015). Accurate lattice parameter measurements of stoichiometric uranium dioxide, J. Nucl. Mater. 469, pp.135-142.

[210] Chollet, M., Belin, R. C., Richaud, J.-C., Adenot F. (2012). New insights into the thermal expansion of neptunium dioxide up to 2000 K. Procedia Chemistry, **7**, pp.466–471.

[211] Conradson S.D, Abney K.D., Begg B., Brady E.D., Clark D.L., den Auwer C., Ding M., Dorhout P.K., Espinoza-Foller F.J., Gordon R.L., Haire R.G., Hess N.J., Webster Keogh D., Lander G., Lupinetti A., Morales L.A., Neu M.P., Palmer P.D., Paviet-Hartmann P., Reilly S.D., Runde W., Tait C.D., Veirs D.K., Wastin F.(2004). Higher order speciation effects on plutonium L3 X-ray near-edge spectra, Inorg. Chem. 43, pp.116-131.

[212] Arab-Chapelet B., De Bruycker F., Picart S., Leturcq G., Grandjean S., 2008. Characterisation of mixed uranium plutonium co-precipitates and oxides synthetised by oxalic co-conversion, Proc. Atalante Conference, Montpellier, paper 3_02.

[213] Arab-Chapelet, B., Martin, P. M., Costenoble, S., Delahaye, T., Scheinost, A. C., Grandjean, S., Abraham, F. (2016). Multiscale structural characterizations of mixed U(IV)–An(III) oxalates (An(III) = Pu or Am) combining XAS and XRD measurements. Dalton Transactions, 45, pp.6909–6919.

[214] Grandjean, S., Arab-Chapelet, B., Robisson, A.-C., Abraham, F., Martin, P., Dancausse, J.-P., Herlet, N., Léorier, C. (2009). Structure of mixed U(IV)–An(III) precursors synthesized by co-conversion methods (An = Pu, Am or Cm). Journal of Nuclear Materials, 385, pp.204–207.

[215] Cho, H.R., Youn, Y.S., Euo Jung, E.C., Cha,W. (2016). Hydrolysis of trivalent plutonium and solubility of $Pu(OH)_3$ (am) under electrolytic reducing conditions, Royal society of Chemistry, issue 48.

[216] Müller, P., Fellhauer, D., Schild, D., Gaona, X., Dardenne, K., Rothe, J., Altmaier, M., Geckeis, H. (2025). Solubility, speciation and thermodynamics of $PuCO_3OH$(cr) in carbonate-containing NaCl solutions. Angewandte Chemie International Edition, 64(50), e202515522.

[217] Saleh, M., Hedberg, M., Tam, P. L., Spahiu, K., Persson, I., Ekberg, C. (2024). Coprecipitation of Ce(III) oxide with UO_2. Journal of Synchrotron Radiation, 31,pp. 1489–1504.

[218] Fujiwara, K., Yamana, H., Fujii, T., Moriyama, H. (2001). Solubility product of plutonium hydrous oxide. Journal of Nuclear Fuel Cycle and Environment, 7, pp.17-23.

[219] Fujiwara, K., Yamana, H., Fujii, T., Moriyama, H. (2002). Solubility product of plutonium hydrous oxide and its ionic strength dependence. Radiochimica Acta, 90(12), pp.857–861

[220] Felmy, A. R., Rai, D., Schramke, J. A., & Ryan, J. L. (1989). The solubility of plutonium hydroxide in dilute solution and in high-ionic-strength chloride brines. Radiochimica Acta, 48(1-2), pp.29-36.

[221] Allard, B, Kipatsi, H., Liljenzin J.O. (1980). Expected species of uranium, neptunium and plutonium in neutral aqueous solutions, J. Inorg. Nucl. Chem. 42, pp. 1015-1027.

[222] Neck, V., Altmaier, M., Fanghänel T. (2007). Solubility of plutonium hydroxides/hydrous oxides under reducing conditions and in the presence of oxygen, C. R. Acad, Sci. Chim. 10, pp.959-977.

[223] Tasi, A., Gaona, X., Fellhauer, D., Böttle, M., Rothe, J., Dardenne, K., Schild, D., Grivé, M., Colàs, E., Bruno, J., Källström, K., Altmaier, M., Geckeis, H. (2018). Redox behavior and solubility of plutonium under alkaline, reducing conditions. Radiochim. Acta 106, pp.259-279.

[224] Rai, D., Moore, D. A., Felmy, A. R., Rosso, K. M., Qafoku, O., Buck, E. C., Ilton, E. S. (2011). Heterogeneous reduction of PuO_2 with Fe(II): Importance of the Fe(III) reaction product. Environmental Science & Technology, 45(9), pp.3952–3958

Appendix

The table below shows the amount of chemicals used in the synthesis of the simulated Forsmark groundwater used for the leaching experiment

		1L Basis	pH		7.19	
ID 02A						
	n [mol/L]	M (g/mol)	m (g/L)	mass in (mg/L)	Cations/ Anions	Results 02A [mol/L]
Reagents					Na^+	9.657E-02
NaCl	8.08E-02	58.44	4.722E+00	4.722E+03	K^+	9.310E-04
$MgCl_2$	1.00E-02	95.211	9.556E-01	9.556E+02	Ca^{2+}	2.221E-02
KF	7.74E-05	58.097	4.495E-03	4.495E+00	Mg^{2+}	1.004E-02
$CaCl_2 \cdot 6H_2O$	2.22E-02	219.07	4.865E+00	4.865E+03	HCO_3^-	2.065E-03
$NaHCO_3$	2.06E-03	84.007	1.735E-01	1.735E+02	Cl^-	1,489E-01
$FeSO_4 \cdot 7H_2O$	4.05E-05	278.02	1.125E-02	1.125E+01	SO_4^{2-}	5.275E-03
NaBr	3.04E-04	102.894	3.129E-02	3.129E+01	Br^-	3.041E-04
Na_2SO_4	5.20E-03	142.04	7.381E-01	7.381E+02	F^-	7.737E-05
Na_2SiO_3	2.16E-04	122.06	2.642E-02	2.642E+01	Si	2,165E-04
KCl	8.54E-04	74.55	6.364E-02	6.364E+01	Fe^{2+}	4.047E-05
$MnSO_4 \cdot H_2O$	3.77E-05	169.003	6.368E-03	6.368E+00	Mn^{2+}	3.768E-05
$SrCl_2 \cdot 6H_2O$	9.90E-05	266.6	2.638E-02	2.638E+01	Sr^{2+}	9.895E-05